Low-temperature co-sputtering for interlayer-free high performance Nb_3Sn thin film coated copper SRF cavities

Zur Erlangung des akademischen Grades Doktor-Ingenieur (Dr.-Ing.)
Genehmigte Dissertation von Nils Schäfer aus Schorndorf
Tag der Einreichung: 09.11.2023, Tag der Prüfung: 11.12.2023

1. Gutachten: Prof. Dr. Lambert Alff
2. Gutachten: Prof. Dr. Dirk Lützenkirchen-Hecht
Darmstadt, Technische Universität Darmstadt

TECHNISCHE UNIVERSITÄT DARMSTADT

Materials and Earth Sciences Department

Materials Science

Advanced Thin Film Technology

Low-temperature co-sputtering for interlayer-free high performance Nb_3Sn thin film coated copper SRF cavities

Accepted doctoral thesis by Nils Schäfer

Date of submission: 09.11.2023
Date of thesis defense: 11.12.2023

Darmstadt, Technische Universität Darmstadt

Erklärungen laut Promotionsordnung

§ 8 Abs. 1 lit. c PromO

Ich versichere hiermit, dass die elektronische Version meiner Dissertation mit der schriftlichen Version übereinstimmt.

§ 8 Abs. 1 lit. d PromO

Ich versichere hiermit, dass zu einem vorherigen Zeitpunkt noch keine Promotion versucht wurde. In diesem Fall sind nähere Angaben über Zeitpunkt, Hochschule, Dissertationsthema und Ergebnis dieses Versuchs mitzuteilen.

§ 9 Abs. 1 PromO

Ich versichere hiermit, dass die vorliegende Dissertation selbstständig und nur unter Verwendung der angegebenen Quellen verfasst wurde.

§ 9 Abs. 2 PromO

Die Arbeit hat bisher noch nicht zu Prüfungszwecken gedient.

Darmstadt, 09.11.2023

N. Schäfer

Contents

Zusammenfassung

Dünne Schichten aus Nb_3Sn sind ein vielversprechender Kandidat, um Vollmaterialkavitäten aus Niob für die Radiofrequenztechnologie zu ersetzen. Neue Materialien, wie Nb_3Sn, sind in der Lage die kryogene Effizienz und Beschleunigungsgradienten durch einen niedrigeren Oberflächenwiderstand und größere kritische magnetische Felder zu erreichen. Co-Sputtering von Nb_3Sn ist ein Prozess, der es ermöglicht die Sputterrate und die kinetische Energie der Elemente Nb und Sn separat zu kontrollieren. Das erlaubt eine präzise Kontrolle des Dünnschichtwachstums und der Stöchiometrie der dünnen Schichten aus Nb_3Sn in großem Maße. Mit dieser Methode ist es möglich eine kritische Temperatur $T_{c,0}$ (Punkt, an dem die Probe vollständig im supraleitenden Zustand ist) von $16.8\,\mathrm{K}$ und ein kritisches Feld H_{c1} von $50\,\mathrm{mT}$ auf Kupfersubstrat bei lediglich $480\,^\circ\mathrm{C}$ Substrattemperatur bei $60\,\mathrm{min}$ Haltedauer ohne Wärmebehandlung nach dem Aufwachsen. Eine exzellente Homogenität in der Oberfläche und Tiefe der Dünnschicht ist gezeigt. Die angewandte Synthesetemperatur ist ausreichend niedrig, um die Durchmischung der Elemente zu unterdrücken. Die erzeugten Proben schirmen das externe Feld überzeugend in beiden Orientierungen parallel und senkrecht zum externen Feld ab. Röntgendiffraktogramme zeugen von einer hohen Phasenreinheit der schnell gewachsenen Proben bei einer niedrigen Defektdichte für Synthesetemperaturen über $400\,^\circ\mathrm{C}$ und eine deutliche Textur für Proben gewachsen bei hohen Sputterleistungen. The hohe Sputterleistung unterstützt das Wachstum großerer Körner. Jedoch können unvorteilhafte Abscheideparameter zu inhomogenen Korngrenzenzuständen führen, die ein Netzwerk schwacher Kopplung der Körner bilden. Der Ursprung ist gefunden in Zinnablagerungen an den Korngrenzen, die zu performanzeinschränkender Abweichung der Stöchiometrie innerhalb der Körner führen. Makroskopisch führt das zu einer großen Übergangsbreite vom normalleitenden zum supraleitenden Zustand und zusätzlichen Zwischenniveaus des Widerstandes am Übergang. Es ist weiterhin gezeigt wie kinetische Energie zur Homogenisierung der Schicht beiträgt und die Korngrenzenzustände verbessert. Wärmebehandlung zeigte, dass sie Korngrenzenwachstum unterstützt, jedoch auch Zinnablagerungen und Einschränkungen durch Korngrenzen verstärkt. Sprünge des magnetischen Flusses tauchen auf für dünne Schichten beschichtet auf Quarzglassubstraten. Es wird dann gezeigt, dass die Sprünge des magnetisches Flusses durch Überbrückung über ein gutleitendes Substrat (in diesem Fall Kupfer), das das Stabilitätskriterium erfüllt, gelöst werden. Auf Kupfer abgeschiedene Nb_3Sn Filme scheinen eine Oberflächenrauigkeit R_q in der Größenordnung $12\,\mathrm{nm}$ und Korngrößen von bis zu $200\,\mathrm{nm}$, sowie eine exzellente Haftung, bestimmt durch Kratztests und Eindringhärteprüfung, zu haben. Die Dicke der dünnen Schichten aus Nb_3Sn auf Kupfer hat einen einen Einfluss auf die physikalischen Eigenschaften kritische Temperatur $T_{c,0}$ und kritisches Feld H_{c1}. Während die kritische Temperatur für niedriger Schichtdicken abnimmt, nimmt das kritische Feld bis auf $190\,\mathrm{mT}$ bei eine Schichtdicke von $240\,\mathrm{nm}$ zu. Die niedrige Synthesetemperatur zusammen mit exzellenter Performanz der sputterbeschichteten Filme ermöglichen die hocheffiziente Nb_3Sn Dünnschichtüberzogene Kupferkavitäten für niedrigste Leistungseinbußen und optimaler Wärmeabführung durch niedrigen Oberflächenwiderstand des Nb_3Sn und hoher Wärmeleitfähigkeit des Kupfers.

Abstract

Thin film Nb_3Sn is a promising candidate to replace bulk niobium cavities for radiofrequency application. New materials, like Nb_3Sn, can increase cryogenic efficiency and acceleration gradients by lower surface resistivity or higher critical magnetic fields. Nb_3Sn co-sputtering is a technique able to control the sputtering rate and kinetic energy of the elements Nb and Sn separately. This allows precise control of the thin film growth and stoichiometry of Nb_3Sn thin films in a broad range. Using this method, it is possible to achieve a critical temperature $T_{c,0}$ (point of fully superconducting sample) of $16.8\,\mathrm{K}$ and a critical field H_{c1} of $50\,\mathrm{mT}$ on copper substrate at only $480\,^{\circ}\mathrm{C}$ and $60\,\mathrm{min}$ heat exposure without heat treatments after growth. An excellent homogeneity is demonstrated in surface plane and depth. The used synthesis temperature is shown to be sufficient low to suppress detrimental inter-diffusion of the elements. The produced samples strongly shield the external field in both directions, parallel and perpendicular to the external magnetic field. XRD patterns reveal a high phase purity for fast grown samples with a low defect concentration for synthesis temperatures above $400\,^{\circ}\mathrm{C}$ and a strong texture for samples grown at high sputter power. The sputter power exhibits to promote growth of larger grains. However, it has been shown that unfavorable deposition parameters can be lead to inhomogeneous grain boundary conditions that form weak link networks. The origin is found in tin grain boundary segregations leading to performance limiting off-stoichiometry within the grains. Macroscopically, it leads to a broad transition width from normal to superconducting state and additional intermediate resistances appear within the transition. It is further shown how kinetic energy can contribute to homogenize the film and improve the grain boundary condition. Heat treatment of the Nb_3Sn thin films however, is demonstrated to promote grain growth, but also tin segregation and emphasize the grain boundary limitation. Magnetic flux jumps appear for measurements of thin films coated on fused silica substrates. It is then demonstrated that the flux jump issue can be solved by shunting via well conducting substrate (copper in this case) that fulfills the stability criterion. Deposited films of Nb_3Sn appear to have a surface roughness R_q in the range of $12\,\mathrm{nm}$ and grain sizes of up to $200\,\mathrm{nm}$ as well as an excellent adhesion shown by scratch and indentation tests. The thickness of Nb_3Sn thin films on copper has shown impact on the physical properties critical temperature $T_{c,0}$ and critical field H_{c1}. While the critical temperature decreases for decreasing thickness, the critical field is enhanced up to $190\,\mathrm{mT}$ at a film thickness of $240\,\mathrm{nm}$. The low synthesis temperature together with excellent performance of the sputter-coated films pave the way to highly efficient Nb_3Sn thin film coated copper cavity for lowest power loss and optimal heat removal by the low surface resistivity of Nb_3Sn and high heat conductivity of copper.

1. Introduction

A long established tradition of naming elements after their place of discovery was continued in 1994, when the chemical element 110 was first created. This chemical element was named Darmstadtium in recognition of the contribution to this discovery. Darmstadtium was synthesized by a team of scientists from the laboratory of heavy ion research (GSI) using the universal linear accelerator UNILAC in Darmstadt. At this facility, the new element was created using fusion evaporation where bombardment of nickel ions onto a lead target formed the new element [1]. The facility used for the nickel ion acceleration is a particle accelerator. Nowadays, such facilities utilize superconducting materials for high efficient operation.

1.1. Discovery and historic events of superconductivity

In 1911, a discovery made by Kamerlingh Onnes was that the electrical resistivity in pure metals such as mercury, tin and lead vanished at very low temperatures [2]. This phenomenon later acquired worldwide recognition as superconductivity. Another significant discovery was made in 1933 by Meissner and Ochsenfeld [3]. They discovered that not only a magnetic field is excluded from a superconductor that can be explained with perfect conductivity, but additionally, a present magnetic field is expelled by a superconductor in the superconducting state, i.e. the sample becomes a perfect diamagnet. Back in that time, the phenomenon remained without any microscopical description. Only decades later, in 1953, a microscopical theory named after their inventors Bardeen, Cooper and Schrieffer emerged [4]. Another important event revitalized the subject in 1986, when Bednorz and Müller discovered a new family of high temperature superconductor ceramics [5]. In the last decades, hundreds of superconducting materials have been found. Their critical temperature is plotted over the year of discovery in Fig. 1.1. Recently, even materials with superconducting properties up to $150\,\mathrm{K}$ at ambient pressure were found. Exceeding $77\,\mathrm{K}$ critical temperature was a tremendous achievement, since this is the boiling point of nitrogen. For these materials, liquid nitrogen instead of liquid helium can be used for cooling.

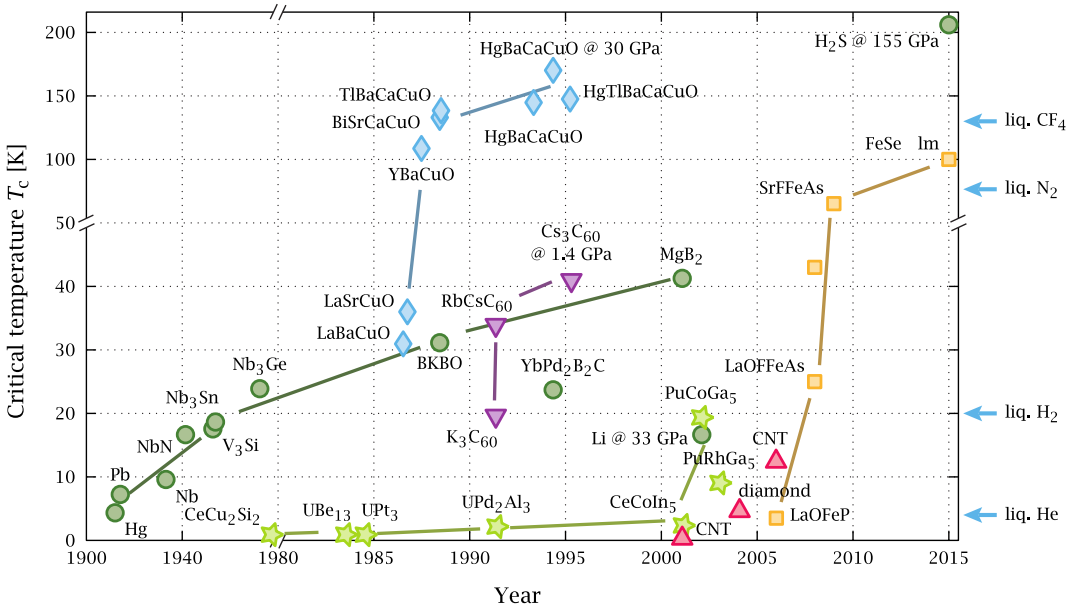

Figure 1.1.: Timeline of superconducting materials by their discovery versus critical temperature. Different superconductor classes are represented by colors [6].

1.2. Practical superconductors

Out of several hundred superconducting materials, only a handful gained practical importance. Although lacking behind in the previous comparison, the dark-green-marked group of the so-called high current superconductors in Fig. 1.1 is of industrial importance. Niobium, Nb-Ti, Nb_3Sn and V_3Ga found their respective field of application. The main prerequisite for industrial applications is the ability to be fabricated in cables or stripes in excellent condition. Nb-Ti is clearly the material-of-choice for field production up to $9\,T$ [7]. The reason is found in the ductility and ease of production. The superconductors Nb_3Sn and V_3Ga belong to the A-15 crystal structure. Although this class is highly brittle, it comes with a bunch of advantages. Among high critical fields and high current densities, the class has isotropic properties. For applications higher than $9\,T$, Nb_3Sn became the first choice over V_3Ga due to the fast improvements in fabrication and its significantly cheaper elements. Today, Nb_3Sn is the best choice for application in high field magnets [7]. Beginning in 2009, the national high magnetic field laboratory built the record $32\,T$ magnet by a combination of the conventional superconductors Nb_3Sn and Nb-Ti together with the high temperature superconductor YBCO [8]. Although it was possible to incorporate YBCO, it could not fully replace the other superconductors due to tough manufacturing of this material. Strong magnets are essential in medical diagnostics, particle accelerators, and upcoming fusion reactors.

1.3. Role of superconducting materials in particle accelerators

Nowadays, superconducting materials are essential for state-of-the-art particle accelerators. Superconducting magnets are used for the creation of strong magnetic fields in dipoles and quadrupoles that direct and focus the beam of particles, respectively. Although they need to be cooled by liquid helium, the high created magnetic field is overall advantageous. Superconducting detectors are another application of superconducting materials with far superior properties in comparison to normal magnets [9]. In particular, this work deals with superconducting materials used for particle acceleration itself. Particles are accelerated

in cavities by oscillating electric fields. A cavity is utilized to create a resonant electromagnetic wave. This way, an always accelerating electric field is used to accelerate the particles in successive cavities or cells up to near speed of light. However, in a second (imaginary) circulation of the beam path, the particles have reached the maximum energy (maximum velocity) and the cavities maintain its energy. It is a clear advantage of the oscillating electric field to allow 'endless' acceleration. However, it is a drawback that the change of electric field generates a magnetic field perpendicular to the maximum electric field. This circular magnetic field is shown in Fig. 1.2. The left schematic shows the phase of acceleration for negative particles (from left to right), the right demonstrates the phase of deceleration. The maximal magnetic field is delayed by $90°$ and rotated by $90°$ to the electric field.

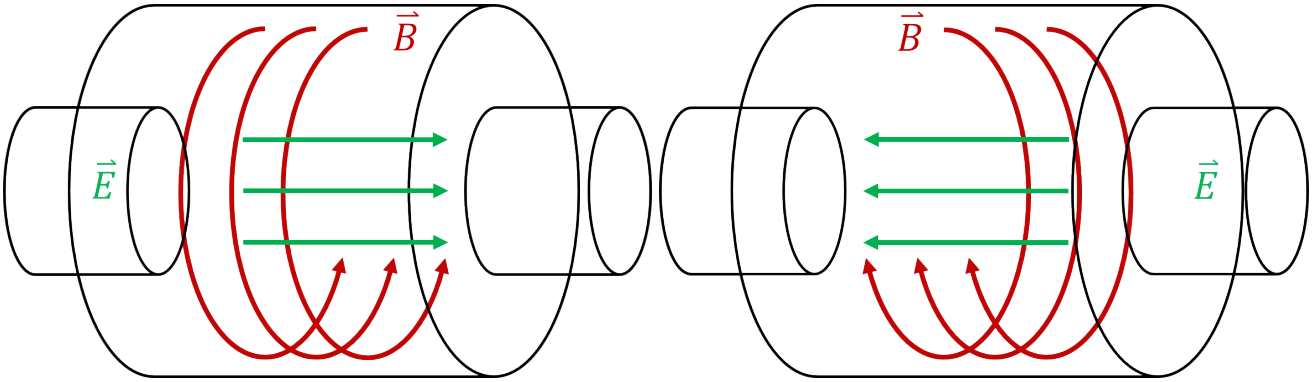

Figure 1.2.: Simplified description of electric and magnetic field in an ideal pillbox cavity. The left cavity shows phase of maximum acceleration (left to right) while the right cavity shows the phase of deceleration.

Although a single cell works in principle, multi-cell cavities (as shown in Fig. 1.3) are commonly used in particle accelerators. Here, the electric field in one cell is at maximum strength in either parallel or anti-parallel direction to the particle's velocity while the field of the adjacent cells point in the opposite direction [10]. If the particle passes exactly at peak amplitude, the acceleration is the highest. Otherwise, the acceleration is weaker or the particle is even decelerated. A possible application of non-maximal deceleration is to separate particles into bunches. The maximal deceleration can be used forrecuperation of the beam energy and reduction of radiation [11].

Figure 1.3.: TESLA-type bulk niobium 9 cell superconducting radiofrequency cavity [12].

As a consequence of the magnetic field, the cavity material is magnetized (inducing shielding currents in a superconductor). Due to electric resistivity, this magnetization is a power loss and means that it is not possible to put the whole applied power into the beam. To minimize the power loss, superconductors are used to shield the cavity material from this magnetic field. By replacing copper with superconducting niobium the power loss can be reduced by the factor 10^4 to 10^5 depending on the frequency [13, 12].

Although they need to be operated at low temperatures, the perfect diamagnetic behavior can be used to minimize losses.

A superconducting material shows no electrical resistance for continuous currents. However, the electrical resistivity in the RF mode is not zero. Normal conducting electrons in the surface see an oscillating magnetic field and start to oscillate. This oscillating electrons collide with lattice atoms and the result is the electric resistance.

In summary, the usage of new superconducting materials can be used to save vast amounts of liquid helium. This is possible by the lower resistivity and the higher operation temperature.

1.4. Significance of particle accelerators

Only a few hundred of the world wide 17,000 accelerator facilities are used for research. About 7,000 are used for medical purposes of 30 million patients every year. In medicine, accelerators are used for radiation therapy of tumors. Conventionally, electrons are either accelerated towards the tumor or a metal-block that then emits Bremsstrahlung. Another medical treatment uses antimatter like positrons that are produced by a particle accelerator directly before being taken orally. In Germany, there are three facilities in Berlin, Heidelberg and München that use hadrons like protons for radiation therapy. Hadrons can be used to increase the local damage of the tumor and reduce the damage of the surroundings.

In industry, particle accelerators are used for doping silicon or germanium wafers. This method allows to build fast transistors that are important for digital electronics. In total, the products produced or processed with particle accelerators are worth 500 billion € every year.

Besides these applications, particle accelerators are used in research. Typically, the particle accelerators are used to generate highly brilliant and monochromatic x-ray for material research [14].

1.5. Emergence of Nb_3Sn as cavity material

Superconducting bulk niobium cavities have been elaborated over decades and are state-of-the-art in modern highly efficient particle accelerators. Still, cooling systems make a huge part of the whole energy consumption that is, for instance, about $120\,\mathrm{MW}$ for the Large Hadron Collider (LHC) at CERN [15]. In comparison, Nb is unfavorable with a critical temperature of $9\,\mathrm{K}$ and critical field of $190\,\mathrm{mT}$ [9, 16]. However, it is the material-of-choice in particle acceleration by its outstanding high acceleration gradients. The reason is the rather simple manufacturing. Due to its low critical temperature, it is necessary to operate the cavity at around $2\,\mathrm{K}$ to achieve up to $45\,\mathrm{MV/m}$ [9]. At this point, the magnetic field reaches the critical value of $190\,\mathrm{mT}$ [9, 16]. Operating the cavity at this temperature makes it rather cost-intense as it requires super-cooling by liquid helium. Super-cooling requires complex refrigeration systems including huge pumps and huge amounts of liquid helium. $1\,\mathrm{W}$ dissipated power to the system requires $1\,\mathrm{kW}$ refrigeration power [9], that motivates researchers all-around the globe to find materials with lower surface resistivity. A promising approach is the usage of Nb_3Sn with a critical temperature of $18.3\,\mathrm{K}$ [17] and a critical field of $400\,\mathrm{mT}$ [18], but the most remarkable property is the low surface resistivity that is around $1\,\%$ of that of niobium at $4.2\,\mathrm{K}$ and $9.5\,\mathrm{GHz}$ [19]. This could save around $99\,\%$ cooling expenses.

Unfortunately, Nb_3Sn is brittle and cannot be used as bulk material. Therefore, the thin film approach on carrier material is the only possibility to use this high performance material in cavities. So far, the achieved acceleration fields are around $24\,\mathrm{MV/m}$ [20] that is lower than the theoretical limitations of $100\,\mathrm{MV\,m^{-1}}$ [21] and lower as the performance of niobium. Nb_3Sn has shown unsatisfactory cavity performance, most likely, due to grain boundary effects [22]. Particularly, the difference in vapor pressure of the elements Nb and Sn as well as the short coherence length of Nb_3Sn are reasons for poor performance.

1.6. Previous approaches of Nb_3Sn synthesis

Tin diffusion is the most straight-forward synthesis process for actual cavity coating, but still, people try to find other processes to improve performance. The synthesis of Nb_3Sn remains a huge challenge [23]. The different nature of Nb and Sn are the reason for the challenging synthesis. The refractory metal Nb requires a relatively high temperature for moderate diffusivity. At this temperatures, Sn is highly diffuse and tends to diffuse to the surface and evaporate [19]. This limits the performance, as the performance in this material is strongly dependent on the proper stoichiometry [24, 25]. Over five decades, several processes were investigated to synthesize this material. Among the tin diffusion process [26, 27, 28, 29, 30, 31], there is sequential sputtering [32, 33, 34], single target sputtering [25, 35, 36, 37], chemical vapor deposition [38], electrochemical deposition [39, 40] and many other approaches.

Tin diffusion is the only process used for Nb_3Sn cavity coating over decades. Several variations of this process were investigated to improve performance. Fig. 1.4 gives an overview of the different adaptations.

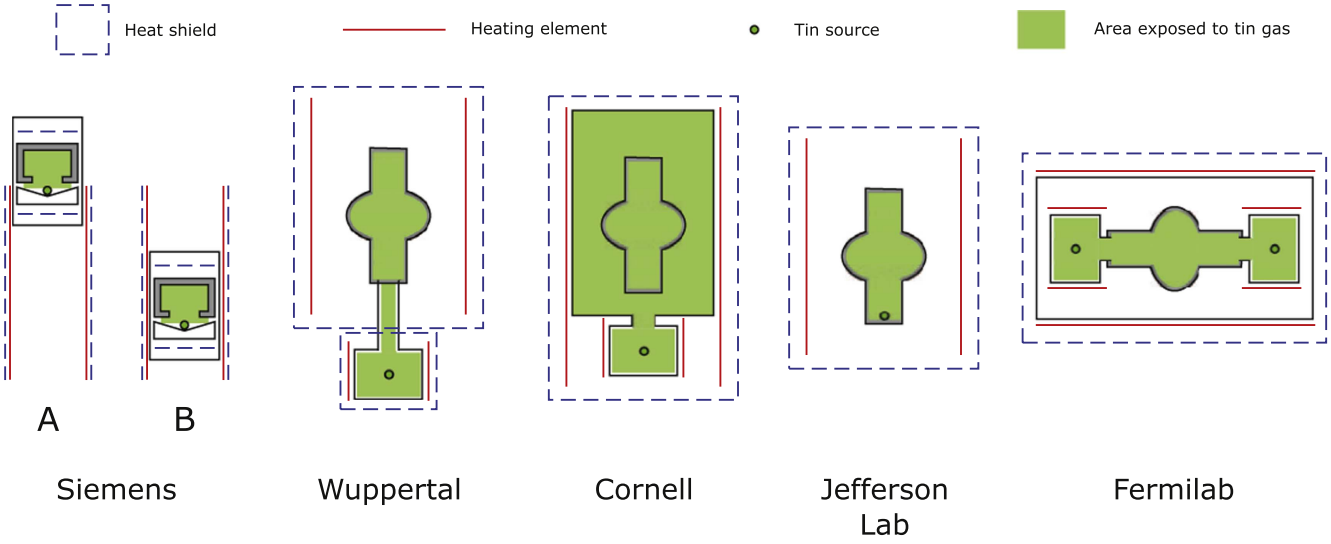

Figure 1.4.: Literature review of different approaches to convert the inner surface of a bulk niobium cavity to Nb_3Sn using tin diffusion. Solid black lines show bulk niobium cavities. Evacuated and sealed volume exposed to tin vapor ist marked in green. Red lines show heat sources while dashed black lines show heat shields. Overview by Posen *et al.* [41].

Up to today, all processes need a consecutive annealing step of at least $930\,°C$ for phase pure Nb_3Sn synthesis or $630\,°C$ with copper as flux medium [39, 40]. Fig. 1.5 shows an overview of commonly used process routes in literature after deposition. Typically, temperatures of $800\,°C$ to $1200\,°C$ for about $3\,h$ to $24\,h$ are used to inter-diffuse Nb and Sn to form Nb_3Sn.

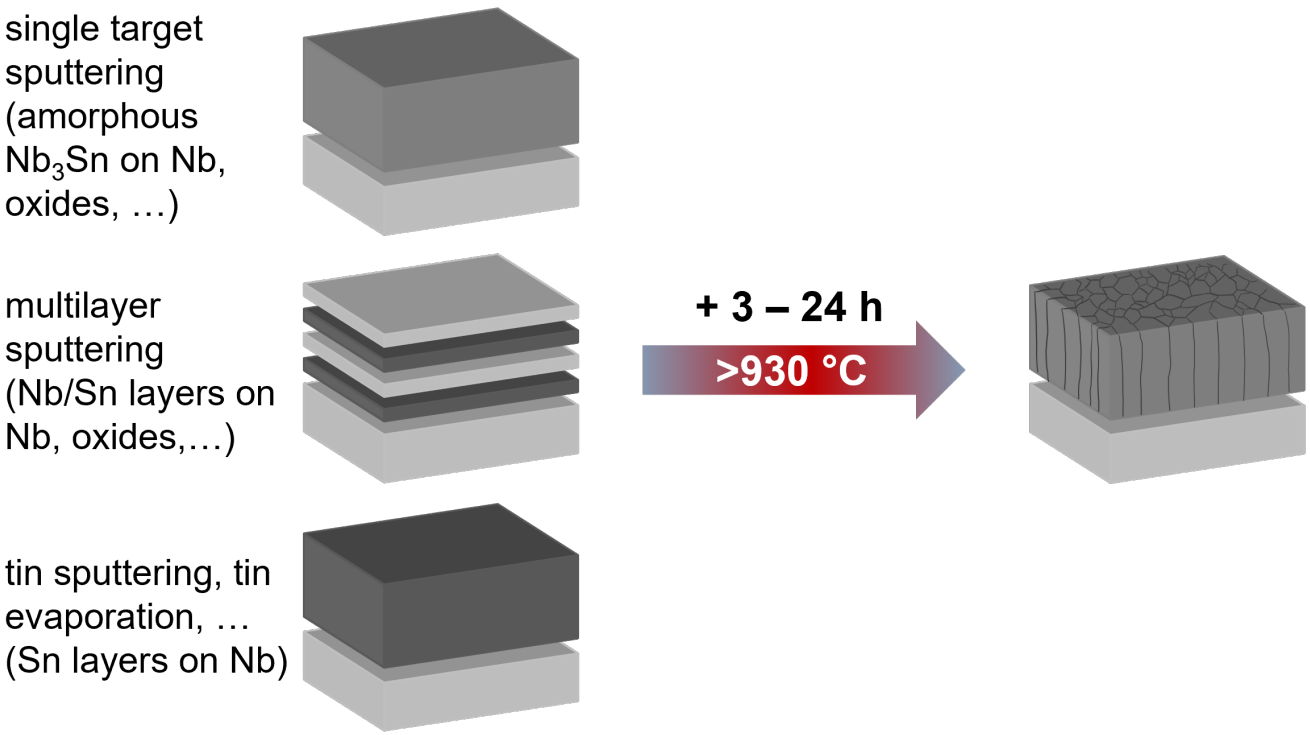

Figure 1.5.: Literature review of synthesis process routes of Nb_3Sn at typical annealing temperatures and durations.

1.7. Motivation

Although having an beneficial influence to our lives, the huge number of particle accelerators consume vast amounts of energy for operation. In times of climate change, this has become an increasing problem. Researcher all over the world dedicate their work to increase the energetic efficiency of these facilities. In this work, the goal is to improve the performance of Nb_3Sn to lower the power consumption for refrigeration. The reason for the previously discussed performance limitation of Nb_3Sn is related to the high synthesis temperatures. To decrease the synthesis temperature, a new co-sputtering process is investigated to overcome the limitation of low niobium diffusivity at low temperatures to form Nb_3Sn in excellent condition at low temperature. Sputtering is a widely used thin film process with industrial relevance. The sputtered atoms have kinetic energies in the range of several eV up to several hundred eV. In comparison to the widely used evaporation process, it is about ten times higher. Although there are also sputtering processes established for the synthesis of Nb_3Sn it was never possible to directly form the desired phase without annealing. In multilayer sputtering, it is necessary to coat the substrate near room temperature. Otherwise, the tin layer is evaporated instantly. Here, the kinetic energy can not be used to assist the phase growth. Single target sputtering likewise was not able to form the phase directly. In this scenario, the sputtering power is rather limited in comparison to the relatively high surface binding energy of the Nb_3Sn stoichiometric target. This limits the kinetic energy to an amount that is not sufficient to form the desired phase. Unlike these approaches, co-sputtering allows to sputter the metallic targets at much higher powers. This way, it is possible to reach high kinetic energies. One day, copper (coated with Nb_3Sn) could be the ideal cavity material due to its relatively cheap price and perfect heat conductivity. In sum, a low formation temperature can improve the Nb_3Sn performance as well as allows coating of copper.

2. Superconductivity

2.1. Overview of superconductivity

2.1.1. The basic phenomena of superconductivity

The resistivity of a metal as a function of the temperature is shown in Fig. 2.1. According to Mathiessen's rule (Eq. 2.1), the resistivity is the addition of one temperature dependent and one independent contribution with

$$\rho = \rho_0 + \rho_\mathrm{i}. \tag{2.1}$$

The resistivity ρ decreases with decreasing temperature and reaches a finite value ρ_0.

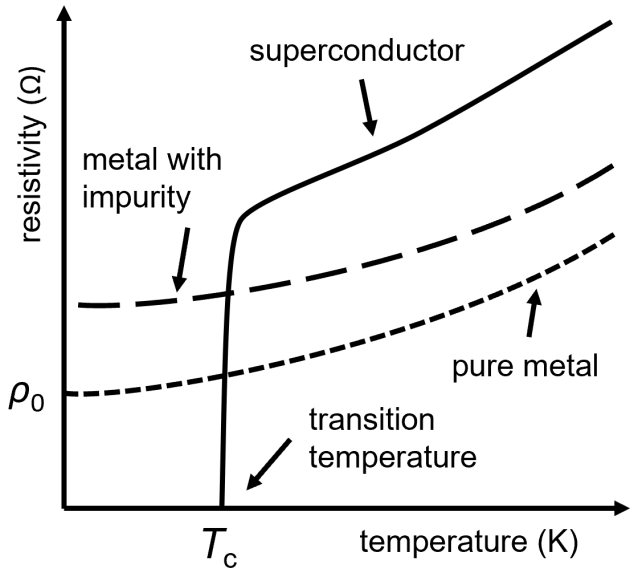

Figure 2.1.: Schematic resistivity as a function of temperature for different material groups.

Analogously to this behavior, the resistance of a superconductor decreases with decreasing temperature. At a certain temperature however, the resistance drops to zero. Below this temperature, a superconductor becomes a perfect conductor. This phenomenon was discovered by Kamerlingh Onnes for mercury in 1911 [2]. At that time, he believed that it was an intrinsic property of mercury. Later, a lot more elements

Chapter 2 and its figures are adapted from [7].

with this behavior were found. Up to the present day, it cannot be predicted which elements, and also compound materials, become superconducting.

In 1933, Meissner and Ochsenfeld made an extraordinary observation [3]. They could observe that the magnetic field is expelled from the inner volume of the superconductor in the superconducting state as shown in Fig. 2.2.

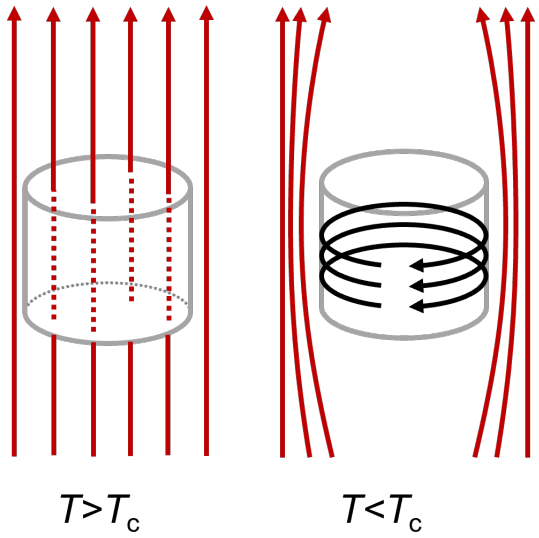

Figure 2.2.: Cylindrical superconductor in an external magnetic field higher than the critical temperature (left) and lower than the critical temperature (right).

It is clear that a perfect superconductor can not sustain an electric voltage, $E = 0$. Therefore, it follows from the Maxwell equation with

$$\nabla \times E = -\frac{\partial B}{\partial t} \tag{2.2}$$

with the magnetic field B and the electric field E that

$$E = 0 \Rightarrow \frac{\partial B}{\partial t} = 0. \tag{2.3}$$

In other words, the magnetic field is constant. This means that a trapped magnetic field inside a perfect conductor stays inside when cooled below T_c. Meissner and Ochsenfeld however, found that this is not the case for a superconductor. Both, a perfect conductor and a superconductor shield external magnetic fields due to Lenz's law. The explanation for this expulsion are screening currents that create a magnetic field in the opposite direction. However, if a perfect conductor is placed in a magnetic field and cooled below T_c, the magnetic flux stays frozen inside. For superconductors, it makes no difference if the magnetic field is applied before or after cooling to temperatures below T_c. The magnetic field is expelled from the inside in both cases. A superconductor behaves like a perfect diamagnet.

Besides the temperature, the external magnetic field is another factor that can break down the superconductivity above a certain strength. The critical external magnetic field is maximal at a temperature of $0\,\mathrm{K}$ and Eq. 2.4 follows with

$$B_c = B_0 \left\{1 - (T/T_c)^2\right\}. \tag{2.4}$$

This dependence is depicted in Fig. 2.3.

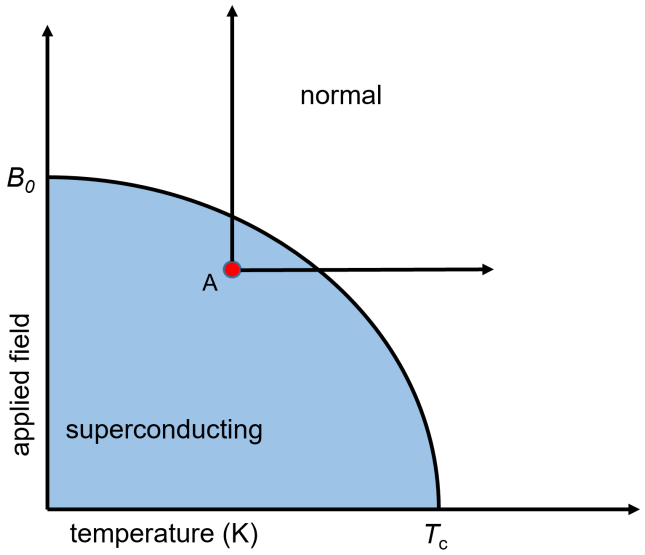

Figure 2.3.: Critical magnetic field as a function of critical temperature of a superconductor. The red dot marks a possible point of operation with the corresponding critical temperature at the given applied field and the critical field at the given temperature, respectively.

2.1.2. Perfect diamagnetism

The fact that the magnetic flux is zero inside the superconductor, leads to a magnetization M that cancels out exactly the external magnetic flux B

$$\mu_0(B_a + M) = 0. \tag{2.5}$$

From this relation, the susceptibility follows as

$$\chi = M/B_a = -1. \tag{2.6}$$

A superconductor has the magnetic susceptibility of -1 which means it is a perfect diamagnet. This value is outstanding in comparison to other known diamagnetic materials. The reason for the perfect diamagnetism are screening currents flowing in the surface. These currents never decay as they do not result in Joule heating.

Fig. 2.4 illustrates the linear dependence of Eq. 2.6. However, this relation is only valid for external fields $B_a < B_c$. As soon as the external field reaches B_c, the shielding currents break down and the magnetization vanishes.

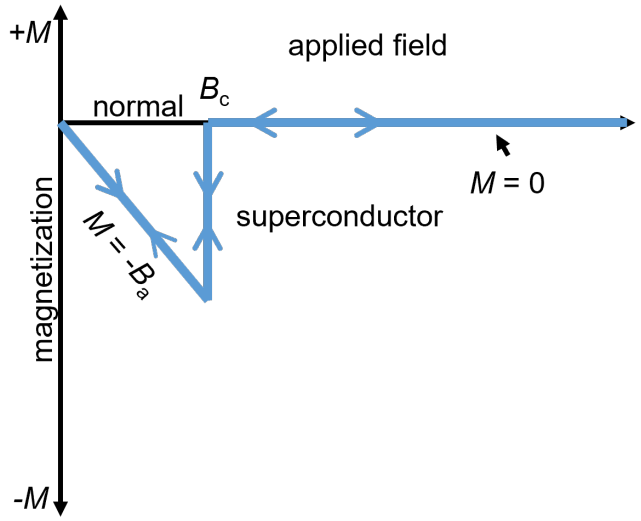

Figure 2.4.: Magnetization as a function of external magnetic field B_a of a superconductor. In the superconducting regime, M equals -B_a and in the normal conducting regime M=0.

2.1.3. The London equations

Previously, it was neglected that the shielding currents cannot flow exclusively in the surface. If these currents flew only in the surface, the current density would be infinite. In fact, these currents flow in the depth of several atomic layers. Therefore, the magnetic field penetrates the material by a small distance. Due to the shielding currents, the magnetic field drops within this distance, called the penetration depth λ. The decay of the magnetic field in dependence of the depth is shown in Fig. 2.5 and described by Eq. 2.7.

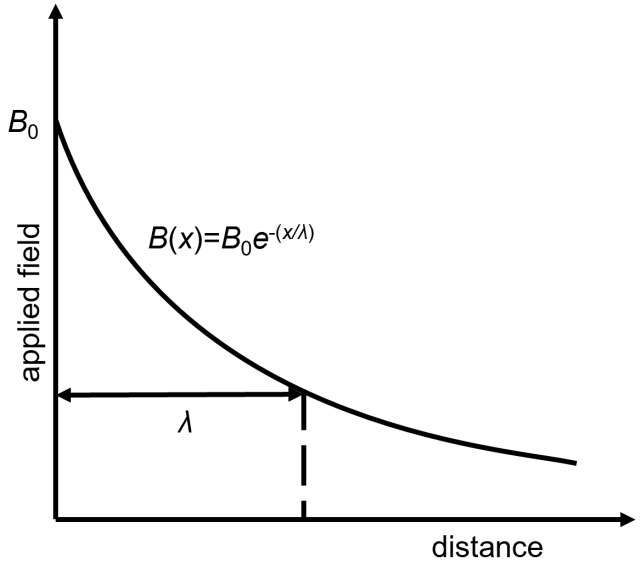

Figure 2.5.: Magnetic field as a function of distance from the surface of a superconductor. Penetration depth λ is defined as the length on which the external magnetic field strength is decreased to $1/e$ of its strength at the surface.

This relation describes the residual magnetic field

$$B(x) = B_0 e^{-(x/\lambda)} \tag{2.7}$$

as function of the applied external field at the surface B_0 and the material specific penetration depth λ. λ is defined as the distance where the magnetic field decreased to $1/e$. The temperature dependence of the penetration depth is described by Eq. 2.8 and Eq. 2.9. Close to $0\,\mathrm{K}$, λ is nearly constant, but approximately at $0.8T_\mathrm{c}$, λ can be described with

$$\lambda(T) = \frac{\lambda_0}{\left[1 - \left(\frac{T}{T_\mathrm{c}}\right)^4\right]^{\frac{1}{2}}}. \tag{2.8}$$

In the closest vicinity of T_c, λ is described by

$$\lambda(T) = \frac{\lambda_0}{\left[1 - \left(\frac{T}{T_\mathrm{c}}\right)\right]^{\frac{1}{2}}}. \tag{2.9}$$

Schematically, this temperature dependence of the penetration depth of a superconductor illustrated in Fig. 2.6.

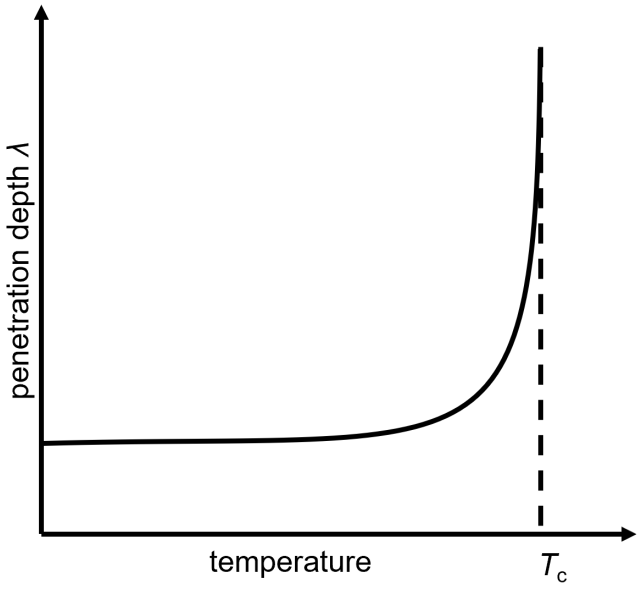

Figure 2.6.: Penetration depth as a function of temperature of a superconductor. There is a sharp increase of the penetration depth below the critical temperature.

2.1.4. Two-fluid model

Gorter and Casimir proposed a hypothesis for the explanation of the zero resistivity and the perfect diamagnetism in 1934 [42]. According to their model, normal electrons start to condense to superelectrons below the transition temperature. The total amount of charge carriers is given with

$$n = n_\mathrm{n} + n_\mathrm{s}. \tag{2.10}$$

where n is the sum of n_n normal electrons and n_s the superelectrons. These two types of charge carriers represent the two fluids. However, only the superelectrons contribute to the superconductivity. The fraction of electrons that condensed to superelectrons at a certain temperature is determined by

$$n_\mathrm{s} = n_0 \left[1 - (T/T_\mathrm{c})^4\right] \tag{2.11}$$

with the concentration of electrons n_0 above T_c. Fig. 2.7 shows this relations. While all electrons are normal electrons at around T_c, all electrons are in the superconducting state at $0\,\mathrm{K}$.

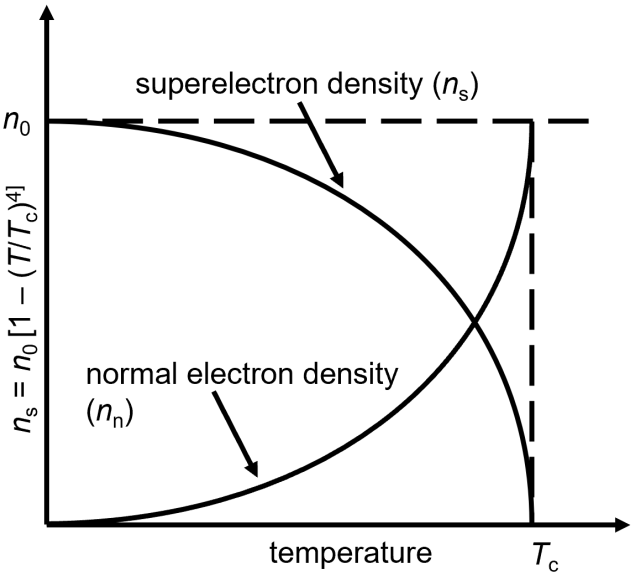

Figure 2.7.: Relative number of normal electrons and superelectron as a function of temperature of a superconductor. While the normal electron density increases with increasing temperature, the superelectron density decreases. The maximal density of normal electrons and the minimal density of superelectrons is reached at the critical temperature.

2.1.5. The Josephson effect

In 1962, Brian D. Josephson stated that a supercurrent could flow through a tunnel junction between two superconductors with zero resistance [43]. Such a tunnel junction is built by sandwiching an insulator between two superconductors. This prediction was supported experimentally and finally explained by the BCS theory (that is discussed later in section 2.2.3). According to this theory, electrons condense to electron

pairs by phonon interaction below a certain temperature T_c. These electron pairs are the so-called Cooper pairs. By phonon interaction, the Cooper pairs can flow through a superconductor without resistance and are the only species that contribute to the (shielding) supercurrents from the two fluid model. All Cooper pairs are coherent and can be described with one single wave function by

$$\Psi(\vec{r},t) = |\Psi(\vec{r},t)| \exp\left[i\phi(\vec{r},t)\right] \tag{2.12}$$

with the quantum mechanical phase ϕ. A superconductor can be described by this function where the phase is constant. However, the supercurrent undergoes a phase difference $\Delta\phi$ between the order parameters of two superconductors when a current flows between them. The current through the junction is described by

$$I = I_c \sin(\phi_1 - \phi_2) \tag{2.13}$$

with the critical current I_c through the junction. This value depends on the temperature and the junction parameter (thickness of the junction). For currents below J_c, $\Delta\phi$ adjusts such that the passage through the junction is facilitated with a constant $\Delta\phi$ or for zero voltage. Currents larger than the critical value induce a finite voltage. In Fig. 2.8, the $J-V$ characteristics are illustrated. The DC Josephson effect was first observed experimentally in 1963 by Anderson and Rowell [44]. They could show the effect using a crossed film junction.

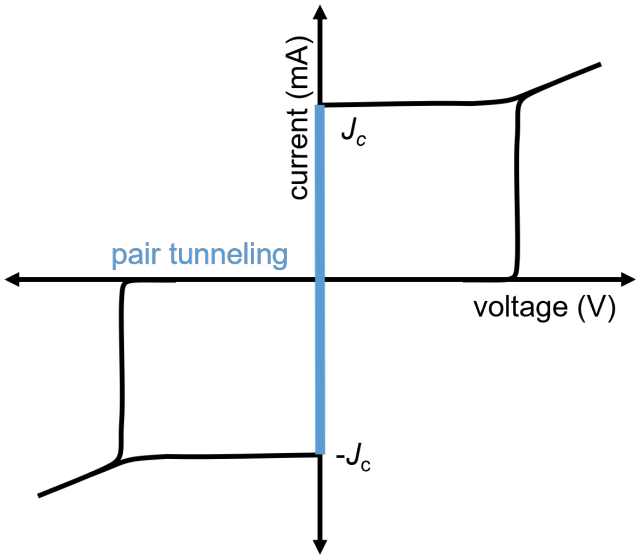

Figure 2.8.: $J-V$ characteristics of a superconductor-insulator-superconductor (SIS) junction. For increasing current, a sudden increase of the voltage is observed. Below the critical current density J_c, pair tunneling through the insulator occurs.

Taking a superconducting ring with a non-superconducting junction (weak link) as an example, the equation describes the current flow through the junction as

$$i = i_c \sin\left[(\phi_1 - \phi_2) + 2\pi\phi_{\text{junction}}/\phi_0\right]. \tag{2.14}$$

The current in the superconducting ring changes with magnetic flux through the junction that is maximal when the phase difference is $2\pi\phi_0$ and minimal when the phase difference is an odd multiple of π. Plotting the current over the magnetic flux shows oscillations driven by the phase change. The phase difference between the superconductors is given by

$$\Delta\phi = \left[\frac{2eV}{\hbar}\right] t. \tag{2.15}$$

It follows that an applied voltage V across the junction causes an alternating current with a frequency $2ev/\hbar$.

2.1.6. The concept of coherence length and positive surface energy

The coherence length ξ is another characteristic property of a superconductor in addition to the penetration depth λ. As discussed in section 2.1.5, a superconductor is phase coherent. Brian Pippard concluded that the superelectron density n_s cannot change abruptly but needs to change smoothly at the S-N interface (shown in Fig. 2.9) [45]. This distance is referred to as the coherence length ξ. The maximum value ξ_0 is found at $T{=}0\,\mathrm{K}$ in the purest state of the superconductor. While ξ_0 is an intrinsic property, ξ depends on several conditions and drops to zero at T_c. ξ is related to ξ_0 via relation

$$\xi = (\xi_0 l_\mathrm{e})^{1/2} \tag{2.16}$$

with the electronic mean free path l_e. The intrinsic coherence length ξ_0 can be calculated using the equation

$$\xi_0 = 0.18\frac{\hbar v_\mathrm{f}}{k_\mathrm{f} T_\mathrm{c}} \tag{2.17}$$

with the Fermi velocity v_f and the critical temperature T_c. Considering a S-N interface, it is clear that the interface must be in equilibrium. This means that the free energy per unit volume of both regions is equal. However, there are two contributions to the free energy of the superconducting region. One is the decrease equal to

$$g_\mathrm{n} - g_\mathrm{s} = \mu_0 B_\mathrm{c}^2/2 \tag{2.18}$$

over the distance of the coherence length ξ. The origin is the electron ordering. The other is the contribution by the flux expulsion to the positive magnetic energy equal to $\mu_0 B_\mathrm{c}^2/2$ over the distance of the penetration depth λ. These contributions cancel out each other deep in the superconducting volume. If $\xi \gg \lambda$, that is valid for most metal superconductors, there is a small positive free energy at the surface. The positive surface free energy turned out to be an important characteristic for metal superconductors, that defines the critical field B_c.

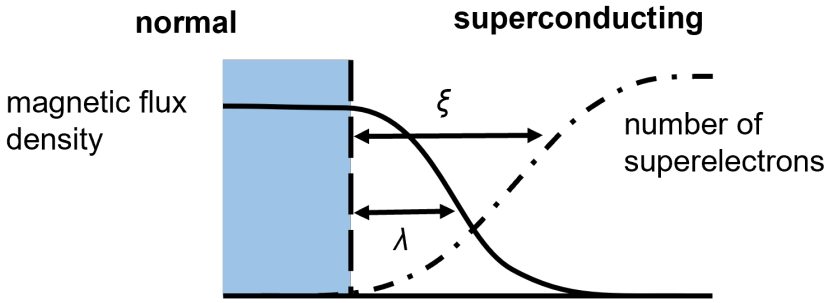

Figure 2.9.: Magnetic flux density and number of electrons as a function of the distance from the normal-superconducting interface. The number of superelectrons increases with increasing distance from the superconductor while the magnetic flux density decreases, respectively.

Abrikosov's concept of negative surface energy (type-II superconductor)

After the discovery of superconductivity in metals, researchers started to search for superconductivity in alloys and compounds. These materials have shown behavior different from the perfect diamagnetism. Abrikosov emphasized that these form a new group of superconductors, now called type-II superconductors [46].

While the type-I superconductor has only one critical magnetic field B_c, the type-II superconductor has a lower critical field B_{c1} and a higher critical field B_{c2}. In Fig. 2.10, a type-II superconductor inside an external magnetic field is shown.

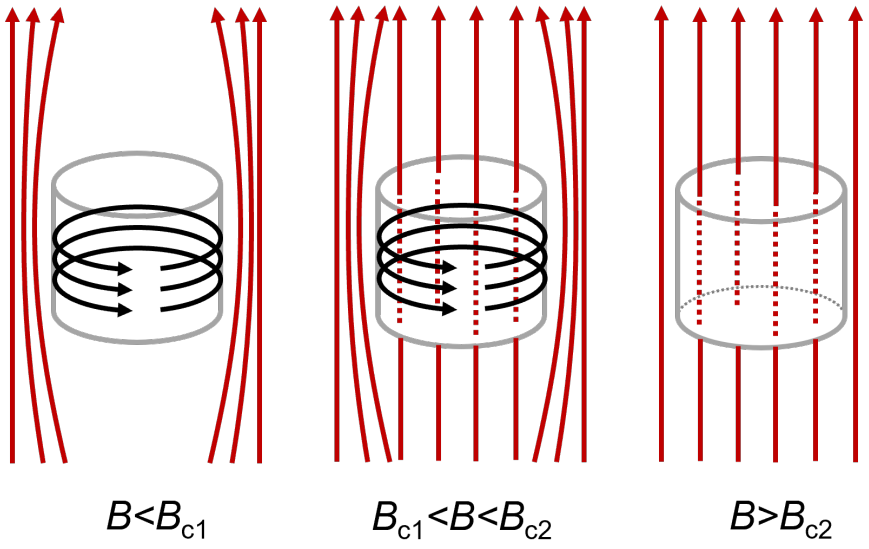

Figure 2.10.: Cylindrical type-II superconductor in an external magnetic field lower than B_{c1} (left), between B_{c1} and B_{c2} (middle) and higher than B_{c2} (right). While there is the critical field B_{c2} at which the magnetic field can fully penetrate the type-II superconductor, there is an additional critical field B_{c1} at which the magnetic field starts penetrating the type-II superconductor partially by forming vortices.

The magnetic field is only expelled from the inner volume for $B_a < B_{c1}$. Instead of the perfect shielding, type-II superconductors allow partial flux penetration in the region $B_{c1} < B_a < B_{c2}$. When the applied magnetic

field reaches B_{c2}, the flux can fully penetrate the superconductor. The intermediate state does not exist for a type-I superconductor. Here, the normal regions have a higher free energy than the superconducting regions (for $B_a < B_c$). The free energy of the superconductor increases when the normal regions grow. This is energetically unfavorable and the superconductivity breaks down at B_c. Considering a negative surface energy at the normal-superconducting interface for type-II superconductors, it follows that the free energy decreases when normal regions are formed. Thus, it becomes energetically favorable to allow partial flux penetration rather than expelling the field completely. Reconsidering that type-II superconductors are alloys and compounds with small coherence lengths, it results that the surface energy at the normal-superconducting interface is negative for materials with $\xi \ll \lambda$. To distinguish between type-I and type-II, the order parameter κ is defined with

$$\kappa = \frac{\lambda}{\xi}. \tag{2.19}$$

A superconductor is type-I, if $0 < \kappa < 1\sqrt{2}$. If $\kappa > 1\sqrt{2}$, the superconductor is type-II.

2.1.7. Lower and upper critical magnetic field of type-II superconductors

The magnetic phase diagrams of a type-I superconductor (left) and type-II superconductor (right) are shown in Fig. 2.11. As previously discussed, while the type-I has only B_c, type-II has a lower B_{c1} and higher critical magnetic field B_{c2}. For the same reason, only the superconductor type-II is of technological importance. These materials can maintain a superconducting state up to relatively high magnetic fields.

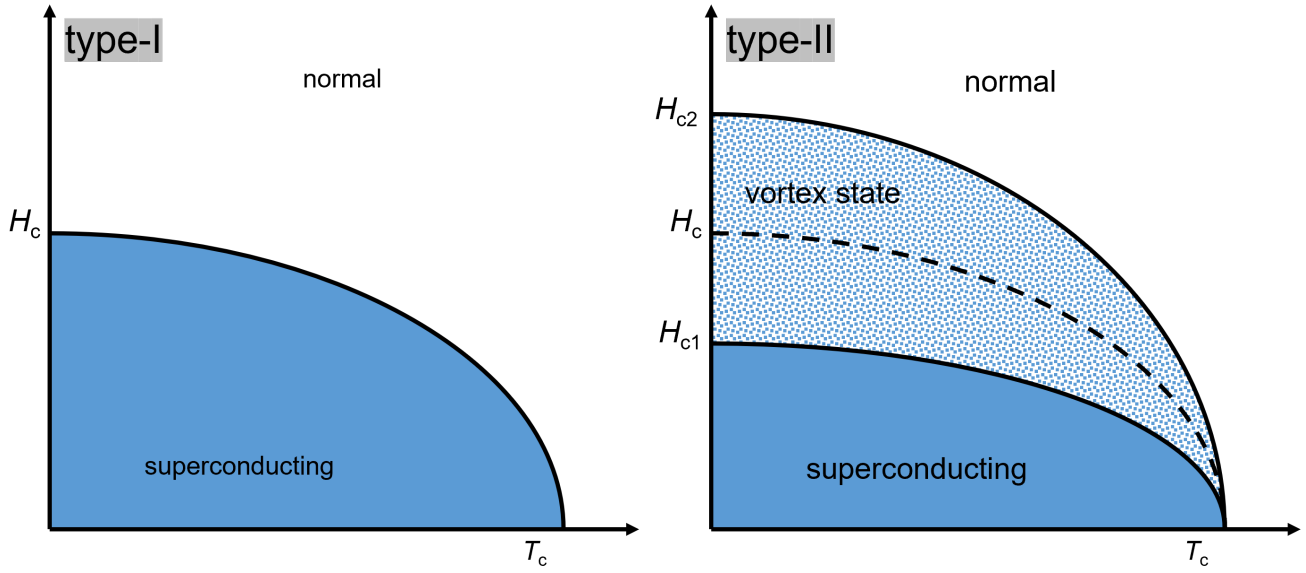

Figure 2.11.: Critical field(s) as a function of temperature for type-I superconductor and type-II superconductor. The critical field H_c is the magnetic field strength at which the magnetic field can fully penetrate the superconductor type-I. While there is the critical field H_{c2} at which the magnetic field can fully penetrate the superconductor type-II, there is an additional critical field H_{c1} at which the magnetic field starts penetrating the superconductor type-II partially by forming vortices.

The critical magnetic field B_c can be calculated with the following equation

$$B_c = [8\pi(g_n - g_s)]^{\frac{1}{2}} . \tag{2.20}$$

The lower and higher critical field of a type-II superconductor can be calculated using

$$B_{c1} = \frac{B_c}{(\kappa\sqrt{2})^{0.65}} \tag{2.21}$$

and

$$B_{c2} = \left(\sqrt{2}\right) \kappa B_c, \tag{2.22}$$

respectively. For increasing κ, B_{c1} decreases while B_{c2} increases in respect to B_c. The order parameter κ can be directly determined using the relation

$$\kappa = \frac{\left(\sqrt{2}\right) 2\pi\lambda^2\mu_0 B_c}{\Phi_0}. \tag{2.23}$$

As previously discussed, the coherence length ξ and the penetration depth λ depend on the purity of the superconductor and therefore also on the order parameter κ. The intrinsic value κ_0 can be used to calculate κ via

$$\kappa = \kappa_0 + 7.5x\sqrt{10}x10^5\gamma^{\frac{1}{2}}\rho \tag{2.24}$$

with the normal state resistivity ρ and the coefficient of electronic specific heat γ.

2.1.8. The mixed state of type-II superconductors

The macroscopic phenomenon of the type-II superconductor mixed state is discussed in the previous chapter. According to Abrikosov's concept of negative surface energy, the magnetic field can penetrate the type-II superconductor partially. This is the so-called mixed state where it is energetically favorable that the flux lines penetrate the material parallel to the magnetic field. The flux lines carry a flux quantum $\Phi = h/2e$ and form a triangular lattice (shown in Fig. 2.12) in the superconductor surface. The red colored normal cores have a diameter of 2ξ. Each of these cores is produced by a vortex of persistent current that is directed in the opposite of the screening current. The reason for the normal conducting core is found in the negative N-S surface energy. This way, the surface to volume ratio is maximal. The percolation current of a superconductor type-II flows in the whole cross-section which is not the case for a superconductor type-I where the currents only flow at the surface. While the sample remains diamagnetic and the shielding currents are flowing, an increasing field increases the core density up to B_{c2}. Increasing the field further leads to a full collapse of the superconductivity and the material becomes normal conducting.

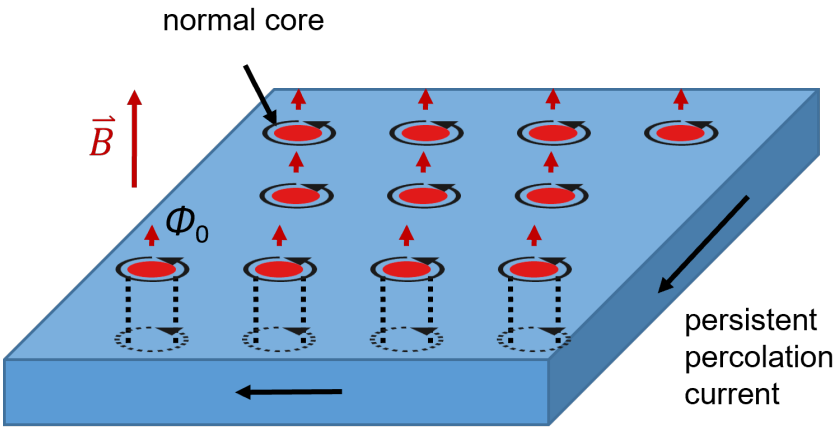

Figure 2.12.: Type-II superconductor in the mixed state. Vortices with a normal conducting core (marked in red) are shown. Each vortex contains a magnetic flux quantum.

Type-II superconductors are usually able to carry high currents in the presence of high fields. In the mixed state, the current is not affected by the vortices. However, an increasing density of vortices decreases the critical current density. Although it is said that a superconductor has zero resistance, the movement of the vortex lines generates a finite voltage. The reason is that the flux lines experience a Lorentz force under the influence of the transport current and the perpendicular field that tries to move them. It is possible to pin these flux lines to imperfections in the crystal like defects and impurities. This pinning decreases the resistance as long as the pinning force is higher than the Lorentz force. The point where the Lorentz force becomes higher than the pinning force is the critical current density. At this point, the flux lines start to move and generate some resistance that brings the superconductor into the normal state. Fig. 2.13 the dependence of the critical current density from the magnetic field, but also the difference between a clean and a dirty superconductor. It is clear that the dirty superconductor has a lot more pinning sites that increase the critical current density.

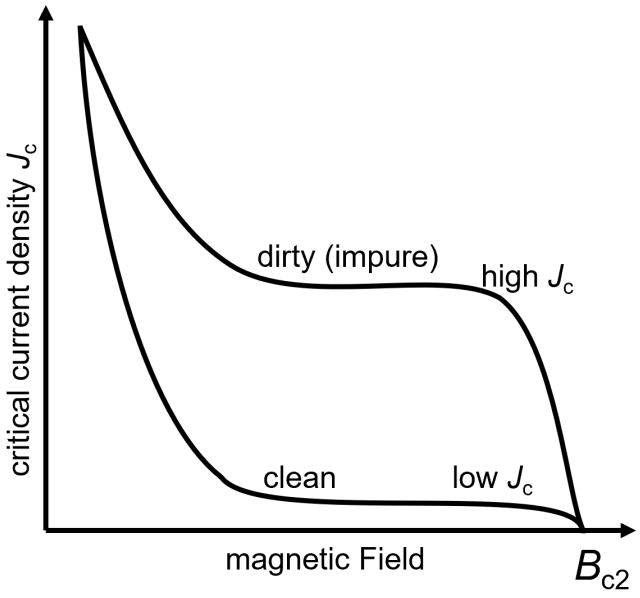

Figure 2.13.: Critical current density J as function of external magnetic field B for a type-II superconductor. Impurities increase the critical current density.

2.1.9. Magnetization in type-II superconductors

The magnetization of a type-II superconductor is analog to a type-I superconductor up to B_{c1}. Then the magnetization drops suddenly towards zero. At B_{c2} the magnetization reaches zero. In a perfectly pure superconductor, the magnetization is reversible since there are no pinning sites where flux lines could be frozen (shown in Fig. 2.14).

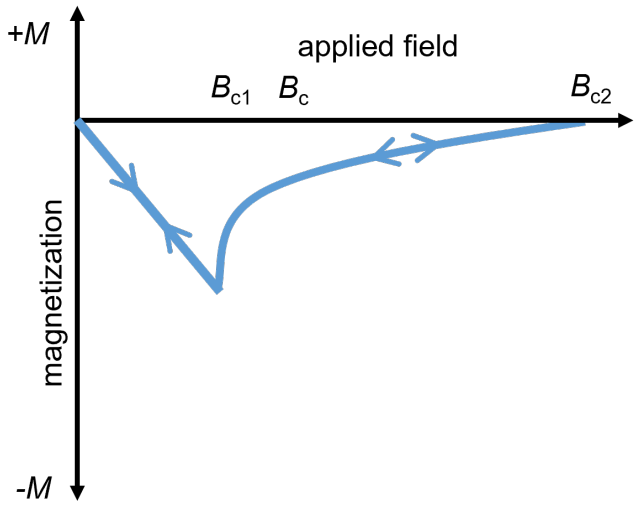

Figure 2.14.: Magnetization M as a function of the applied magnetic field B_a in a perfect type-II superconductor. For B_a<B_{c1}, M equals B_a. Above B_{c1}, M is continuously decreasing until it reaches zero at B_{c2}.

κ can be determined experimentally by

$$\left[\frac{dM}{dH}\right]_{B_{c2}} = \frac{-1}{1.16(2\kappa^2 - 1)} \tag{2.25}$$

with the slope of the $M - H$ curve near the field B_{c2} $[dM/dH]_{B_{c2}}$. The relation is, however, only valid for reversible magnetization. Real type-II superconductors show an irreversible magnetization response as shown in Fig. 2.15. The reason is the usually high density of pinning sites. In contrast for a perfect superconductor, the magnetization does not drop suddenly at B_{c1}. For this superconductors, there is a rounding of the magnetization curve at B_{c1}. Likewise, the magnetization reaches zero at B_{c2}. However, the sweep back shows a different slope, as there is remaining pinned flux in the superconductor. Flux may even be trapped permanently.

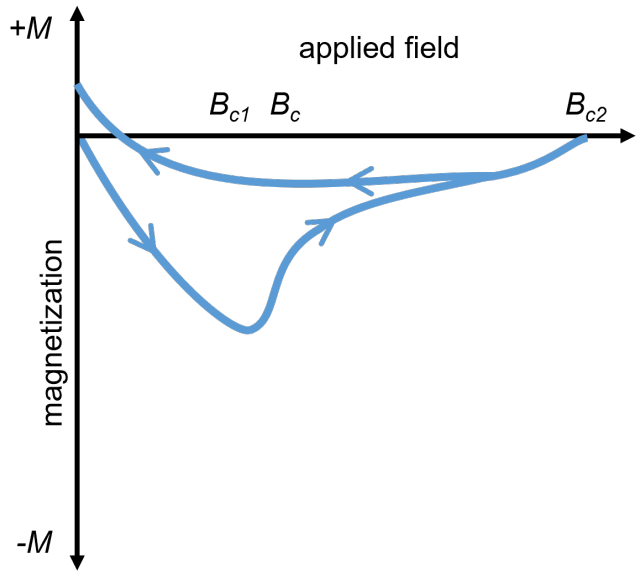

Figure 2.15.: Magnetization as a function of the applied magnetic field in a real (imperfect) type-II superconductor: zero field cooled (lower to higher fields) and field cooled (higher to lower fields). Difference between ZFC and FC curves occurs due to flux pinning.

Fig. 2.16 illustrates a typical magnetization plot for a type-II superconductor (hard superconductor) with strong flux pinning. Starting with a field free superconductor at the origin, the magnetization decreases until B_{c1} (point A). From this point, the magnetization increases and reaches zero at point B (B_{c2}). The characteristic property of a hard superconductor is the following increase of the magnetization towards the peak value at point C instead of retracing the path to point A when the magnetic field is decreased to zero. Reversing the magnetic field leads directly to an decrease of the magnetization that reaches zero at point D (-B_{c2}). At Point E, a new peak value is reached for the magnetization. A full cycle from $+B_{c2}$ to $-B_{c2}$ and back is performed. However, there is trapped flux in the superconductor. Only warming up the superconductor to the normal state and cooling at zero field can remove the trapped flux from a hard superconductor.

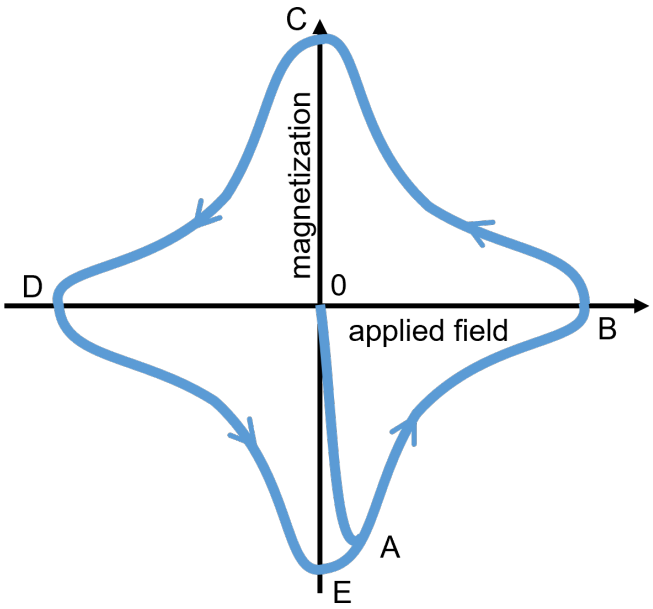

Figure 2.16.: Typical hysteresis of a hard superconductor (type-II) in the range $-B_{c2}$ to $+B_{c2}$. The difference in magnetization for the scans from B to D versus D to B is due to flux pinning.

A closer look to the hysteresis loop shows that the cycle is asymmetric. This asymmetry is the result of the magnetic moments produced by the surface screening current opposing the flux entry. The area of the hysteresis represents the dissipated energy that is created by the flux movement. It can be calculated using the relation

$$Q_{\text{hys}} = \oint M(B)dB. \tag{2.26}$$

The dissipation is transformed into heat. Such an hysteresis is an indication of effective flux pinning by imperfections.

2.1.10. Bean's critical-state model and magnetization

Bean's critical-state model is a phenomenological theory of magnetization explaining the field dependent magnetization and macroscopic penetration depth. Further, it can explain the impact of the superconductor geometry on the magnetization. In this model, a new characteristic magnetic field B^* is defined. It represents the field at that a shielding current in the whole sample cross-section is induced. This field is defined as

$$B^* = 4\pi J_c R/10 \tag{2.27}$$

with the critical current density J_c and the superconductor radius R. Following this model, the macroscopic penetration depth D_p is given by

$$D_\mathrm{p} = 10(B - B_\mathrm{c})/4\pi J_\mathrm{c}. \tag{2.28}$$

If B^* is applied to a superconductor, the penetration depth D_p equals the samples radius R. This relation is shown in Fig. 2.17 (left). In Fig. 2.17 (right) it is shown that at B^*, shielding currents at the critical current density are flowing in the whole cross-section of the superconductor.

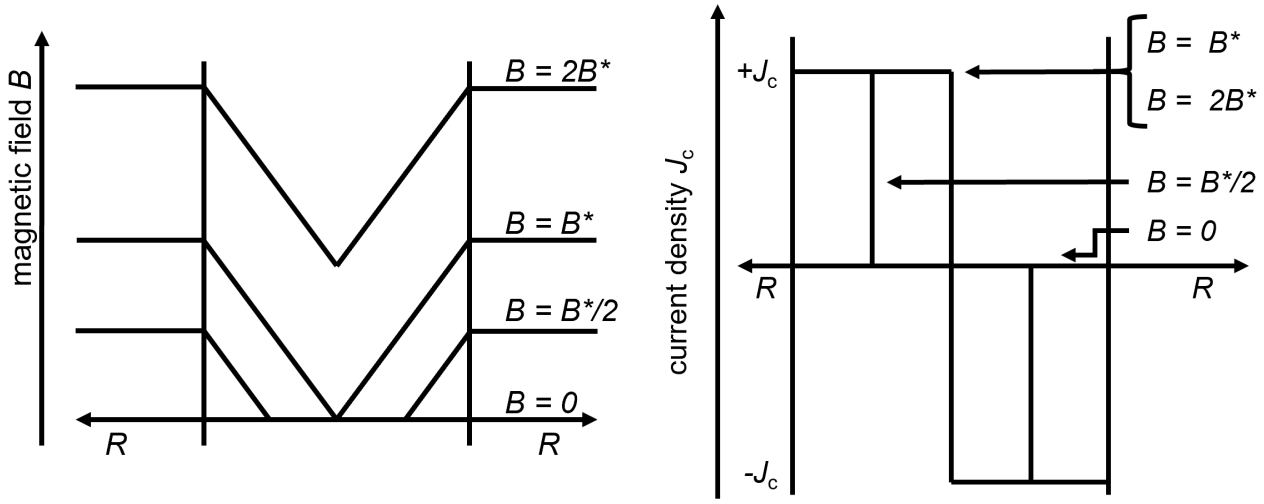

Figure 2.17.: Local magnetization and current distribution in a superconductor for increasing external magnetic field according to Bean's model.

A mathematical expression for field dependent magnetization distinguishes between three given intervals:
(i) For $0 \leq B \leq B_\mathrm{c}$

$$4\pi M = -B \tag{2.29}$$

(ii) For $B_\mathrm{c} \leq B \leq B^*$

$$4\pi M = -B + \frac{(B^2 - B_\mathrm{c}^2)}{B^*} + \frac{\left[B_\mathrm{c}^2(3B - 2B_\mathrm{c}) - B^*\right]}{3B^{*2}} \tag{2.30}$$

(iii) For $B \geq B^* + B_\mathrm{c}$

$$4\pi M = -B^*/3 \tag{2.31}$$

The model can further explain the current distribution when the applied magnetic field is removed. Fig. 2.18 shows the magnetization and current distribution when a magnetic field B_0 is applied and removed. When the magnetic field is removed, an electromotive force generates a current opposing the former current. The trapped flux is exactly half the flux at B_0. The key note of that model is that the magnetization is dependent from the dimensions of the superconductor.

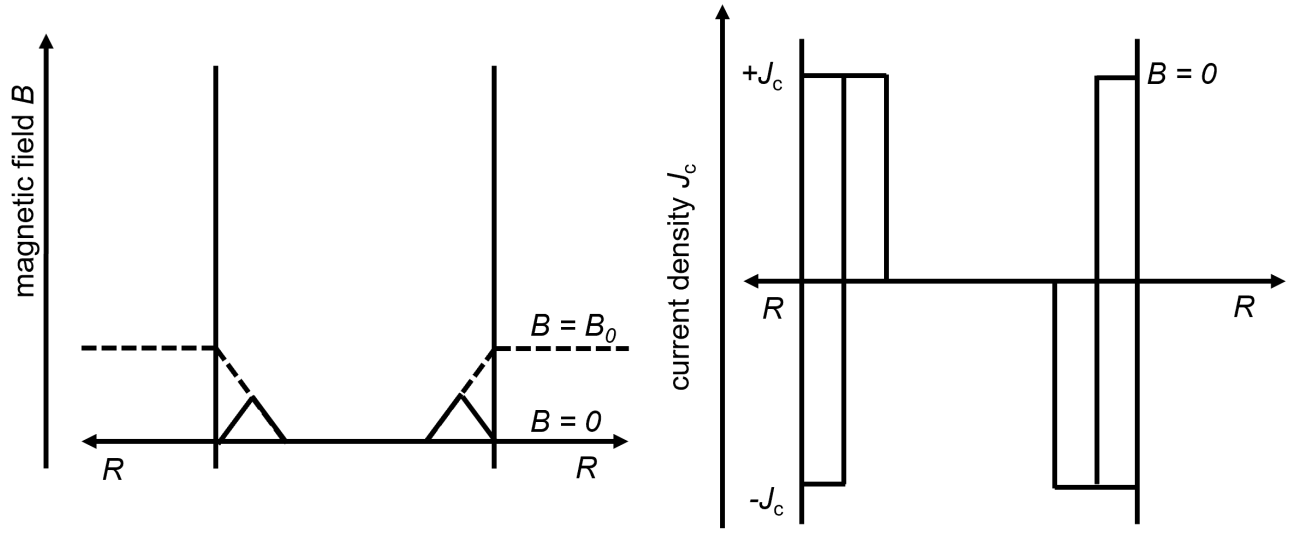

Figure 2.18.: Magnetization and current distribution in a superconductor after removing the magnetic field according to Bean's model.

2.1.11. Critical current of a type-II superconductor

Bean's model [47, 48] can be used to determine the critical current only using the magnetization. For the determination, the fact that magnetization and critical current are depending on each other is used. Fig. 2.19 shows the experimental procedure to obtain ΔM, that is the difference between the magnetization of the superconductor M_+ in the increasing and M_- decreasing external field at the same strength.

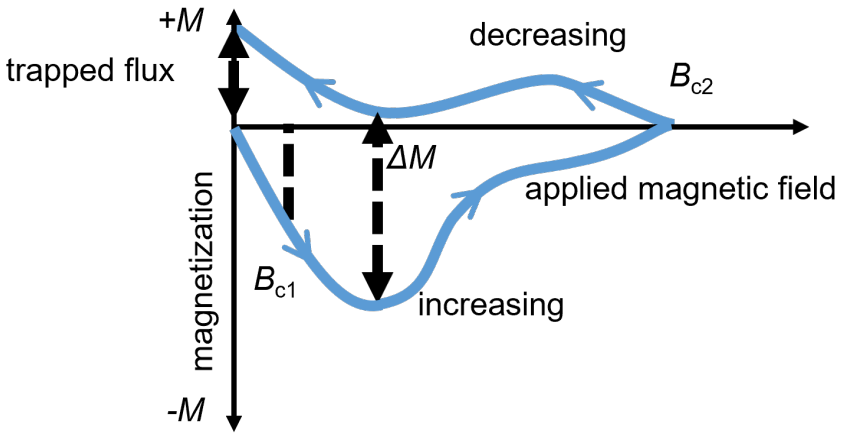

Figure 2.19.: Procedure to determine the critical current density by the magnetization. Difference in magnetization (of scan from low to high fields and scan from high to low fields) as a function of applied magnetic field is taken to determine the critical current density.

J_c in A/m^2 can be determined by the following expression

$$J_c = 2(M_+ - M_-)/d = 1.59 \times 10^6 \mu_0 \Delta M/d \tag{2.32}$$

with the diameter d of the superconductor in m (orthogonal to the external magnetic field) and $\mu_0\ \Delta M$ in T. The equation in cgs units simplifies to

$$J_\mathrm{c} = 30\Delta M/d(A/cm^2) \tag{2.33}$$

where d is in cm.

2.1.12. Degradation and flux jump in type-II superconductors

Some superconductors quench at current densities below the value of small samples. This phenomenon was believed to happen because of flux jumps or premature quenching. Whenever an external field is applied to a superconductor, a shielding current starts to flow in the surface region. This results in a small heat of magnetization that increases the temperature of the superconductor by ΔT_1. Since the critical current density is temperature dependent, the shielding current density is decreasing. This in return allows deeper penetration of the superconductor. The deeper penetration causes a second heat up by ΔT_2 that once more can cause a deeper penetration and another heat up by ΔT_3. As a consequence of several cycles, the superconductor can quench to normal state. The phenomenon is referred to as 'thermal run-away' or 'flux jump'. In case that

$$\Delta T_2 \ll \Delta T_1 \ll \Delta T_3, \tag{2.34}$$

the superconductor can be stabilized in the superconducting state. There are two stabilization criteria: the adiabatic stability criterion and the dynamic stability criterion. Reconsidering Bean's model, it is clear that the macroscopic penetration depth is influenced by the sample radius r. The stored heat of the magnetization is given by

$$Q = \left(\frac{2\pi}{3} \times 10^{-9}\right) J_\mathrm{c}^2 r^2. \tag{2.35}$$

From this expression, it is clear that the heat produced by magnetization is proportional to the square of the thickness of the superconductor. This is called the adiabatic stability criterion. Flux jumps in superconducting cables are commonly avoided by reducing the diameter of the superconducting strands. Reducing the diameter to 1/10 decreases the heat of magnetization to only $1\,\%$. The other criterion is the dynamic stability criterion. Here, a technical solution is found to surround the superconductor with a good heat conductor like copper. Copper provides cryogenic stability to the superconductor by working as a shunt resistance.

2.2. Theory of superconductivity

London's theory is a phenomenological theory explaining the Meissner effect and the infinite electrical conductivity. It also gives an (approximated) explanation for the observed temperature dependence of the flux entry. This theory is only valid at temperatures close to $0\,\mathrm{K}$. The Ginzburg-Landau theory is another phenomenological theory where it is argued that a superconductor can be described using a complex wave function $\Psi(r)$ that is an order parameter $\left(n_\mathrm{s} = |\Psi(r)|^2\right)$. The description of the superconductor transition is a special case of the Ginzburg-Landau theory that is in general a theory to describe second order phase

transitions. It is valid only close to T_c, where $\Psi(r)$ is proportional to the energy gap parameter. While both theories, London's theory and the Ginzburg-Landau theory, are macroscopic theories to describe phenomenological observations of the superconductor, the BCS theory provides microscopical explanations for (1) the zero electrical resistance below T_c, (2) second order phase transition at T_c, (3) the Meissner effect, (4) the energy gap of charger carriers between normal and superconducting state, (5) a jump in specific heat at T_c and an exponential term in the electronic specific heat in the superconducting state, (6) dependence of T_c from isotopic mass and (7) the penetration depth and its temperature dependence. Superconductors follow the predictions of this theory best in the range from $0\,\mathrm{K}$ to about $1/2\ T_c$.

2.2.1. London's theory

To explain superconductivity, the London brothers started with superelectrons that do not experience resistance. This leads to continuous acceleration following relation

$$\frac{dv}{dt} = \frac{eE}{m} \tag{2.36}$$

with charge e, mass m and velocity v of the electron. Multiplying both sides with the density of superelectrons n_s and the charge e leads to

$$\frac{d}{dt}(n_s e\nu) = \left[\frac{n_s e^2}{m}\right] E. \tag{2.37}$$

Since J_s can be expressed with $(n_s ev)$ it follows that

$$\frac{d}{dt}(J_s) = \left[\frac{n_s e^2}{m}\right] E. \tag{2.38}$$

The London brothers formulated the electric field E in terms of a vector potential A with $E = -\left|\frac{\partial A}{\partial t}\right|$. Inserting this relation in previous equation it can be rewritten as

$$\frac{d}{dt}(J_s) = -\frac{n_s e^2}{m}\left[\frac{\partial A}{\partial t}\right]. \tag{2.39}$$

Integration leads finally to an expression for J_s with

$$J_s = -\left(\frac{n_s e^2}{m}\right) A \tag{2.40}$$

The magnetic field can be expressed using Ampèré's law with

$$\nabla \times B = \mu_0 J_s. \tag{2.41}$$

Inserting equation 2.40 and $A = \nabla \times B$ (relation between magnetic flux and electric field in terms of vector potential A) is given as

$$\nabla \times (\nabla \times B) = -\left[\frac{n_s e^2}{m}\right] \mu_0 B. \tag{2.42}$$

Defining the direction along the magnetic field orientation as z direction, the London equation provides a relation to describe the field in the superconductor along the x direction with

$$\frac{d^2 B(x)}{dx^2} = \frac{\mu_0 n_s e^2}{m} B\left(x\right). \tag{2.43}$$

This differential equation has a solution of type

$$B(x) = B_0 \exp(-x/\lambda). \tag{2.44}$$

The solution matches the experiment where the magnetic flux is maximal at B_0 on the superconductor surface and drops exponentially to $1/e$ at a distance of the penetration depth λ. From this solution, λ follows as

$$\lambda^2 = \frac{1}{\mu_0}\left[\frac{m}{n_s e^2}\right]. \tag{2.45}$$

According to the two fluid model, the density of superelectrons n_s is temperature dependent. This allows the London theory not only to describe the depth of flux penetration into the superconductor, but also the temperature dependence of the penetration depth. However, equations 2.44 and 2.45 can only give approximate values that differ from the experimental values. The origin of the difference might be the values of n_s, e and m for free electrons. In the end, a superconductor is not a free electron metal since the superelectrons interact coherently.

2.2.2. Ginzburg-Landau theory

The Ginzburg-Landau theory or short G-L theory is named after its authors Ginzburg and Landau describing the superconductor close to T_c phenomenologically [49]. The transition from normal to superconducting state is a second order phase transition that is similar to the ferromagnetic phase transition in metals like iron and nickel. For the superconductor, the order parameter M is replaced by a macroscopic quantum wave function $\Psi(r)$. Here, the theory formulates the free energy of a superconductor as expressed by the expansion of $\Psi(r)$. In this theory, $\Psi(r)$ can vary with location r and is treated as a wave function with $|\Psi(r)|\, e^{i\phi(r)}$ where $\phi(r)$ is the phase. The gradient of the phase at location r is related to the flowing current at the respective point. The free energy is then formulated as

$$F\left\{\Psi\left(r\right)\right\} = \int a\left|\Psi\left(r\right)\right|^2 + (b/2)\left|\Psi\left(r\right)\right|^4 + d\xi^2\left|\nabla\Psi(r) - (ie^*/\hbar)A\Psi\left(r\right)\right|^2 + (1/2)\mu_0 \int \left|B\left(r\right)^2 dr \tag{2.46}$$

with the energy density terms a, b and d. While the terms b and d are considered temperature independent, a is temperature dependent and expressed in terms of the temperature independent a_0 as

$$a = a_0 \left[T - T_c/T_c\right]. \tag{2.47}$$

ξ is a characteristic length over that $\nabla\Psi(r)$ varies and represents the coherence length. The third term contains the electromagnetic potential A since $\nabla\Psi(r)$ is proportional to the current that in turn is dependent on A. The last term represents the energy of the magnetic field B. The whole relation aims for a configuration such that the free energy with the parameters like temperature and magnetic field is at its minimum. There are several minimal free energy configurations possible that result in various superconducting parameters. The term ξ or ξ_{GL} follows with relation

$$\xi_{GL} = \frac{\hbar}{\left|2m^* a\left(T\right)\right|^{1/2}}. \tag{2.48}$$

It is defined as the characteristic length over that $\Psi(r)$ can change without significant increase in energy. At $0\,\mathrm{K}$, ξ_{GL} is approximately ξ_0 and similar to the temperature independent Pippard coherence length. Since a vanishes at temperatures close to T_c, ξ_{GL} diverges as $(T_c - T)^{-1/2}$. It must be noted that these two coherence lengths rely on the same concept, yet they are two different quantities. High impurity concentrations can lead to a strong decrease of the coherence length. For example, high pure metals have coherence lengths of several hundred nm while alloys have typically only a few tens of nm.

Flux exclusion and zero electrical resistance

The GL theory, as well as the London theory, can be used to describe the vector potential A and the electric current flowing in the superconductor. With

$$j_s\left(r\right) = -\left[\partial F/\partial A\left(r\right)\right] \tag{2.49}$$

follows using expression 2.46 as

$$j_s = -d\xi^2 \left|\Psi\right|^2 \left(\frac{e^{*2}}{\hbar^2} A\right). \tag{2.50}$$

This relation is comparable to the London equation where the proportionality depends on the order parameter $|\Psi|^2$. From this relation it can be seen that the penetration depth increases when the order parameter increases. Near T_c, $|\Psi|^2 \propto (T_c - T)$ from that follows that the penetration depth λ should be proportional to $(T_c - T)^{-1/2}$. This temperature dependence of λ is shown in Fig. 2.6 and could be confirmed experimentally. Together with the assumption that Ψ does not change spatially, the London theory is valid only if the coherence length is much smaller than the penetration depth λ. This is only the case for type-II superconductors.

Flux quantization

From previous description of the Meissner effect, it is known that the flux penetrates only a small depth of the superconductor. This means the field and the supercurrent deep in the superconductor are zero. It follows that

$$j_s = \Psi^* (r) \left[\nabla - \frac{ie^* A}{\hbar} \right] \Psi (r) = 0. \tag{2.51}$$

With $\Psi = |\Psi| e^{(i\Phi)} (r)$ the equation can be rewritten as

$$\nabla \Phi (r) - \frac{e^* A (r)}{\hbar} = 0. \tag{2.52}$$

The order parameter should only change by an integral multiple 2π on a circular path with a minimum energy. From this assumption follows

$$\oint \nabla \cdot dl = \Delta \Phi = 2n\pi \tag{2.53}$$

and finally

$$\Phi = \frac{nh}{e^*} = \Phi_0. \tag{2.54}$$

Following the GL theory, the order parameter Ψ leads to the flux quantization. In equation 2.54, e^* equals $2e$ in the microscopic theory.

GL parameter and ype-II superconductors

London's theory introduced the two quantities penetration depth λ and coherence length ξ. The GL theory provides a classification using the ratio of these quantities that is called the GL parameter

$$\kappa = \lambda / \xi. \tag{2.55}$$

Both quantities diverge as $(T_c - T)^{(-1/2)}$, while κ remains temperature independent. The GL parameter is in fact able to distinguish between type-I and type-II superconductors. $\kappa < 1/\sqrt{2}$ for most metallic superconductors (type-I) and $\kappa > y1/\sqrt{2}$ for alloy superconductors and high T_c superconductors (type-II).

2.2.3. BCS theory

Before the formulation of this theory, it was often predicted that superconductivity must be a cooperative phenomenon in that a large number of electrons take part. One reason was the very sharp transition width of only about 10^{-5} K. For the collaboration of two electrons, there are two main difficulties. One is the fact that electrons are fermions that follow Fermi-Dirac statistics. Accordingly, two electrons cannot occupy the same quantum energy state. The other fact is the Coulomb repulsion. Thus, cooperative phenomenon is not possible. Fröhlich [50] in 1950 was first to postulate that the electrons might overcome the Coulomb repulsion by either emitting or absorbing a phonon to enter the superconducting state. The formed electron pair would then behave like a boson and follow Bose-Einstein statistics. This allows to explain superconductivity as a coherent phenomenon, since bosons can condense coherently into a single

quantum state. The postulate could be confirmed by the isotope effect [51, 52]. Bardeen [53] developed independently a theory of electron-electron interaction via the exchange of a virtual phonon.

Cooper pairs

A free electron attracts the surrounding (positively) charged lattice ions. Because of a large inertia of this lattice ions, the lattice distortion is delayed and reaches its maximum distortion when the electron already passed. A typical distance for this 'delay' is given by

$$d \approx \nu_\mathrm{F} \frac{2\pi}{\omega_\mathrm{D}} \approx 100 - 1000 \text{ nm} \tag{2.56}$$

with the Debye frequency ω_D. The distorted lattice then forms an accumulation of positive charge that attracts another electron passing the same corridor. The attraction is maximum when the first electron passed the spot by the distance d. The lattice distortion is shown schematically in Fig. 2.20.

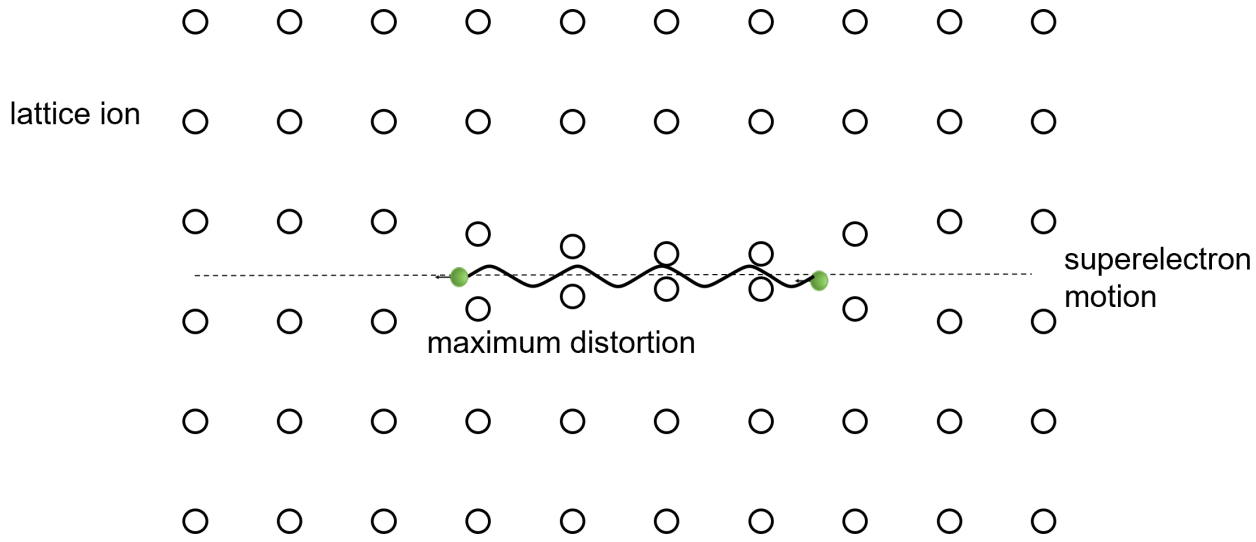

Figure 2.20.: Lattice distortion by a superelectron in a superconducting material.

In 1956, Cooper [54] stated that electrons with equal and opposite momenta $\vec{p_1} = -\vec{p_2}$ cannot occupy fully occupied energy states below the Fermi level. The reason is the Pauli exclusion principle. These electrons form pairs by phonon coupling. The so-called Cooper pairs have a binding energy of 10^{-3} eV to 10^{-4} eV. Since this binding energy is quite low, the temperature of the system must be low to preserve the Cooper pair from thermal excitation. The binding is maximum when the electrons have equal and opposite momentum. In this scenario, the total momentum of the pair is zero and the pairs are in spin singlet state. The electron distance in these Cooper pairs can be calculated using relation

$$r = \left[\frac{\hbar \nu_\mathrm{F}}{E_\mathrm{B}} \right] \tag{2.57}$$

with the binding energy E_B and the Fermi velocity ν_F. The value for r turns out to be typically 100 nm to 1000 nm that is equal to the previously mentioned distance d between two electrons for maximal attraction. The size of such a Cooper pair is large in comparison to the typical electron distance of only about 0.01 nm.

This means that the Cooper pairs usually overlap with a few others (depicted in Fig. 2.21). Bardeen, Cooper and Schrieffer showed that the system is at its lowest energetic state when all pairs have zero momentum and are phase coherent.

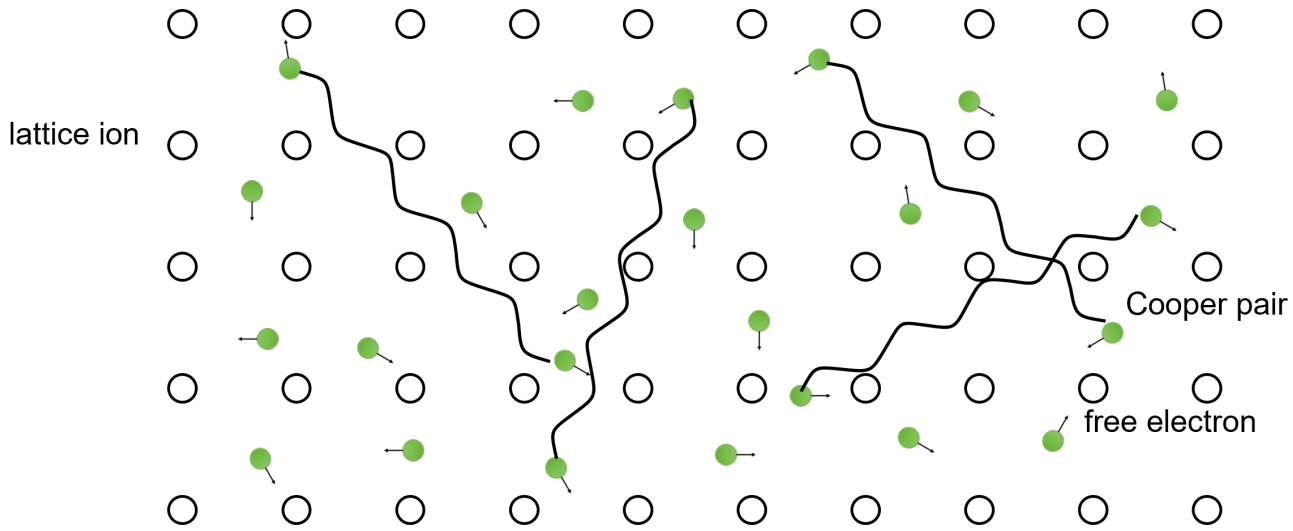

Figure 2.21.: Single electrons and Cooper pairs in a crystal lattice. Cooper pairs overlap with each other due to extended length.

Fig. 2.22 shows the energy level diagram of a normal metal at $0\,\mathrm{K}$ (left), a superconductor at $0\,\mathrm{K}$ (middle), and a superconductor above $0\,\mathrm{K}$ (right). For a metal at $0\,\mathrm{K}$, all levels up to the Fermi level are filled and all levels above are empty. For a superconductor at $0\,\mathrm{K}$, all electrons form bound pairs and condense to the ground state. The difference between the Fermi level and the ground state is the energy gap with magnitude 2Δ. At temperatures above $0\,\mathrm{K}$, thermal excitation equal to 2Δ can break electron pairs into quasi-electrons. While some electrons occupy levels above the Fermi level, some Cooper pairs stay in the ground state.

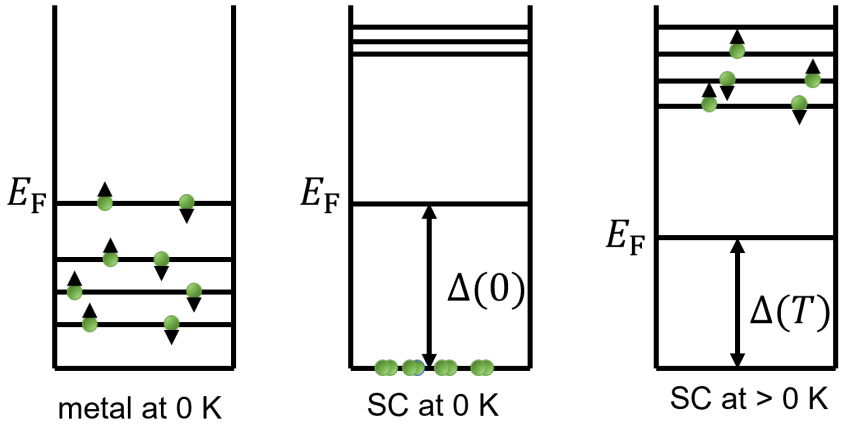

Figure 2.22.: Energy level diagram of a normal conducting metal at $0\,\mathrm{K}$ (left), a superconductor at $0\,\mathrm{K}$ (middle), and a superconductor above $0\,\mathrm{K}$ (right).

Formulation of the microscopic theory

The BCS theory uses the discussed Cooper pair formation as base to describe superconductivity microscopically. An attractive force (mediated by phonons) can start the condensation process of two electrons into the ground state (formation of Cooper pairs). The over-all electron-electron interaction is only attractive in the case that the energetic difference between the electrons is less than the phonon energy $\hbar\omega$. A superconductor goes into the superconducting state when the attractive force between the electrons is stronger than the repulsive Coulomb interaction. The momentum of the electrons is conserved when the pair is formed. The total momentum follows as

$$(k_1 + k_2) = (k_1^{'} + k_2^{'}) \tag{2.58}$$

with the momentum of the free electrons $k_{1,2}$ and the momentum of the paired electrons $k^{'} - 1, 2$. All condensed pairs are in the BCS ground state and cannot be distinguished anymore. The BCS ground state is highly ordered and the reason for most properties of the superconductor.

Transition temperature

The Cooper pair stability condition $kT_\mathrm{c} \ll \hbar\omega$ originates from ground state equations where the solution is given by

$$kT_\mathrm{c} = 1.14\hbar\omega \exp\left[-\frac{1}{N(0)V}\right] \tag{2.59}$$

with the density of electron states of spin per unit energy at the Fermi level $N(0)$ and the electron-phonon interaction parameter V. From this expression, it can be seen that T_c is proportional to the phonon frequency $\hbar\omega$. It can be further seen that T_c is a function of the electron concentration. As a consequence, T_c is dependent from alloying or the applied external pressure.

The energy gap

A very interesting observation is that the energy gap normalized to the value at $0\,\mathrm{K}$ when plotted over T normalized to T_c (T/T_c) becomes a universal curve for all superconducting materials. This means that it is possible to formulate a universal expression given with

$$2\Delta = 3.5kT_\mathrm{c}. \tag{2.60}$$

While this curve is nearly independent from the temperature close to $0\,\mathrm{K}$ (almost flat slope), the impact gets stronger for temperatures close to T_c. This relationship is given by

$$2\Delta = 3.2kT_\mathrm{c}\left[1 - (T/T_\mathrm{c})\right]^{1/2}. \tag{2.61}$$

Critical field

According to equation 2.4, the critical field B_c varies with $1 - (T/T_\mathrm{c})^2$ that is in accordance with the Gorter-Casimir two-fluid model. The BCS theory provides another prediction for the temperature dependence.

Experimental data is found to be usually between the two predictions of BCS theory and two-fluid model with a maximal deviation of $4\,\%$. The critical field at $0\,\mathrm{K}$ is given by

$$B_{\mathrm{c},0} = \left[4\pi N\left(0\right)\right]^{1/2} \Delta\left(0\right) = 1.75\left[4\pi N\left(0\right)\right]^{1/2} kT_{\mathrm{c}} \tag{2.62}$$

where $2\Delta(0)$ is the energy gap at $0\,\mathrm{K}$ and the density of states $N(0)$ from a unit volume.

2.3. Superconductivity of thin films

The transition of a thin film superconductor from superconducting to normal state is a second order transition. For this reason, the GL equation can be reduced such that only the expression

$$\left|\Psi\right|^2 = \Psi_{\propto}^2 \left(1 - \frac{d^2 H^2}{24\lambda^2 H_{\mathrm{c}}^2}\right) \tag{2.63}$$

remains where λ corresponds to λ_{eff} in zero field. It follows, that the film gets normal conducting, for $\left|\Psi\right|^2 \to 0$, when $H - H_{\mathrm{c}||}$, given by

$$H_{\mathrm{c}||} = 2\sqrt{6}\frac{H_{\mathrm{c}}\lambda}{d}. \tag{2.64}$$

This means that the parallel critical field can be higher than the bulk critical field, if d/λ is small enough. The reason is the small diamagnetic energy of the thin film in comparison to bulk of same volume. Reformulating Eq. 2.63 in terms of $H_{\mathrm{c}||}$ leads to

$$\frac{\left|\Psi\right|^2}{\Psi_{\propto}^2} = 1 - \frac{d^2 H^2}{24\lambda^2 H_{\mathrm{c}}^2}. \tag{2.65}$$

Reconsidering that $\Psi \propto \Delta$, shows that the energy gap tends to zero for increasing $H_{\mathrm{c}||}$. This behavior was confirmed by electron tunneling experiments [55].

As long as the superconducting film has a second order transition, Eq. 2.64 remains valid. As a result, it follows that $\left|\Psi\right|^2 \to 0$. Therefore, $\lambda_{\mathrm{eff}} \to \infty$ and $d/\lambda\left(H\right) \to 0$. The condition for a second order transition is given with

$$d_{\mathrm{max}} = \sqrt{5}\lambda \tag{2.66}$$

for $d_{\mathrm{max}} > \sqrt{5}\lambda$, the transition is of first order with a discontinuous drop in $\left|\Psi\right|^2$ to zero. Gurevich [56] provided an expression of practical importance that shows the relation between the lower critical field H_{c1}, the thin film thickness d and the coherence length ξ with

$$\mu_0 H_{\mathrm{c1}} = \frac{2\phi_0}{\pi d^2} \ln\frac{d}{\epsilon}. \tag{2.67}$$

This equation is valid in the regime $d < \lambda$.

2.4. Superconductivity at radio-frequency

The superconducting material of a cavity is penetrated by a microwave field. Superconductivity in microwave fields relies on the same phenomena, yet it is essentially different from direct-current applications. The reason is that in alternating-current applications, the applied magnetic field penetrates a thin surface layer. This causes power dissipation that is given by

$$R_{\text{surf}} = \frac{1}{\delta\sigma} \tag{2.68}$$

with the skin depth δ and the normal conductivity of the metal σ.

2.4.1. Radio-frequency dissipation in superconductors

The response of the superconductor to the microwave field with radio-frequency can be explained using the two-fluid model. Here, the current is carried by Cooper pairs and free electrons with total current density $J = J_{\text{n}} + J_{\text{s}}$ and total conductivity $\sigma = \sigma_{\text{n}} + \sigma_{\text{s}}$. The surface resistivity is the real part of the complex surface impedance and can be expressed with

$$R_{\text{surf}} = Re\left(\frac{1}{\lambda_{\text{L}}\left(\sigma_{\text{n}} + \sigma_{\text{s}}\right)}\right) = \frac{1}{\lambda_{\text{L}}}\frac{\sigma_{\text{n}}}{\sigma_{\text{n}}^2 + \sigma_{\text{s}}^2}. \tag{2.69}$$

It is clear that $\sigma_{\text{n}}^2 \ll \sigma_{\text{s}}^2$ at radio-frequency and therefore, σ_{n}^2 can be neglected in the relation. The R_{surf} ends up to be proportional to σ_{n} which is a surprising result. σ_{n} can be formulated by the Drude expression

$$\sigma_{\text{n}} = \frac{n_{\text{n}} e^2 l}{m_{\text{e}} \nu_{\text{F}}} \tag{2.70}$$

with the density of unpaired electrons n_{n}, their mean free path l and the Fermi velocity ν_{F}. Taking the undoped semiconductor with intrinsic conductivity as an analogy, one can get the relation $n_{\text{n}} \propto exp(-E_{\text{g}}/(2k_{\text{B}}T))$ that leads to

$$\sigma_{\text{n}} \propto l \exp\left(\Delta\left(T\right)/\left(k_{\text{B}}T\right)\right) \tag{2.71}$$

Inserting σ_{s} with $\mu_0\lambda_{\text{L}}^2\omega$ and $2\Delta(T) \approx 2\Delta(0) = 3k_B T_{\text{c}}$ leads to

$$R_{\text{surf}} \propto \lambda_{\text{L}}^3\omega^2 l \exp(-1.75T_{\text{c}}/T). \tag{2.72}$$

Since this equation uses postulates from the BCS theory, it is often referred to as R_{BCS}. From this relation, it can be seen that the resistivity has operation related influences like temperature and frequency, but also material related dependencies like normal conductivity and critical temperature. This must be clearly considered when choosing the superconducting material for radio-frequency applications. Fig. 2.23 shows a cross-section of the superconductor in a microwave field trying to give an explanation for the previously discussed contributions to the power losses in radio-frequency application. As mentioned before, the power loss originates from the normal electrons in the superconductor. According to the two fluid model, there

exist normal electrons even below the critical temperature deep in the superconductor above 0 K (in relation to the critical temperature). This shows clearly that the operation temperature has an impact on the resistance. Additionally, the penetration depth is an important property that influences the volume in the surface region where normal electrons contribute to the resistance.

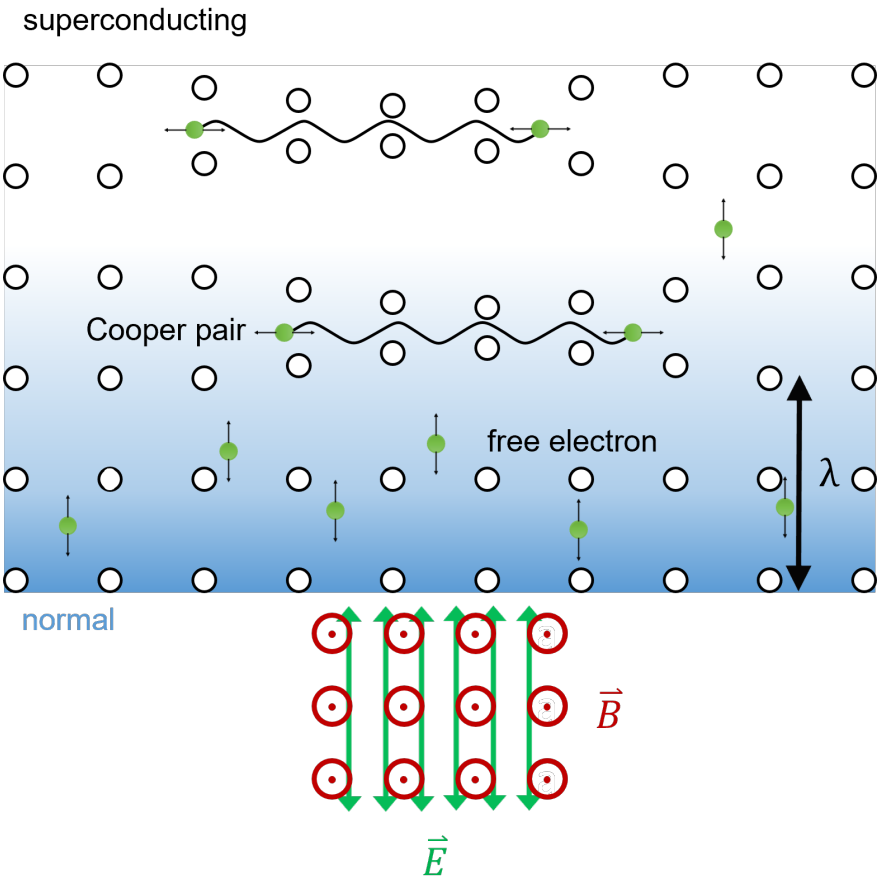

Figure 2.23.: Atomic scale cross-section of an SRF cavity wall. Magnetic field in surface plane of the cavity wall follows from the change in applied electric field. Electric field at cavity wall oscillates perpendicular to the surface. Oscillating shielding currents (Cooper pairs) perpendicular to the magnetic field are induced in the surface region. Normal electrons in the surface region start to oscillate accelerated by the electric field. Collisions between electrons and lattice cause RF power losses. The effect of the magnetic field on the electrons is neglected.

The impact of the frequency however, can be explained by the probability of the normal electrons to collide with lattice ions. Obviously, the probability increases with the amount of cycles per unit time.

2.4.2. Superheating field H_{SH}

So far, only the critical fields H_{c} for a type-I superconductor and $H_{\mathrm{c1,2}}$ for a type-II superconductor in equilibrium conditions are discussed. However, the application at radio-frequency requires to introduce the metastable condition of a superconductor. When an external magnetic field is increased, it reaches a value at that flux penetrates the superconductor. Since the work of Bean and Livingston, it is known that an energy barrier works against flux penetration [57]. At a certain strength the barrier vanishes and the flux

penetrates the superconductor that then enters the mixed state. The transition of a superconductor from superconducting to normal state is of first order at $T = T_c(H)$ that involves latent heat. Since an imperfect superconductor has nucleation centers, the superconducting state can be maintained metastably above H_c. In DC fields, the positive surface energy of a type-I superconductor allows that the Meissner state can persist up to the superheating field H_{SH} ($>H_c$). At this field the surface energy per unit area becomes zero. Superconductors of type-II can maintain the Meissner state as well as the type-I superconductors above H_{c1}. Christiansen *et al.* [58] derived a relation for the superheating field with

$$\frac{H_{SH}(\kappa)}{\sqrt{2}H_c} \approx \frac{\sqrt{10}}{6} + \frac{0.3852}{\sqrt{\kappa}} \tag{2.73}$$

where H_c is the thermodynamical critical field. The nucleation time of a vortex is large in comparison to a period in radio-frequency. In RF mode, the field there is a field where the vortices start to penetrate the material called H_c^{RF}. This field is estimated to equal the superheating field H_{SH} of the DC mode [59]. The point where the SRF cavity is operated is shown by red dot in Fig. 2.24.

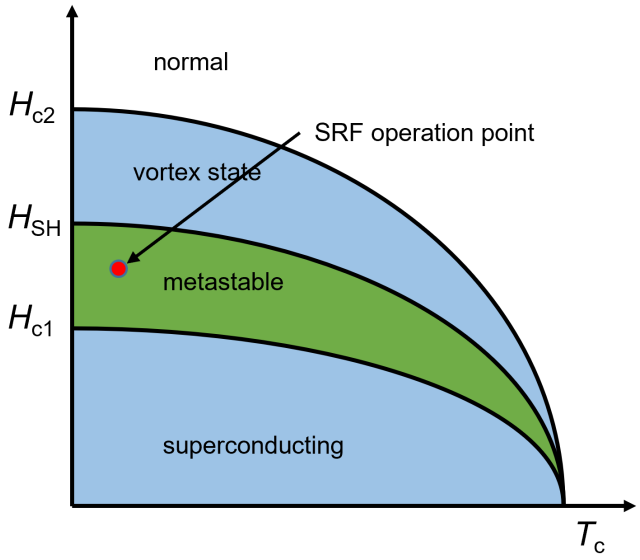

Figure 2.24.: Superheating field H_{SH} as a function of temperature of a type-II superconductor at radiofrequency. SRF operation point is marked by red dot.

The acceleration gradient is directly linked to the magnetic field on the cavity surface. Therefore, the acceleration gradient is chosen to result in a magnetic field slightly below H_{SH}.

3. Nb_3Sn for SRF application

3.1. Choosing the best SRF material

In DC applications, the decision for the right superconducting material is relatively simple. There are only a few relevant key figures, like $H_{c1,2}$, J_c or T_c, that must be considered. In SRF applications however, many more key figures must be considered. The state-of-the-art material is bulk niobium. Niobium has the highest critical temperature among all elements (≈ 9.3 K) [41], a low surface resistivity [60], a lower critical field of 130 mT and a superheating field of 250 mT [61], and good thermal conductivity [62]. Although it is cost-intense to produce high purity niobium sheets, the cavity manufacturing is relatively simple with deep drawing, welding and several polishing steps. Researchers around the globe could elaborate many techniques to improve the performance of niobium that included decreasing the impurity concentration [63] or doping [64, 65, 66]. However, it is not possible to improve the niobium performance any further. Still, niobium reaches the highest accelerating gradients that however, drop rapidly at temperatures above 2 K [67] that is related to the critical temperature. Table 3.1 provides an overview of materials that were considered to replace niobium in the next generation SRF cavities.

Table 3.1.: Properties of candidates for SRF application. [61].

Material	T_c [K]	ρ_n [$\mu\Omega cm$]	H_c [T]	H_{c1} [T]	H_{c2} [T]	λ [nm]	Δ [meV]	ξ [nm]
Nb	9.23	2	0.2	0.18	0.28	40	1.5	35
NbN	16.2	70	0.23	0.02	15	200-350	2.6	3-5
NbTiN	17.3	35		0.03	15	150-200	2.8	5
Nb_3Sn	18	8-20	0.54	0.05	28	80-100	3.1	4
V_3Si	17	4	0.72	0.072	24.5	179	2.5	3.5
Nb_3Al	18.7	54			33	210	3	
Mo_3Re	15	10-30	0.43	0.03	3.5	140		5
MgB_2	40	0.1-10	0.43	0.03	3.5-60	140	2.3/7.2	5
Pnictides	30-55		0.5-0.9	30	50-135	200	10-20	2

The overview shows clearly that it is not possible to choose the best performing material in every category. The overall benchmark of a cavity is the quality factor Q that is given by

$$Q = \frac{G}{R_s} \tag{3.1}$$

with the material independent geometry factor G and the material dependent surface resistivity R_s. Thus, the material can be chosen independently from the cavity's geometry. The surface resistivity consists of two contributions. R_BCS that was discussed in section 2.4.1 and the temperature independent residual resistivity R_res that is proportional to the concentration of impurities, grain boundaries, non-superconducting phases, or penetrating flux [61].

$$R_\mathrm{s} = R_\mathrm{BCS} + R_\mathrm{res} \tag{3.2}$$

For the normal skin effect regime $\hbar\omega < 2\Delta$ an analytical approximation (from [61]) for R_BCS can be formulated with

$$R_\mathrm{BCS} \cong \frac{R_\mathrm{n}}{\sqrt{2}} \left(\frac{\hbar\omega}{\pi\Delta}\right)^{\frac{3}{2}} \frac{\sigma_1}{\sigma_\mathrm{n}} = A\sqrt{\rho_\mathrm{n}} \frac{e^{-\frac{\Delta}{k_\mathrm{B}T}}}{\sqrt{sT_\mathrm{c}}T(1+e^{-\frac{\Delta}{k_\mathrm{B}T}})^2} \omega^2 \ln\frac{\Delta}{\hbar\omega} \tag{3.3}$$

where A is a constant weakly dependent on the material. The expression is valid for $0 < T < T_\mathrm{c}/2$. It is clear now that the material must be chosen by the lowest R_BCS where key figure from table 3.1 are taken in account.

The cryogenic efficiency of a cavity is driven by the so-called Q-factor. So far, the critical fields have been left out from this discussion. However, the acceleration gradient is limited by the superheating field. Such high critical fields can reduce the accelerator size. This means that a higher critical field can indirectly increase the cryogenic efficiency.

Setting the operational parameters $T = 4\,\mathrm{K}$ and $\omega = 2\pi \times 1.3 \times 10^9\,\mathrm{s}^{-1}$ allows a direct comparison of the materials in Table 3.2. The surface resistivity is normalized to that of niobium.

Table 3.2.: Surface resistivity of candidates for SRF application. Values from Tab. 3.1 inserted in Eq. 3.3.

Material	$R_\mathrm{BCS}/R_\mathrm{BCS,Nb}$ [%]
NbN	21.5
NbTiN	8.4
Nb_3Sn	2.2
V_3Si	6.7
Nb_3Al	5.7
Mo_3Re	3.8

From that comparison, it is clear that Nb_3Sn is the best candidate for SRF application. Additionally, the superheating field of Nb_3Sn is about $420\,\mathrm{mT}$ to $440\,\mathrm{mT}$ [68, 69] that can theoretically lead to acceleration gradients twice as high as for bulk niobium. Unfortunately, the high-quality synthesis of this material is challenging.

3.2. The discovery of Nb_3Sn

In 1953, Hardy and Hulm discovered the superconductivity in the A15-class in silicides and germanides [70]. The first reported material of this class was V_3Si with a critical temperature of $17\,K$. Superconductivity in Nb_3Sn was discovered by Matthias *et. al* in 1953 [71]. They demonstrated a critical temperature of $18\,K$ measuring the inductive transition. Up to this day, it was the highest reported critical temperature. Fig. 3.1 shows the original measurement.

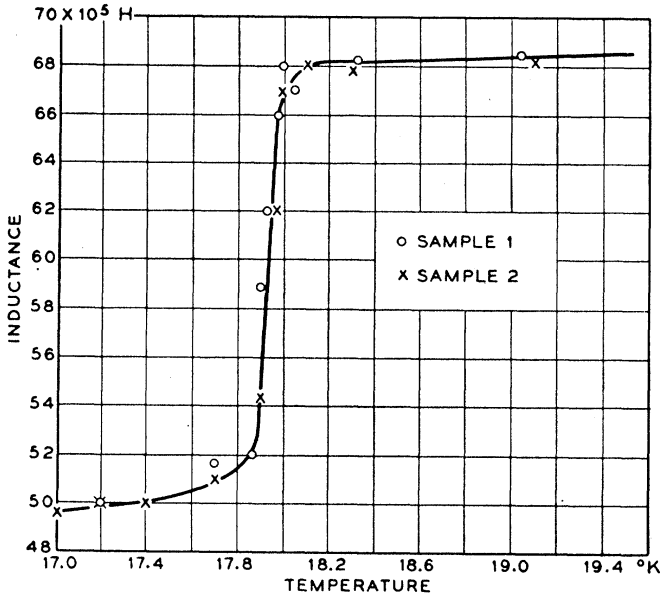

Figure 3.1.: Superconducting transition in Nb_3Sn determined by Matthias *et. al* in 1953 [71] measuring the inductance of a pick-up coil.

The samples were synthesized by dipping Nb into liquid Sn and kept at $1200\,°C$ in a quartz tube. To the present date, the highest achieved critical temperature is $18.3\,K$ that was first reported by Hanak *et al.* in 1964 [72].

3.3. The Nb-Sn material system

Fig. 3.2 illustrated the Nb-Sn phase diagram from Godeke [24]. The Nb_3Sn phase is stable in the range of $17.5\,\%$ to $26\,\%$. The Nb_3Sn phase region was corrected to the right after the phase formation $>25\,\%$ was reported. Another correction (dashed line) shows an alternative low-temperature phase diagram after Flükiger. The wide range for Nb_3Sn phase formation allows flexible synthesis of the phase. However, below $930\,°C$ other phases like Nb_6Sn_5 and $NbSn_2$ with critical temperature of $2.8\,K$ [73, 74] and $2.68\,K$ [74, 75] are formed. This is why the formation of these phases must be prevented by a fast cooling below $930\,°C$.

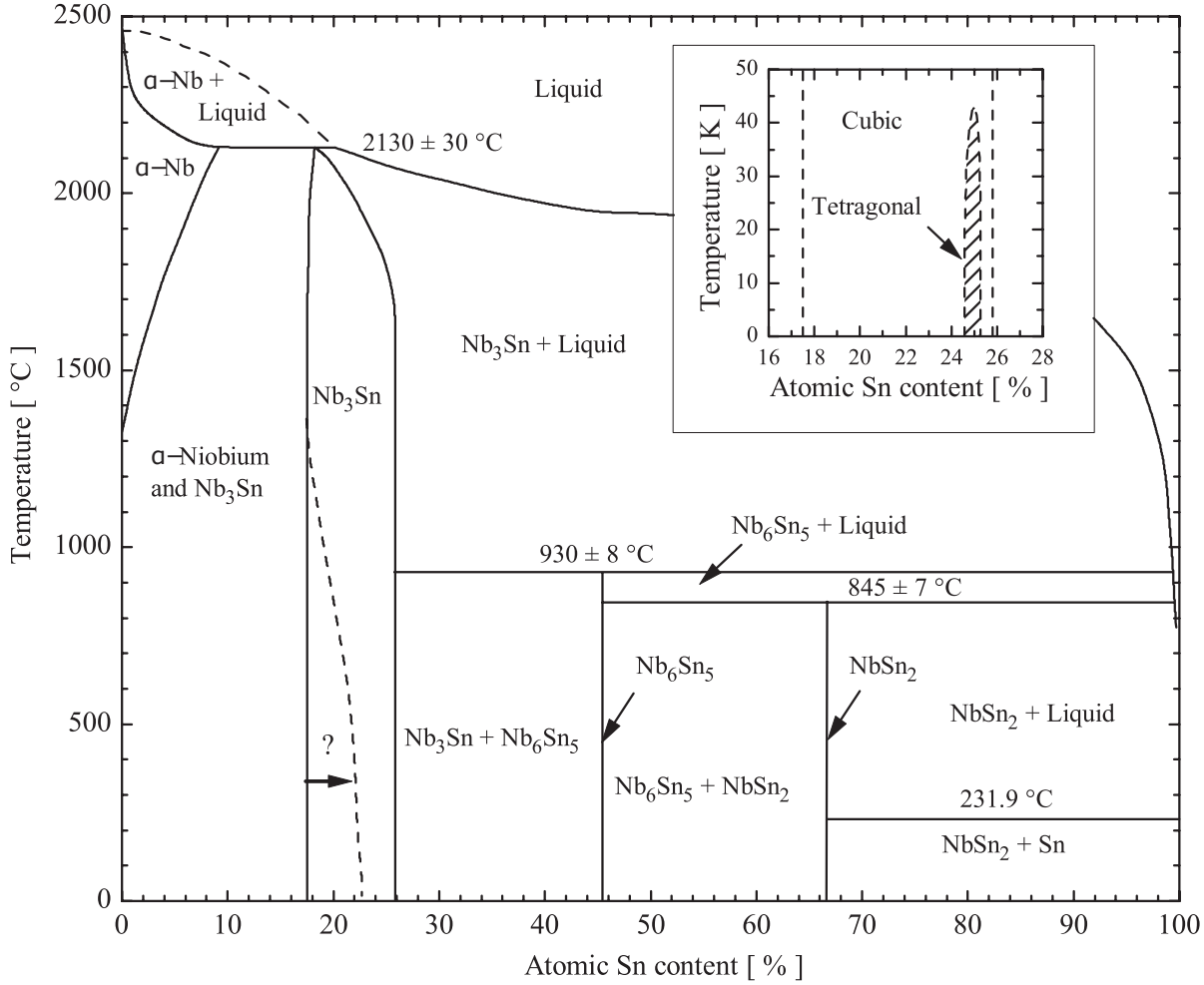

Figure 3.2.: Nb-Sn phase diagram from Godeke [24] adapted to tin-rich Nb_3Sn formation. The dashed line shows an alternative low-temperature phase diagram after Flükiger.

It is further known that the crystal structure of Nb_3Sn changes from A-15 cubic to tetragonal below $43\,K$ within a narrow range around $25\,\%$. The phase has the crystal structure of β-tungsten/Cr_3Si or the A-15 class (shown in Fig. 3.3). This class is outstanding due to the chains along the faces formed by the A-atoms (in this case Nb). The lattice constant of Nb_3Sn is $5.2908\,Å$.

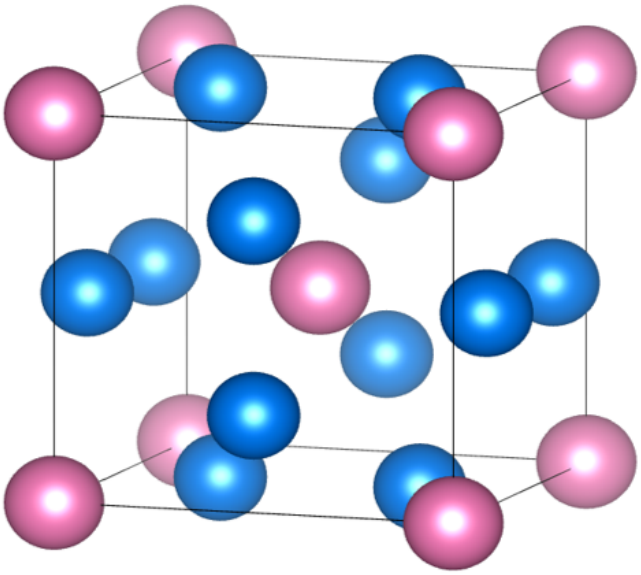

Figure 3.3.: The crystal structure of the A-15 or A_3B-type compounds. The Sn atoms are shown in pink and the Nb atoms are shown in blue.

3.4. The superconductivity of Nb_3Sn

The peculiar superconducting properties, like isotropy, are said to come from Nb chains. Nb atoms have a distance of 0.265 nm in the stoichiometric composition [76] that results in a narrow peak in the d-band. This in turn results in a very high density of states (DOS) near the Fermi level. The high critical temperature of Nb_3Sn in comparison to bcc Nb is believed to come from this high DOS. Deviations of the critical temperature from the optimal value are often correlated with the long range ordering of Nb_3Sn [77, 78]. This can be explained by the change of the Nb chains and the influence on the DOS peak. Although low tin content leads to tin vacancies, they are believed to be unstable and compensated by niobium anti-site occupation [77, 79]. Such anti-site Nb atoms cause their own broad d-band at the cost of the electrons from the Nb chain peak. This explanation is confirmed by the critical temperature of the metastable Nb_3Nb structure that is about $5.2\,\mathrm{K}$ [77]. Since this value is lower than the critical temperature of Nb, the explanation is the broad d-band caused by the Sn-site Nb atoms [80]. The lattice parameter as a function of the tin content was determined experimentally by Devantay [76] and added to experimental results from Vieland [81]. Figure 3.4 (left) provides a relation of the lattice parameter a in dependence of the tin content β based on experimental data.

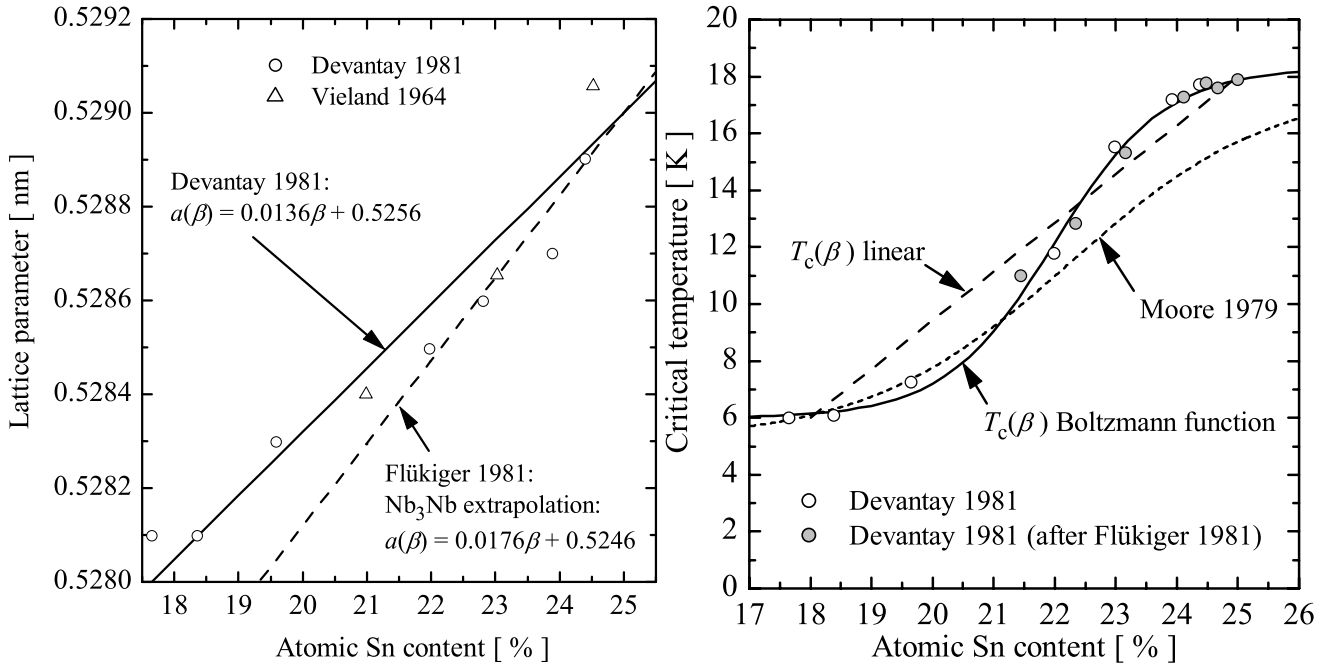

Figure 3.4.: Critical temperature as a function of the tin content (left) and the lattice parameter as a function the tin content (right) of the Nb-Sn material system [24].

Figure 3.4 (right) shows the influence of the tin content on the critical temperature. The fitted Boltzmann function is based on the experimental data from Devantay [76] and Flükiger [82]. Devantay provides a relation to summarize the result given by

$$T_c(\beta) = \frac{12}{0.07}(\beta - 0.18) + 6\ [\mathrm{K}]. \tag{3.4}$$

3.5. The synthesis of Nb_3Sn

There are many mature bulk processes to synthesize Nb_3Sn for high magnetic field generation. The most important processes are (1) the bronze process, (2) the internal tin process, (3) the jelly roll process and (4) the in situ process. Since Nb_3Sn is brittle [39], the bulk processes cannot synthesize a bulk Nb_3Sn cavity. For this reason, thin film coating of a carrier cavity is the technological solution. However, bulk processes show that the most important process parameter, is the heat treatment. Most techniques (bulk + thin film) require such heat treatments to form Nb_3Sn and are beneficial for high critical temperature, critical fields and critical currents. Unfortunately, the performance benefit is limited by the different nature of Nb and Sn.

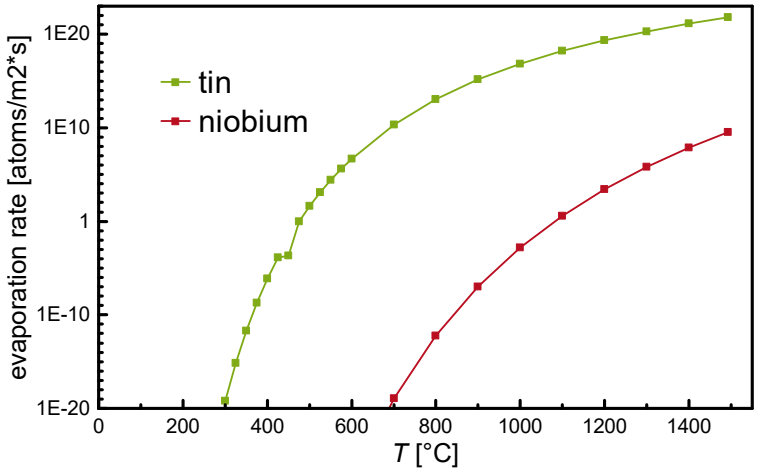

Figure 3.5.: Evaporation rate of niobium and tin as a function of the temperature at ambient pressure. While tin evaporation starts at around $300\,^{\circ}$C, niobium evaporation start at about $700\,^{\circ}$C.

Fig. 3.5 shows the evaporation rate of these elements as a function of the temperature. Although long heat treatments at high temperatures improve performance, the comparison of the evaporation rates demonstrates that long heat treatments lead to loss of tin. As a consequence, it is challenging to achieve stoichiometric tin contents all over large samples. The synthesis temperature can be lowered by additional Cu as flux medium to about $650\,^{\circ}$C to $700\,^{\circ}$C. This reduces tin loss and tin segregation. The presence of Cu is generally not expected to be within the A-15 phase and forms Cu segregations at the grain boundaries. Such a Cu matrix is the possible origin for the suppression of the critical field in superconducting wires [83].

4. Methods

4.1. Thin film growth

Thin film growth is divided in five steps: the physisorption, surface diffusion, chemisorption, nucleation, and continued growth. This mechanisms are illustrated in Fig. 4.1.

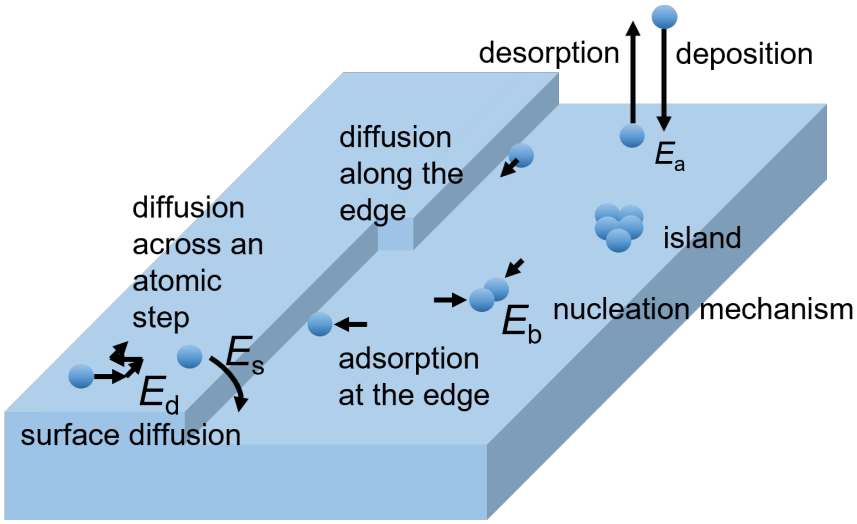

Figure 4.1.: Overview of mechanisms after atomic deposition on surface in thin film growth.

In the first step, the atoms can be either adsorbed (deposited) or desorbed. For high atom energies, even implantation in the material is possible. Single crystals are well described by the Langmuir term

$$A + S \rightleftharpoons AS \tag{4.1}$$

with gas atom A and the adsorption sites S in constant exchange with the occupied sites AS. The equilibrium constant K is given by

$$K = \frac{k_A}{k_D} = \frac{\theta}{p(1-\theta)} \tag{4.2}$$

with the equilibrium adsorption rate k_A, the equilibrium desorption rate k_D and the adsorbate gas pressure p. The change in surface coverage for adsorption θ_A and for desorption θ_D can be given by

$$\frac{d\theta_A}{dt} = k_A p N_s (1-\theta_A), \frac{d\theta_D}{dt} = -k_D p N_s \theta_D \tag{4.3}$$

with the total number of sites on the surface N_s. Physisorption is a mechanism with a weak bonding to the surface by Van-der-Waals forces with a binding energy below 1 eV. In this state, the atoms have high diffusion lengths in the range of several micrometers with a surface mobility described by

$$D = a^2 v e^{-V_s/k_B T_s} \tag{4.4}$$

with Boltzmann constant k_B, the substrate temperature T_s, the potential energy barrier between adsorption sites V_s and the effective hopping distance between adsorption sites a. The term $ve^{-V_s/k_B T_s}$ describes the site-to-site hopping rate of an adsorbed atom. D defines the distance of an atom to nucleation sites on an ideally flat surface. Alternatively, it is the distance to another adsorbed atom. During synthesis, there are two parameters to control the surface diffusion: The substrate temperature T_s and the deposition rate [84]. In vacuum thin film processes, atoms carry kinetic energies of several hundred meV up to several eV.

After surface diffusion, nucleation and chemisorption takes place. During this mechanisms, the atoms rise in binding energy by about $1\,\text{eV}$ to $10\,\text{eV}$. Chemisorbed atoms have a much lower diffusion length in the range of several nanometers. The surface energy has a strong impact on the critical nucleation size. Below this size, nuclei can dissolve. If it is overcome, the nucleus becomes a stable island. This relation is described by the total Gibbs free energy

$$\Delta G = A_1 \gamma_{iv} + A_2(\gamma_{is} - \gamma_{sv}) + V \Delta G_v \tag{4.5}$$

with the contact surface of island to vapor A_1, the surface of island to substrate A_2, the surface energy between island and vapor γ_{iv} the surface energy between island and substrate γ_{is}, the volume of the island V and the relative Gibbs free energy between gas phase and the island ΔG_v [84]. For different surface energies, three different growth modes are possible. In the case of

$$\gamma_{sv} > \gamma_{iv} + \gamma_{is}, \tag{4.6}$$

the film grows layer-by-layer. This growth mode is called Frank-van-der-Merwe growth. In the contrary case that

$$\gamma_{sv} < \gamma_{iv} + \gamma_{is}, \tag{4.7}$$

the surface diffusion is hindered and the result is island growth. This growth mode is called Vollmer-Weber growth. In this scenario, the film reduces the interface area to the substrate by island formation. The third growth mode is called Stranski-Krastanov growth. Here, the material growth layer-by-layer in the beginning and after a few layers, the surface energy changes such that the growth mode changes to island growth. This change in surface energy can be promoted by lattice misfit between the substrate and the deposited material. The thin film growth reacts to this misfit by relaxation of stresses after a few layers [84].

4.2. Sputtering

Sputtering is a physical vapor deposition (PVD) technique that is of high industrial relevance. The reason is the versatility to large samples, nearly all materials, and the high deposition rate [85]. The most important

advantage that even insulators and materials with high melting points, that can not be evaporated in a resistance evaporator, are evaporated by sputtering. The reason is that it uses ion bombardment in order to eject atoms or even clusters out of the target. An incoming ion starts an atomic displacement cascade leading to the ejection of a surface atom. This mechanism is shown in Figure 4.2. The out-sputtered particles are then deposited on a substrate.

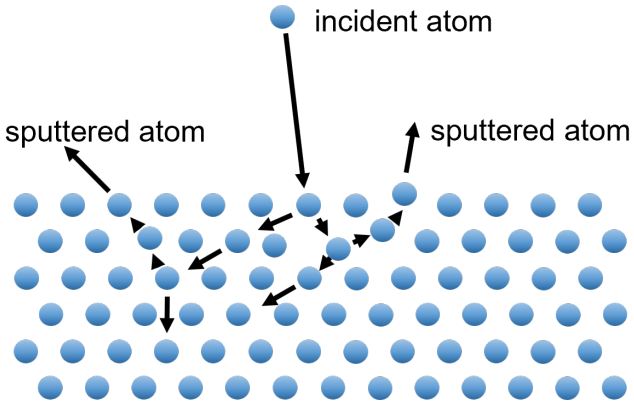

Figure 4.2.: Sputtering mechanism of target material by incident atom. An incident atom starts an atomic displacement cascade which results in sputtering of surface layers.

Sputtering was first described by Grove in 1852 and Plücker in 1858 as 'spluttering' or 'cathode disintegration'. However, it took more than a century for the first commercially available sputtering coating system by Leybold and a wider demand for this technology by semiconductors in the 1970s and optical recording media in the 1980s. The simplest sputtering variant is diode sputtering. Here, an electric potential between target and substrate is applied. By this potential, the sputtering gas (e.g. Argon) is accelerated onto the target material. The ratio between incident particle and ejected particle is called sputter yield Y. The sputtering yield is strongly dependent on the incident ion energy. As an example, the sputter yield of argon bombarded Nb at $100\,\mathrm{eV}$ is 1 [86]. Equation 4.8 gives the final erosion rate

$$R = 62.3\frac{JYM_\mathrm{a}}{\rho}\text{Å/min} \tag{4.8}$$

with the ion current density J of the gas in $\mathrm{mA/cm^2}$, M_a the atomic weight of the target atoms, and ρ the density of the target [86]. The ejected target species then travel to the substrate were they are deposited. The erosion rate can be manipulated by the process gas pressure. In addition, the process pressure also manipulates the mean free path of the out-sputtered species and the kinetic energy at the substrate surface. Lower pressures lead to a higher mean free path and kinetic energies. However, the lower pressures also lead to lower ion current densities since it is less likely to have ionizing collisions. Unfortunately, the minimum pressure necessary for plasma discharge limits the kinetic energy in diode sputtering. In the 1970s, a new magnetically enhanced variant emerged which was called magnetron sputtering [85]. In this variant, electrons with a velocity $\vec{v}$ are forced on cycloidal orbits in a magnetic field $\vec{B}$ by Lorentz force

$$\vec{F}_\mathrm{L} = q\vec{v} \times \vec{B} \tag{4.9}$$

in the absence of an electrical Field $\vec{E}$. The magnetic field traps the electrons in cycloidal tracks in the vicinity of the target surface. Although the collision probability is increased leading to higher ion densities with

high sputtering rates, relatively high kinetic energies at low pressure are also possible. In sum, magnetron sputtering allows more optimization potential to the respective demands. However, magnetron sputtering guns are technically more advanced. Another disadvantage is that the cycloidal track of the electrons result in preferred erosion of the target in this region. This way, only a low volume fraction of the target material can be used until the race track depth reaches the track thickness. There are two operation modes, direct current (DC) and radio frequency (RF) magnetron sputtering. While DC magnetron sputtering is the preferred mode for most metals, it is not possible to sputter insulators due to charging of the target. One possibility is doping to increase the conductibility. Since this is often not possible, the commonly used mode for this group of materials is RF sputtering at a frequency of $13.56\,\mathrm{MHz}$. In this work, DC magnetron sputtering of niobium and RF magnetron sputtering of tin are operated simultaneously. This variant is the so-called co-sputtering. Although it is technically not necessary to use RF magnetron sputtering for the metal tin, the sputtering rate is shown to be more stable and the erosion more homogeneous.

Figure 4.3 shows the sputtering coating system used in this work. It consists of a Thermionics vacuum chamber with loadlock chamber. A Leybold turbomolecular pump together with a roughing pump reach base pressures around $1.0 \times 10^{-6}\,\mathrm{mbar}$. Three Lesker Torus 2C sputtering guns are installed using the bottom flanges. DC and RF power sources are used to control the sputtering power of the niobium and tin targets, respectively. The sputtering guns are shielded by custom made separators avoiding cross-contamination. Mechanical shutters at the sputtering guns allow operation of the guns without coating of the substrate. Four MKS mass flow controllers can be used to control four gases independently or mix gases in the desired ratio. A MKS automatic valve is used to control the process pressure during sputtering. The custom made sample manipulator can be used to adjust target-sample distance and allows sample rotation for homogeneous coating of large sample up to $77\,\mathrm{mm}$ diameter. The temperature is measured by a type K thermocouple which is positioned between sample and heating lamps. An Eurotherm controller is used to track and control the temperature during the deposition process. The sample can be heated up to about $520\,^{\circ}\mathrm{C}$ by two $24\,\mathrm{V}/10\,\mathrm{A}$ projection lamps. For this sample temperature, the substrate manipulator needs to be heated to about $800\,^{\circ}\mathrm{C}$.

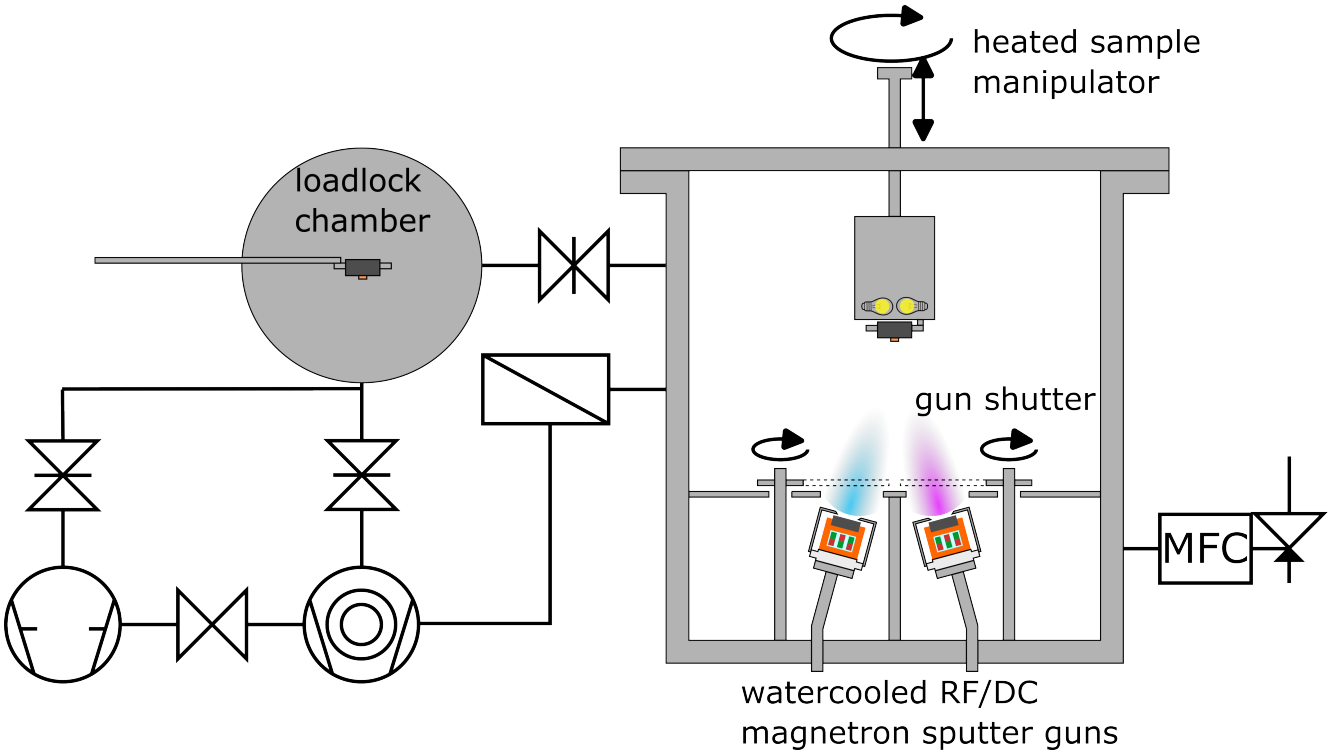

Figure 4.3.: Schematic of the deposition system used in this work equipped with three water-cooled sputtering sources. While a mass flow controller (MFC) was used to control the argon inlet, a butterfly valve controlled the pressure in the chamber. Lamps are used to heat the sample from the backside to the desired process temperature.

In this work, process pressures of about 8.0×10^{-3} mbar to 1.0×10^{-2} mbar and an argon flow of 0.058 standard cubic cm per minute were used. The guns were started with closed shutters to allow process stabilization until the substrate reached the desired process temperature. A heating rate of $30\,\mathrm{K\,min^{-1}}$ was used to heat to $50\,\mathrm{K}$ below the process temperature. From this point, a heating rate of $5\,\mathrm{K\,min^{-1}}$ was used to avoid overshooting of the temperature. When the temperature was reached, the shutters were opened and the deposition started. After the deposition time, the shutters were closed and the guns stopped. The temperature was hold at the process temperature for another $30\,\mathrm{min}$ and then cooled down in $25\,\mathrm{min}$.

4.3. x-ray diffraction

Back in 1913, W.L. Bragg and W.H. Bragg discovered that characteristic patterns were projected by crystalline samples when illuminated by x-rays [87]. Today, x-ray diffraction is the most important characterization method in materials science. It is used mainly for phase determination of samples, however, it can be used for many other purposes. Depending on the measurement procedure, material properties like lattice constant, strain, crystallite size, density, texture, and surface roughness can be determined. The principle of this technique is the interference of x-ray photons reflected at atomic planes in crystals. These photons need wavelengths of the incident radiation in the range of the observed features. In materials science, typical wavelengths used are typically $1\,\text{Å}$ to $100\,\text{Å}$ (x-ray) which corresponds to the atomic distance in crystals. The Bragg equation formulates a relation between diffraction angle θ, the distance between lattice planes d to the wavelength λ with

$$n\lambda = 2d \sin\theta. \tag{4.10}$$

This equation followed the discovery in the same year[88]. The conclusion from the experiments was that a crystal is a periodical arrangement of atomic planes with constant distances parallel to each other. The principle of diffraction is illustrated in Fig. 4.4.

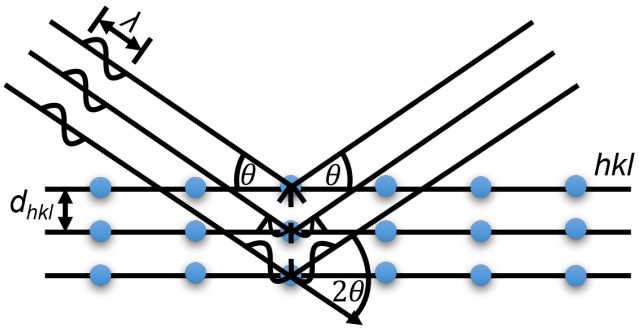

Figure 4.4.: Diffraction principle according to Bragg's law. Atomic planes act as mirrors for incoming x-ray radiation. Interference between outgoing photons leads to angular distribution of intensity that can be used to determine the atomic distance.

In this specific case a monochromatic beam is reflected by the atoms. As it is formulated in Bragg's law, the reflection occurs from the atomic planes. In dependence of the incident angle, the phase difference between reflected waves can be either constructive or destructive. In the constructive case, a peak in intensity is observed. The angular distribution of these peaks give information about the characteristic distance d of the crystal which can then be used to determine lattice constants (a, b c, α, β and γ) [89]. Equation 4.10 can also explain the wavelength requirement for diffraction. Inserting the maximum angle of $\theta = 180°$ in this equation, it follows

$$\lambda \leq 2d. \tag{4.11}$$

It can be concluded that the diffraction angles depend only on the lattice constants. Using this fact experimentally, the structure of samples can be determined, for example, using Cu-K_α radiation with a wavelength of $1.5406\,$Å.

Such a characteristic diffraction pattern does not only contain information by the position of the peaks, but also their relative intensity or even the absence of predicted peaks. The incident beam can be scattered elastically by Thomson scattering. Another process is called Compton scattering, where a weakly bonded electron is displaced by the x-ray photon. This deflects the beam and increases its wavelength. The scattering by an atom in a solid can be seen as the Thomson scattering of all electrons in sum. Since electrons have different positions around the atomic core, the summation is dependent from the incident angle. Due to characteristic electron distribution for different elements, the description of the scattering needs the introduction of the atomic scattering factor

$$f = \frac{A_a}{A_e} \tag{4.12}$$

with the amplitude of the x-ray scattered by an atom A_a and the amplitude of the x-ray scattered by the electron A_e. The atomic scattering factor equals the number of electrons in the given atom (which equals the atomic number Z for uncharged atoms) in case that the diffraction angle is $\theta = 0°$. In this scenario, the electron scattered x-rays are all in phase and interfere constructively. Higher diffraction angles result in smaller values. The atomic scattering factor considers only diffraction by one atom. Therefore, the scattering and phase of every atom in a unit cell needs to be considered which results in the amplitude-phase product for a single atom in the unit cell

$$Ae^{i\phi} = fe^{2\pi i(hu+kv+lw)} \tag{4.13}$$

with the intensity of the scattered wave A, its phase ϕ, the Miller indices h, k and l, together with the fractional coordinates $u = x/a$, $v = x/b$ and $w = z/c$. These amplitude-phase products then need to be summed up for n atoms in the unit cell as follows

$$\sum_n f_\mathrm{n} e^{2\pi i(hu_\mathrm{n}+kv_\mathrm{n}+lw_\mathrm{n})} = F_\mathrm{hkl} \tag{4.14}$$

with the complex number F containing both phase and amplitude information of diffracted x-ray for the unit cell. Experimentally, only $|F|^2$ can be determined by an x-ray detector. It is only possible to determine F_hkl by the calculation of the wave information. This is the so-called phase problem. Another experimental method uses highly coherent radiation (e.g. from a synchrotron) where the phase information is preserved until the photons are diffracted to determine F_hkl [89, 90].

4.3.1. Diffractometer configuration

A SmartLab thin film diffractometer from Rigaku was used for structural characterization of the samples synthesized in this work. The installed x-ray source was a 9kw Cu rotating anode with a tungsten filament to generate x-rays with K_α of $1.5406\,$Å. For the x-ray generation, the source was set to $45\,$kV and $190\,$mA. A cross-beam-optics (CBO) unit with inserted parallel beam (PB) slit together with a Soller slit unit with $5°$ slits was installed on the source arm. Another slit limited the beam size on the sample stage to $5\,$mm. On the detector arm, there were installed two slit boxes set to $0.8\,$mm and $1.3\,$mm. $\theta/2\theta$-measurements were carried out utilizing a D/TeX line detector in 1D-mode together with a K_β filter while grazing incidence measurements were carried out using a SC90 point detector together with a graphite analyzer. After the parallel optics alignment procedure, the sample was aligned with the beam half cut procedure.

4.3.2. $\theta/2\theta$-scans and pole figure scans

$\theta/2\theta$-scans are the standard measurements procedure to determine the crystal structure of thin film samples. The set-up for this measurement is shown in Fig. 4.5. For this measurement, the parallel beam configuration is used. While the sample stage does not move, both, the x-ray source and the detector move symmetrically by θ.

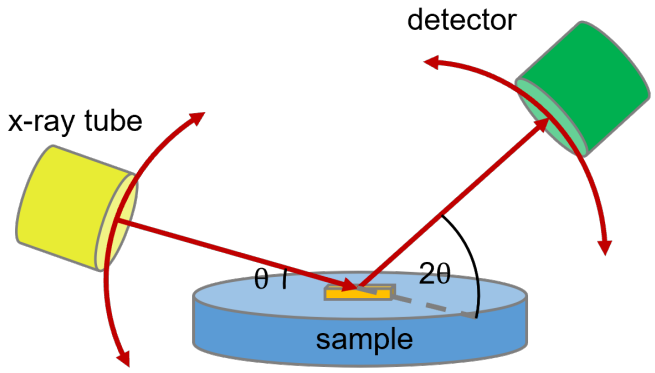

Figure 4.5.: Experimental procedure of $\theta/2\theta$-Scan. While the sample is fixed on a stationary manipulator, the x-ray source and the detector move simultaneously with θ.

Pole figures provide texture information of the measured sample by a stereographic projection. Experimentally, it is measured by repetitive $\theta/2\theta$-scans. In between the $\theta/2\theta$-scans, the sample stage is tilted along the χ-axis by a defined step up to $90°$ and fully rotated around the ϕ-axis.

4.3.3. 2θ-scans

XRD measurements of thin film samples are challenging in terms of intensity. There are several reasons for low intensities. Among others, low film thicknesses result in very high substrate reflection intensity. To overcome this limitation, it is possible to use 2θ-scans. Figure 4.6 shows this measurement procedure schematically. Here, the x-ray source arm stays at a pre-defined angle, while the detector arm moves by 2θ. This way, the incident beam path through the thin film is longer and the diffraction signal is higher. Another advantage of this measurement type is that it can be used for depth profiling. The measurement can be performed for difference incidence angles. If the phase fraction of these measurements differs, a rough estimation about the phase depth distribution can be stated. 2θ-scans are used for the Williamson-Hall plot, since it provides information about the in-plane grain size. In contrast to the 2θ-scans, the $\theta/2\theta$-scans provide a well averaged value of in-plane and out-of-plane grain sizes.

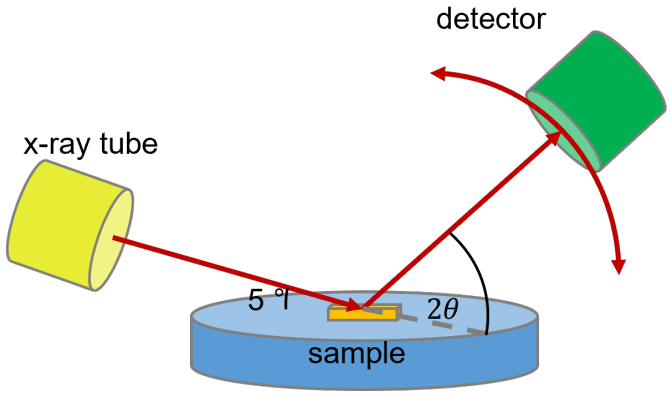

Figure 4.6.: Experimental procedure of 2θ-scan (grazing incidence x-ray diffraction). While the sample is fixed to a stationary manipulator and the x-ray source is fixed to a small grazing incidence angle, the detector moves with 2θ.

4.3.4. Williamson-Hall plot

XRD can be further used to determine an averaged grain size of polycrystalline thin films. For such materials, the reflections are not as sharp as for single crystals. The origin of this broadening are the three mechanisms grain size broadening, strain broadening and instrument broadening. The Scherrer equation with

$$\beta_{\mathrm{L}} = \frac{K\lambda}{L\cos\theta} \tag{4.15}$$

allows to calculate the grain size L using the full width at half maximum (FWHM) as β_{L} at the given diffraction angle θ. In this scenario, K is a geometry factor which is normally assumed to be 1. However, the different origins of peak broadening are not considered.

The Williamson-Hall plot is a graphical approach to distinguish between grain size broadening and strain broadening based on the Scherrer equation. However, it can not be used to distinguish between instrument broadening and broadening by the crystals. Therefore, two procedures are possible. Either the instrument broadening needs to be determined experimentally or the instrument broadening needs to be neglected. In case the instrument broadening is neglected, it is not possible to give an absolute value for grain size and strain in the sample. This way, it can be used for a relative comparison to other samples which is done in the present work. Williamson and Hall proposed an extension for the differentiation between grain size broadening β_{L} and strain broadening β_ϵ of the reflection at diffraction angle θ. The strain C_ϵ of the sample can be calculated by equation 4.16 with

$$\beta_\epsilon = C_\epsilon \tan\theta. \tag{4.16}$$

This equation is added to the Scherrer equation. In equation 4.17, the total FWHM of the reflection is

$$\beta_{\mathrm{tot}} = \beta_{\mathrm{L}} + \beta_\epsilon = C_\epsilon \tan\theta + \frac{K\lambda}{L\cos\theta}. \tag{4.17}$$

Using equation 4.17, grain sizes can be calculated for known strains and vice versa. However, it is not possible to calculate strain and grain size independently. Therefore, Williamson and Hall made use of the angular dependence of grain size broadening and strain broadening. It is known that grain size has a stronger impact on low angle reflections and strain has a stronger impact on high angle reflections. Equation 4.18 is a linear function which leads to the Williamson-Hall plot. The linear equation of this plot is given by

$$\frac{\beta_{\mathrm{tot}}\cos\theta}{\lambda} = \frac{C_\epsilon \sin\theta}{\lambda} + \frac{K}{L}. \tag{4.18}$$

In this plot, every reflection with FWHM (β_{tot}) at diffraction angle θ of the pattern is represented by a single point. The y-axis intersection of this plot $\frac{\lambda K}{L}$ then can be used to determine the grain size. Consequently, the slope of the linear function $\frac{C_\epsilon \sin\theta}{\lambda}$ can be used to calculate the strain.

4.4. Scanning electron microscope and energy dispersive x-ray spectroscopy

Modern scanning electron microscopes (SEM) provide resolutions below 1 nm [91]. SEMs reach resolutions much lower than common light microscopes. The reason is that SEMs use electron beams. The attributed wavelength of the electron beams is lower than that of visible light. The used electron sources are W (or LaB_6) cathodes or field emission guns which are defined by their electron energy E_B and their electron current I_B. The electron energy affects the penetration depth R into the sample and the beam current influences the intensity of the secondary beam. Lenses (electric coils) are used to focus the primary electron beam. They are illustrated in Fig. 4.9. Another set of scan-coils is used to deflect the beam for scanning purposes. Usually, three different detectors are used for different applications. The secondary electron (SE) and backscattered electron (BSE) detectors are used for topographical imaging, while the x-ray detector is for energy dispersive x-ray spectroscopy (EDX). Per definition, secondary electrons have less than 50 eV and backscattered electrons have more than 50 eV. The BSE detector is used for better resolution in z-direction, while the SE detector is used for better resolution in xy-direction. Secondary electrons are accelerated into a positively charged collector grid. After passing the grid, the electrons are counted by a scintillation counter. Such a detector is called Everhart-Thornley detector. The detector is positioned sideways that deeper regions propagate electrons in the higher regions. This is how the topographical information is created.

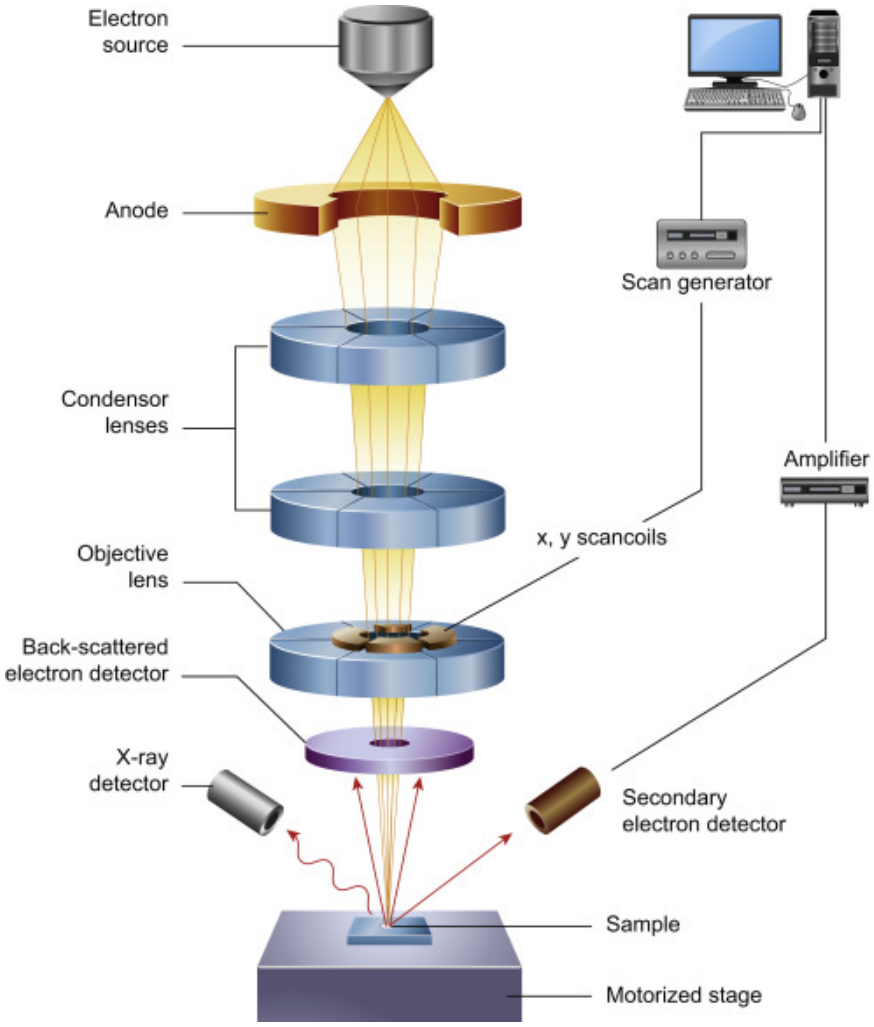

Figure 4.7.: Basic functionality of the scanning electron microscope [92]. An electron beam is focused to a small spot by lenses. Scan-coils are used to deflect the beam to scan the sample surface. Secondary electron detector and back-scattered electron detector are used for topographical imaging. An x-ray detector is used for elemental analysis.

Fig. 4.8 shows the electron-sample interaction. The mean free path limits the information depth of the species. In comparison, the x-ray information depth is about $2\,\mu m$ [93]. It must be noted that the excited area is larger than the incident beam size. This limits the ability of local resolved analysis with x-rays.

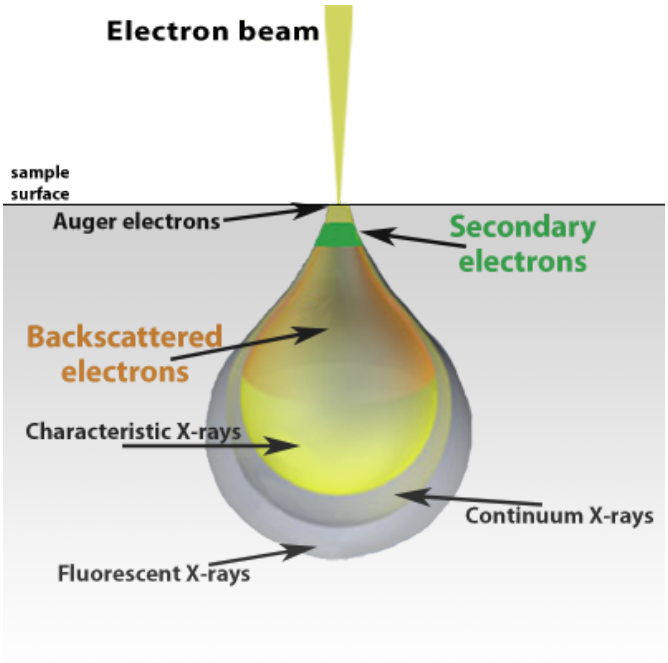

Figure 4.8.: Electron-sample interaction in scanning electron microscopy (SEM) [94]. The information depth of the imaging depends on the detected species.

However, the x-rays can be used for elemental analysis. The basic principle of energy dispersive x-ray spectroscopy (EDX) is shown in Fig. 4.9. Here, the primary electron kicks-out a second electron. Then another electron from a higher shell falls down occupying the vacancy. This transmits a photon of characteristic wavelength.

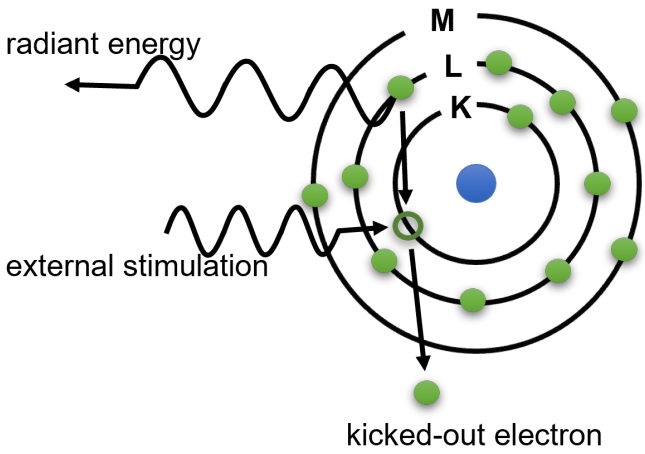

Figure 4.9.: Basic principle of energy dispersive x-ray spectroscopy (EDX). An electron is kicked-out by external stimulation. Another electron occupies the vacancy and emits an x-ray photon of characteristic wavelength.

For quantitative analysis of a sample, it is assumed that the number of x-ray photons at a certain wavelength is proportional to the weight percent of the element in the present sample. The sample is then compared

to a known standard. The relation

$$\frac{c_\mathrm{i}}{c_\mathrm{i}^{STD}} \approx \frac{I_\mathrm{i}}{I_\mathrm{i}^{STD}} = k_\mathrm{i} \tag{4.19}$$

with intensity I of element i leads to concentration c of element i making use of the known intensity and concentration of known standard. Several instrumental factors as must be corrected as well as the difference in electron backscatter, density, x-ray excitation cross section, energy loss, and absorption within the solid. These effects are divided into the origins atomic number Z_i, x-ray absorption A_i, and x-ray fluorescence F_i. The corrected quantification follows as

$$\text{wt\%} = \frac{c_\mathrm{i}}{c_\mathrm{i}^{STD}} \cdot 100 = \frac{I_\mathrm{i}}{I_\mathrm{i}^{STD}} \cdot \frac{100}{[Z.A.F]_\mathrm{i}} = k_\mathrm{i} \frac{100}{[ZAF]_\mathrm{i}} \tag{4.20}$$

The EDAX Genesis software used in this work allows for a true standardless correction considering all aspects of x-ray generation, propagation through the solid target and detection. The relation

$$\text{wt\%} = k_\mathrm{i} \frac{100}{[ZAF]_\mathrm{i}} \cdot SEC \tag{4.21}$$

allows then to give the corrected elemental composition of the sample. In this work, a Philips XL30-FEG equipped with a Genesis detector from EDAX was used. The measurement time was set to $300\,\mathrm{s}$ at $15\,\mathrm{kV}$ acceleration voltage.

4.5. Photoelectron spectroscopy

Photoelectron spectroscopy (PES) is a characterization method to obtain information about the density of states, oxidation state and chemical composition of materials. PES is based on the photoelectric effect to eject electrons from a given sample using photons. There are typically two different photons sources used, the x-ray sources and ultraviolet light sources. The technique is then named x-ray photoelectron spectroscopy (XPS) or ultraviolet photoelectron spectroscopy (UPS). Since the mean free path of the ejected electrons is limited to several nanometers, this characterization method is highly surface sensitive. The kinetic energy of the emitted electron is measured and the following relation

$$E_\mathrm{kin} = h\nu - E_\mathrm{B} - \phi_\mathrm{S} \tag{4.22}$$

with the energy of the incident photon $h\nu$, the binding energy of the electron E_B and the work function of the spectrometer ϕ_S is used to determine the binding energy of the emitted electron. This basic principle is shown in Fig. 4.10.

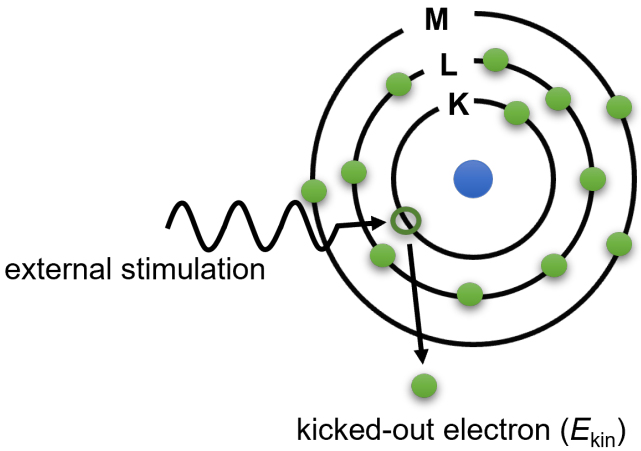

Figure 4.10.: Basic principle of x-ray photoelectron spectroscopy (XPS). An electron is kicked-out by external stimulation. The kinetic energy of the kicked-out electron is determined by an analyzer.

The sample is electrically connected to the spectrometer which brings the different Fermi levels of sample and spectrometer into line. The binding energy of the electron is usually given with respect to the Fermi level. For this reason, E_B is independent from the work function of the sample ϕ_P. The band structure of a sample electrically connected to the spectrometer is depicted in Fig. 4.11 (left).

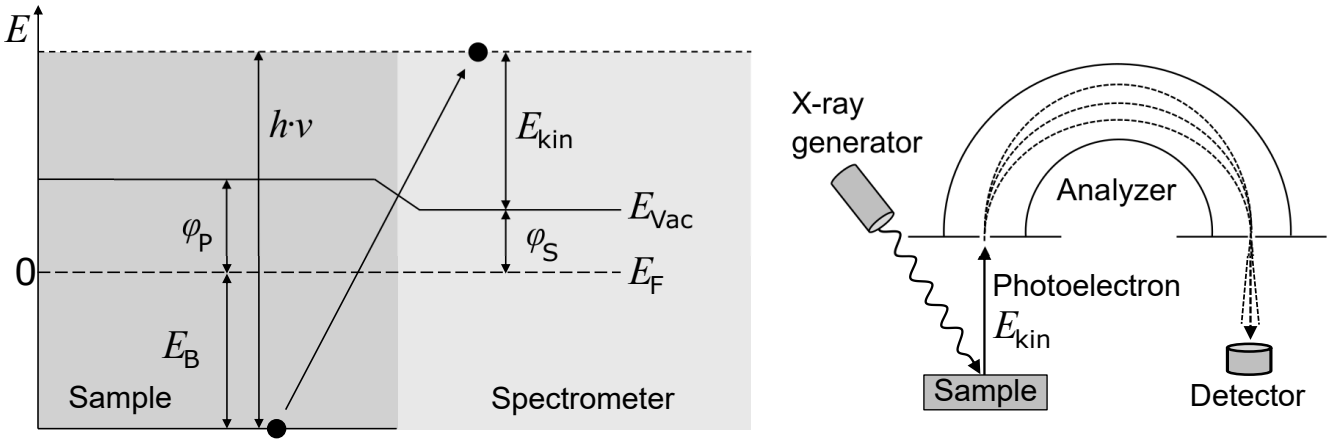

Figure 4.11.: Electronic band structure of a sample in a photoelectron spectrometer (left) and schematic setup of an photoelectron spectrometer (right) from Bayer [95].

Fig. 4.11 (right) shows a schematic setup of a photoelectron spectrometer. The photons are generated in an x-ray source, monochromatized and focused before hitting the sample. The ejected electrons then pass an analyzer before hitting the detector. The analyzer deflects the electrons by a defined potential difference between two concentric hemispheres. This means that only electrons of a certain kinetic energy can pass the analyzer to be counted in the detector. The whole spectrum of kinetic energies is analyzed by a sweep of the potential between the two hemispheres.

The background (after Tougaard [96]) of the spectrum is subtracted in this work using the relation

$$T(E) = \int_E^\infty F(E' - E)S(E')dE'. \tag{4.23}$$

The Tougaard algorithm convolutes the energy cross section $F(E)$ and the measured spectrum $S(E)$. The energy loss cross section is the probability of an electron at an energy E to contribute to the background. The universal cross section used in the program CasaXPS is given by

$$F(E) = \frac{B \cdot E}{(C + E^2)^2} \tag{4.24}$$

with a parameter B to match the background with the data points at the region limits. After the background subtraction, the raw area of all peaks of the spectrum is determined. Each area I_x is divided by an element specific relative sensitivity factor RSF_x. The chemical composition is then calculated by the relation

$$c_\mathrm{x} = \frac{I_\mathrm{x}/RSF_\mathrm{x}}{\sum_\mathrm{i} I_\mathrm{i}/RSF_\mathrm{i}}. \tag{4.25}$$

The XPS measurement of this thesis were conducted a the DAISY-BAT (Darmstadt's integrated system for battery research) photoelectron spectrometer which is PHI Versaprobe 5000. The used photons were AlK_α ($h\nu$=1486.6 eV). The detector was at $75°$ to the sample surface leading to an information depth of $\approx$5 nm to 8 nm.

4.6. Resistivity measurements

The 4-point probe method is a measuring technique to make more accurate resistance measurements than the 2-point probe method. It makes use of two separate pairs of current-carrying and voltage-sensing electrodes. Such a separation is essential when low resistances are expected. Four measurement points allow the extinction of the contact resistance between the probe and the surface of the sample, but also the resistance of the cables and the voltmeter. The method uses the fact that the contact and instrument resistances are constant for all measurements. Since different known distances (between outer and inner electrodes) are measured, the contact and instrument resistances cancel out. What follows is the sample resistance which is given by

$$R = \frac{\rho \cdot D}{d \cdot W} \tag{4.26}$$

with the distance between outer and inner electrode pair D, the sample width W, the thin films thickness d, and the thin film material resistivity ρ. The sheet resistance R_s is commonly used for thin films which follows with

$$R_\mathrm{s} = \frac{\rho}{d}. \tag{4.27}$$

Fig. 4.12 shows the used sample geometry in this work. After the deposition of Nb_3Sn by co-sputtering, four bar gold contacts of 50 nm were sputtered to provide optimal contact to the Nb_3Sn thin film. The gold

contacts further ensure a constant width and distance between the electrode pairs.

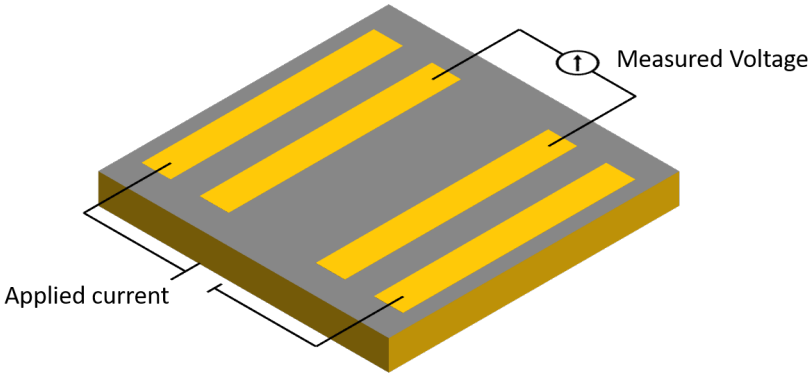

Figure 4.12.: Schematic of 4-point probe setup for resistivity measurements in the cryostat.

However, the samples measure in this work oxidized before the gold contact sputtering. For this reason, the measured resistances could not be used quantitatively. Thus, the resistances at $20\,\mathrm{K}$ (slightly above the critical temperature) were normalized to 1. Resistivity measurements were used to determine the critical temperature of the deposited superconducting films. For this determination, the resistivity utilizing the 4-point method was measured during cool down from $300\,\mathrm{K}$ to $5\,\mathrm{K}$ in a cryostat from Oxford instruments. The applied current was $10\,\mu\mathrm{A}$. Resistivity versus temperature measurements were used to determine $T_{\mathrm{c},90}$ which corresponds to the value of $90\,\%$ of the resistivity at $20\,\mathrm{K}$.

4.7. Magnetic measurements

4.7.1. The SQUID

SQUID stands for superconducting quantum interference device which is a widely used application of the Josephson effect. Such SQUIDs consist of a superconducting ring with a Josephson junction to exploit the flux quantization and can measure magnetic fields down to $10^{-15}\,\mathrm{T}$ (in multiples of the flux quantum). There are two types of SQUIDs, the DC and RF SQUID which are operated with an external DC and RF current in the superconducting ring, respectively. The difference is that the superconducting ring has one Josephson junction in RF and two Josephson junction in DC operation. Then, for every penetrated flux quantum, an oscillation of the voltage is observed. The amount of oscillations can be used to determine ΔB_{a} of the present field. Figure 4.7.1 show schematically how the voltage is picked up from the SQUID ring.

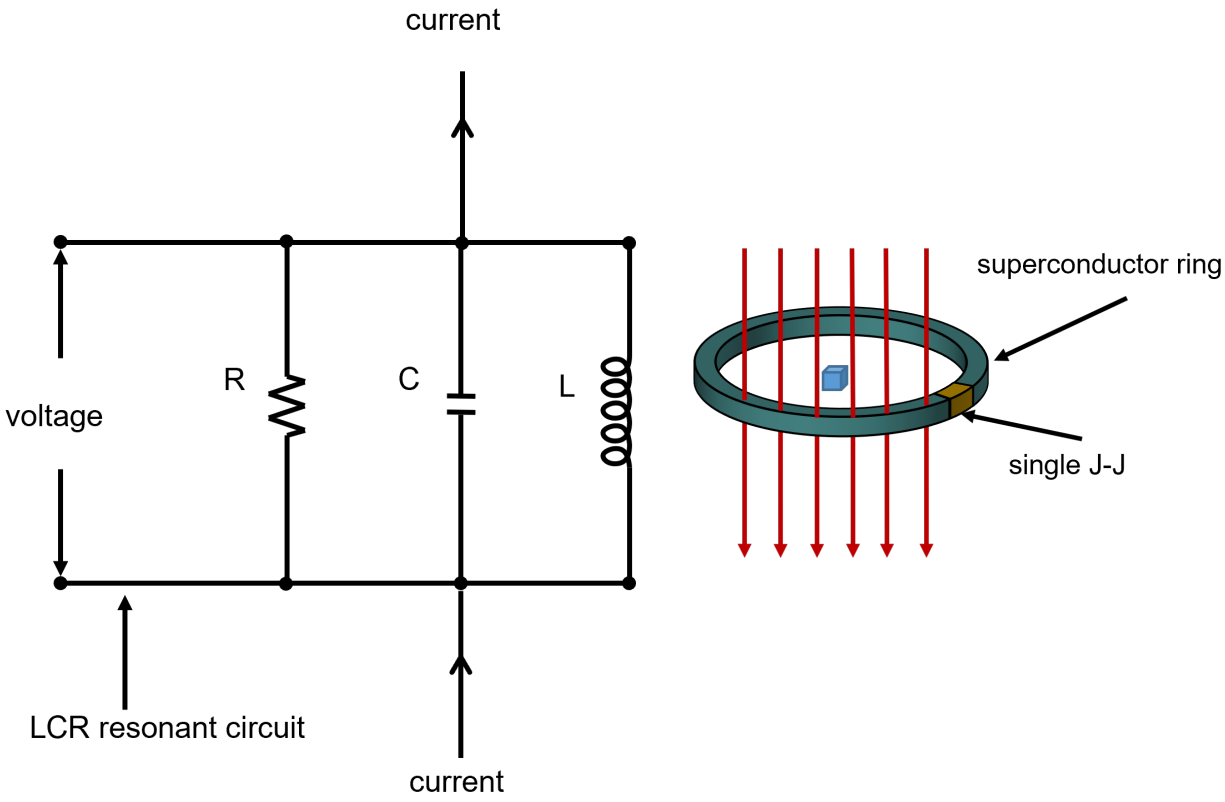

Figure 4.13.: Schematic of alternating current superconducting quantum interference device (AC-SQUID). The sample is positioned within a superconducting ring that has a built-in Josephson-junction (J-J). The magnetic moment of the sample is measured by moving the sample passing the superconducting ring twice. The pickup coil perceives voltage oscillations which then lead to the magnetic moment of the sample by a multiplication with the flux quantum.

The system used in this work was a Quantum Design MPMS. It consists of a strong superconducting magnet which is able to apply homogeneous fields up to $6\,\mathrm{T}$ within the SQUID ring. Next to the SQUID ring, the pick up coil is placed to pick up the changes in the supercurrent. To measure the magnetic moment of the sample, the sample is moved up (or down) to pass the SQUID ring twice. The amount of perceived voltage oscillations multiplied by the flux quantum then leads to the magnetic moment of the sample. In this work, the samples amplitude was $1\,\mathrm{cm}$ with a frequency of $2\,\mathrm{Hz}$. The used value of the magnetic moment was the average of the upwards and downwards movement. The MPMS was used for magnetization versus temperature $M-T$ and magnetization versus field $M-H$ measurements. These measurements were used to determine the critical temperature $T_{\mathrm{c},0}$ (the point of zero resistivity), but also the critical field $H_{\mathrm{c}1}$. $M-T$ measurements were carried out from $5\,\mathrm{K}$ to $20\,\mathrm{K}$ at $20\,\mathrm{mT}$ (zero field cooled) and $20\,\mathrm{K}$ to $5\,\mathrm{K}$ at $20\,\mathrm{mT}$ (field cooled). The first measurement point which is below the extrapolation of the paramagnetic value is used as $T_{\mathrm{c},0}$. For the determination of $H_{\mathrm{c}1}$, the lowest magnetic moment in virgin curves is used. The critical current density is determined using the relation

$$j_{\mathrm{c}} = 30\frac{\Delta M}{d} \tag{4.28}$$

with the difference in magnetization between the upwards and downwards sweep of a $M-H$ measurement at a given external magnetic field ΔM in emu/cm^3, and the width of the sample in which the shielding currents percolate d.

5. Results

The main goal of this work is the optimization of the superconducting Nb_3Sn films. The experiments of this work are structured as follows:

1. The process engineering on fused silica substrates optimizing the growth parameters (sputtering power ratio, substrate temperature, and integrated sputtering power).
2. The after-deposition annealing on sapphire substrate optimizing the parameters annealing temperature and duration for samples deposited at different temperatures.
3. The role of the kinetic energy of out-sputtered atoms on physical properties at low process temperature on fused silica substrates.
4. Investigations of the inter-diffusion, adhesion and surface roughness of films coated on copper substrates, and the role of the thin film thickness on the physical properties.

5.1. Process optimization on fused silica

5.1.1. Sputtering power ratio

Since the sputtering rate is proportional to the sputtering power [97], the sputtering power ratio can be used to tailor the stoichiometry of the Nb_3Sn thin films to reach the desired range of $24\,\%$ to $26\,\%$ for a good performance. Figure 5.1 shows the atomic tin content as a function of the sputtering power ratio in the range of 5.0 to 6.5 P_{Nb}/P_{Sn}. The deposition of this series has been carried out at room temperature to minimize the influence of thermal energy followed by an elemental evaluation by EDX. As it can be seen, the tin content can be accessed in a broad range.

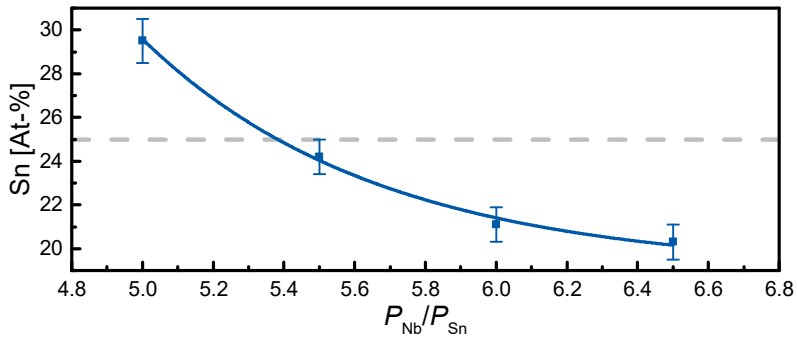

Figure 5.1.: Tin content measured by EDX plotted as a function of sputtering power input ratio of niobium and tin gun. The stoichiometric tin content in Nb_3Sn of $25\,\%$ is marked by the dashed gray line. The stoichiometry has been tuned in a broad range around the desired $24\,\%$ to $26\,\%$.

Since the best performance has been correlated to the tin content of $25\,\%$ [24], the optimal sputtering power ratio is considered to be 5.25.

5.1.2. Effect of substrate temperature

The effect of the substrate temperature on the thin film composition is investigated by using an optimal sputtering power ratio of 5.25 at increasing substrate temperature during thin film growth. The result of this series is shown in Fig. 5.2, that shows the tin content is constant within the desired window of $24\,\%$ to $26\,\%$ in the range of $260\,^{\circ}\mathrm{C}$ to $435\,^{\circ}\mathrm{C}$ and therefore, the thin film composition is considered temperature independent in this range. The most important conclusion is that the co-sputtering process does not suffer tin loss like it is reported for other processes [98, 99].

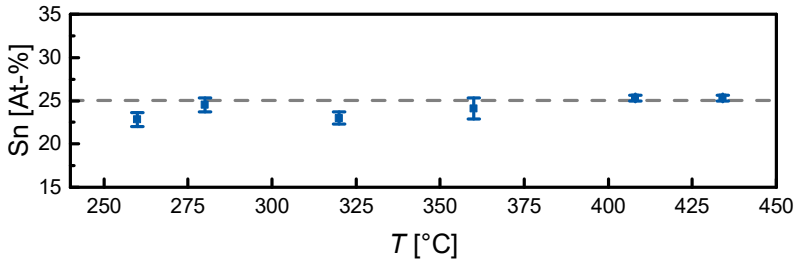

Figure 5.2.: Tin content measured by EDX is plotted as a function of substrate temperature at fixed power ratio of 5.25. The stoichiometric tin content in Nb_3Sn of $25\,\%$ is marked by the dashed gray line. The desired range was successfully accessed at every temperature.

XRD is used to get information about the phase growth as a function of the substrate temperature during thin film growth. The XRD patterns are shown in Fig. 5.3 and summarized in Tab. 5.1 for samples grown in the range from $260\,^{\circ}\mathrm{C}$ to $435\,^{\circ}\mathrm{C}$. All detected reflections of the shown patterns can be attributed to the Nb_3Sn phase with space group $Pm\bar{3}n$. Other reflections were not observed indicating films with high phase purity. The reflection with the highest peak area at $2\theta = 34.11^{\circ}$, 38.28° and 42.10° can be correlated to the Nb_3Sn 200, 210, and 211 reflections, respectively.

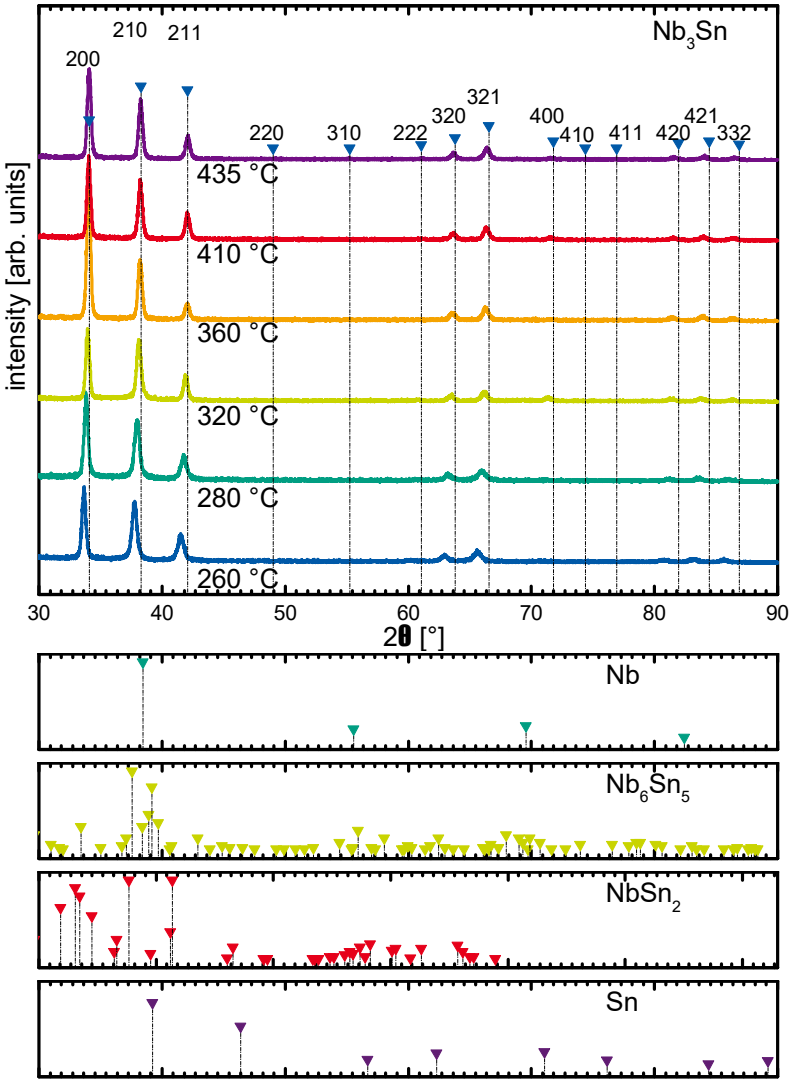

Figure 5.3.: XRD patterns of Nb_3Sn thin films grown on fused silica substrates. The substrate temperature is decreased from $435\,°C$ to $260\,°C$ while the power input is fixed to $20\,W$ Sn/$105\,W$ Nb (power ratio of 5.25). Nb_3Sn reflections are marked in the tip down triangles. For comparison, patterns of Nb, Sn, Nb_6Sn_5, and $NbSn_2$ are given. All detected reflections were correlated to Nb_3Sn ($Pm\bar{3}n$) indicating a high phase purity. 210, 211, and 200 reflections indicate a textured growth in the (100) orientation.

However, the peak area ratio of the 200, 210 and 211 reflections is uncommon (in comparison to powder), that indicates a texture along the (100) orientation. Pole figure measurements in Fig. A.1 and A.2 confirmed the texture. A comparison of the peak position shows a continuous shift to higher angles with increasing process temperature that indicates a decreasing lattice constant of the Nb_3Sn phase. Increasing the process temperature is further observed to result in smaller FWHM of the 210 reflection. This is an indication for a larger average of crystallite size at higher process temperatures that in general decreases the grain boundary density [100].

Table 5.1.: Sample overview of Nb_3Sn grown on fused silica by co-sputtering. The substrate temperature was decreased from $435\,°C$ to $260\,°C$ at a constant power ratio of 5.25 and $20\,W$ Sn/$105\,W$ Nb. The tin content and FWHM of the 210 reflection are listed.

T_{sub} [°C]	Sn [At-%]	FWHM 210 [°]	$T_{c,90}$ [K]
435	25.3±0.3	0.367	13.9
410	25.3±0.3	0.387	15.1
360	24.1±1.2	0.381	14.7
320	23.0±0.7	0.414	11.5
280	24.5±0.8	0.493	7.3
260	22.8±0.8	0.497	/

This work aims for a critical temperature as close as possible to the bulk value of $18.3\,K$ [17] at the lowest possible synthesis temperature. Besides Nb_3Sn, there are the intermetallic compounds Nb_6Sn_5 and $NbSn_2$ with transition temperatures below that of metallic Nb with $9.2\,K$ [101]. It is therefore unfavorable to have these insidious phases. Resistivity versus temperature measurements are shown in Fig. 5.4 and the properties summarized in Tab. 5.1.

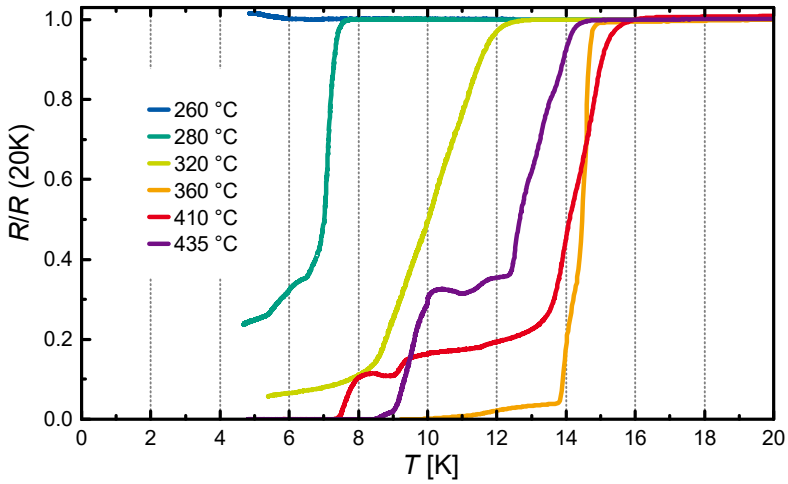

Figure 5.4.: Resistivity normalized to the resistivity at $20\,K$ of sputtered Nb_3Sn thin films versus temperature. The substrate temperature is decreased from $435\,°C$ to $260\,°C$ while the power input is fixed to $20\,W$ Sn/$105\,W$ Nb at a power ratio of 5.25. T_c is determined at $90\,\%$ of the resistivity at $20\,K$ and defined as $T_{c,90}$. Substrate temperatures above $280\,°C$ result in superconducting phases. With increasing substrate temperature the primary transition temperature increases.

It can be clearly seen that all samples have a transition into the superconducting state except for the sample deposited at $260\,°C$. All samples grown above $280\,°C$ demonstrated a transition temperature higher than $9\,K$ that validates the Nb_3Sn phase formation. For the first time, superconducting Nb_3Sn is synthesized at temperatures as low as $320\,°C$. Unfortunately, all samples of this series have a second transition. There are two possibilities, tin deficient Nb_3Sn regions with less than $25\,\%$ tin content [24] or thermally activated

phase slippage (TAPS) across weakly coupled regions [102]. Such a foot structure could be observed for grain boundaries [103]. Here, it is likely to form weak links across grain boundaries. At the same time, it is unlikely that only a few distinct tin concentrations form and result in such foot structures. An obvious solution is to increase the process temperature [32] that has been demonstrated for different processes. This in turn can cause tremendous tin loss. Since the goal of this work is to keep the process temperature low, other solutions are investigated.

5.1.3. Role of total sputtering power

To further improve the superconducting properties, morphology, and composition of the low-temperature co-sputtering process, a series of varying integrated sputtering power has been produced. Since the peak position of the sample grown at $435\,°C$ are closest to the bulk pattern, the following series has been grown at $435\,°C$. By increasing the sputtering power, the kinetic energy of out-sputtered species is increased. The higher kinetic energy brings additional energy to the system to promote surface diffusion at low temperature. For this series, the sputtering power ratio is kept constant at 5.25 while the total sputtering power is varied. The XRD patterns are shown in Fig. 5.5 and the determined characteristics are summarized in Tab. 5.2.

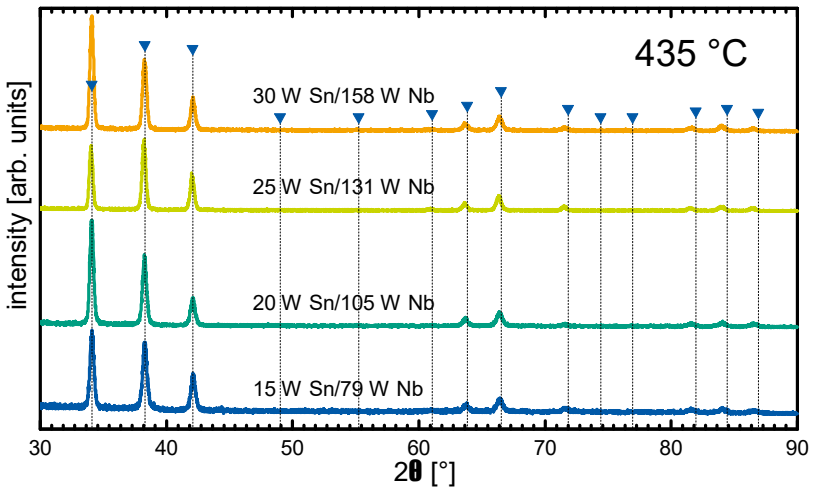

Figure 5.5.: XRD patterns of Nb_3Sn thin films grown on fused silica substrates. The sputtering power was increased from $15\,W$ Sn/$79\,W$ Nb to $30\,W$ Sn/$158\,W$ Nb while the substrate temperature was fixed to $435\,°C$ at a power ratio of 5.25. All detected reflections are correlated to the Nb_3Sn ($Pm\bar{3}n$) indicating a high phase purity.

The XRD patterns of this series show a preferentially textured growth along the (100) orientation only revealing reflections from the Nb_3Sn phase. For this series of varying sputtering power, the peak positions evidently do not change. The FWHM is, however, a function of the sputtering power. The FWHM increases for lower sputtering power indicating that higher sputtering power (and higher kinetic energy) promotes growth of larger grains. The results are validated by SEM investigation shown in Fig. 5.6.

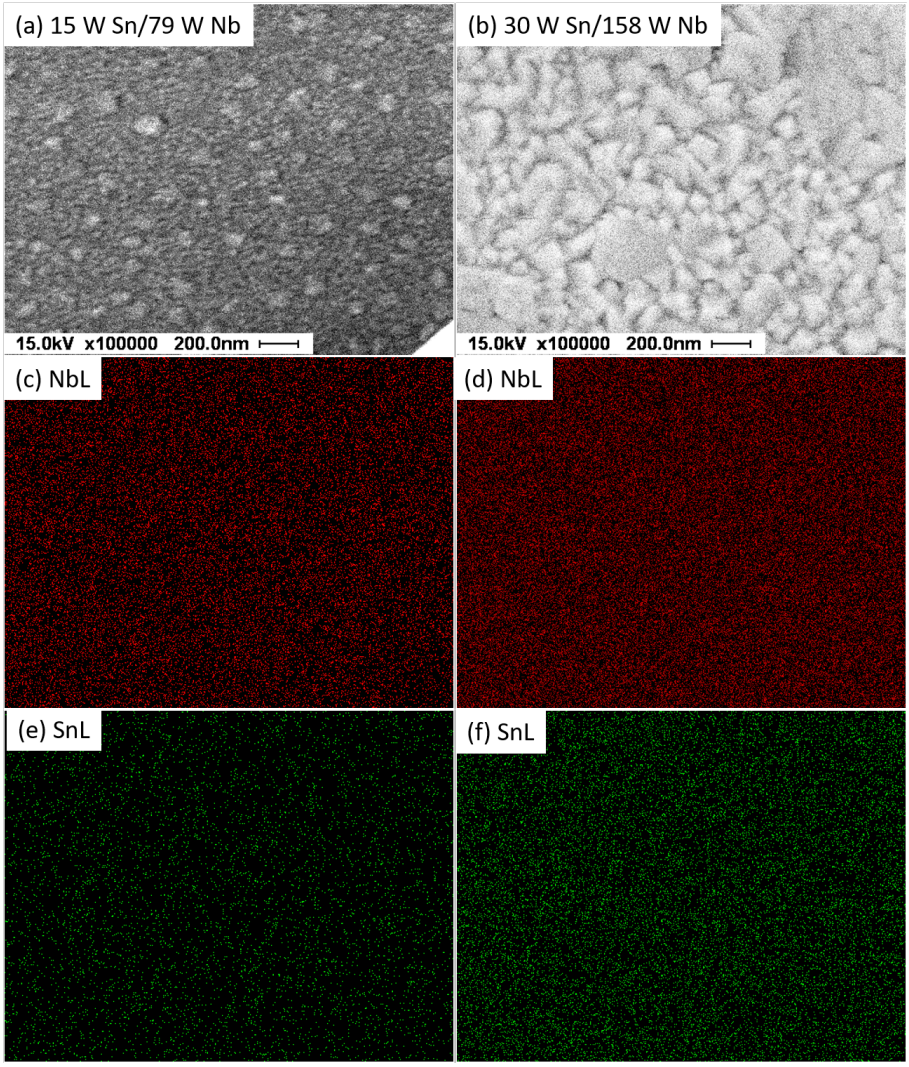

Figure 5.6.: Secondary electron images (top), NbL (middle) and SnL (bottom) emission of the same area by EDX of sputtered Nb_3Sn thin films at a fixed substrate temperature of $410\,°C$ and a power ratio of 5.25 while the power input is increased from $15\,W$ Sn/$79\,W$ Nb ((a),(c) and (e)) to $30\,W$ Sn/$158\,W$ Nb ((b),(d) and (f)).

It is clear from the SEM images that the sample sputtered at $30\,W$ Sn/$158\,W$ Nb has larger grains than the sample sputtered at $15\,W$ Sn/$79\,W$ Nb. This observation is in agreement with the FHWM of the XRD patterns. EDX mapping is carried out additionally to obtain information about the local homogeneity. From these images, no elemental segregation is visible. Combining both techniques, XRD and EDX mappings, it can be stated that the films have an excellent homogeneity. It must be noted that the film sputtered at higher sputtering power has also higher film thicknesses. The film thickness can have an impact on the grain size. In this series however, the film thickness is one order of magnitude larger than the grain size. For this reason, the grain size is considered to be independent from the film thickness (see Tab. A.2).

To show the influence of the sputtering power to the superconducting properties, $R-T$ measurements were performed and plotted in Fig. 5.7. All samples have a critical temperature above $9.2\,K$ that is a clear indication for the formation of Nb_3Sn. It can be seen from the resistivity versus temperature measurements

that the increase of the sputtering power results in an increase of the critical temperature from $13.8\,\mathrm{K}$ to $16.3\,\mathrm{K}$. An evenly important observation is that the foot structure is less pronounced with increasing sputtering power until the samples sputtered at $30\,\mathrm{W}$ Sn/$158\,\mathrm{W}$ Nb have a sharp transition. It is plausible that the TAPS foot structure vanishes for higher sputtering powers, since the higher sputtering powers lead to larger grains (less grain boundaries). The $I(V)$ characteristics and calculated kinetic energy statistics values (from numerical simulations) are summarized in Tab. A.3 and Tab. A.4. In conclusion, the increased overall sputtering power is beneficial for the phase formation and grain size of Nb_3Sn. The high kinetic energy promotes surface diffusion across atomic steps and edges, that allows homogeneous thin film growth. The low coherence length of only about $3\,\mathrm{nm}$ to $4\,\mathrm{nm}$ is likely to form weak link grain boundaries. This is why the reduction of the grain boundary density can suppress the TAPS observed for samples with low grain sizes by increasing the overall sputtering power.

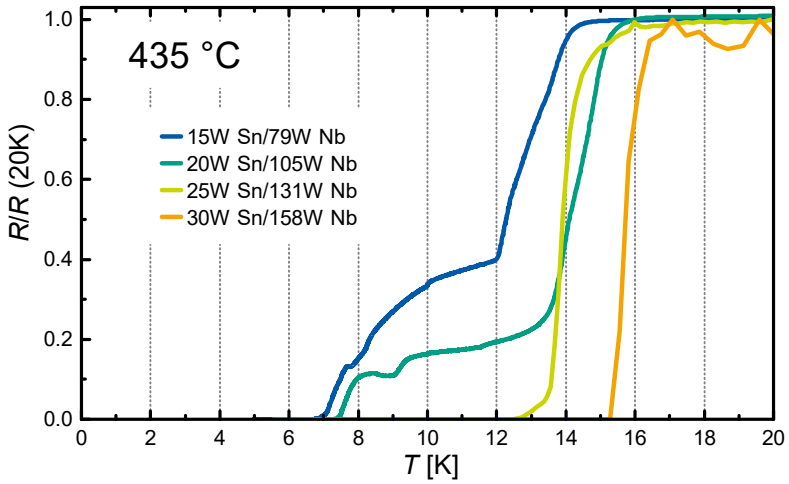

Figure 5.7.: Resistivity normalized to the resistivity at $20\,\mathrm{K}$ of sputtered Nb_3Sn thin films versus temperature. The power input is increased from $15\,\mathrm{W}$ Sn/$79\,\mathrm{W}$ Nb to $30\,\mathrm{W}$ Sn/$158\,\mathrm{W}$ Nb while the substrate temperature is fixed to $435\,^{\circ}\mathrm{C}$. T_c is determined at $90\,\%$ of the resistivity at $20\,\mathrm{K}$. Increasing overall sputtering power increased the primary transition temperature and hindered multi-step transitions.

Table 5.2.: Properties of Nb_3Sn grown on fused silica by co-sputtering. The sputtering power was increased from $15\,\mathrm{W}$ Sn/$79\,\mathrm{W}$ Nb to $30\,\mathrm{W}$ Sn/$158\,\mathrm{W}$ Nb at constant power ratio of 5.25 and $435\,^{\circ}\mathrm{C}$ substrate temperature. Tin content and FWHM of 210 Bragg peak are listed.

P_{Sn}/P_{Nb} [W/W]	Sn [At-%]	FWHM 210 [°]	$T_{c,90}$ [K]
15/79	17.7±0.7	0.367	13.8
20/105	25.3±0.3	0.387	15.1
25/131	24.1±0.3	0.368	14.8
30/158	25.7±0.2	0.337	16.3

5.1.4. Magnetic properties of the superconducting state

A sample sputtered at $435\,^{\circ}\mathrm{C}$ utilizing $30\,\mathrm{W}$ Sn/$158\,\mathrm{W}$ Nb was used to measure the magnetization versus temperature curve in a field of $2\,\mathrm{mT}$ perpendicular to the surface after zero field cooling (ZFC) and field cooling (FC). The curve is shown in Fig. 5.8, demonstrating a pronounced drop of the magnetization at $15.5\,\mathrm{K}$ for the ZFC curve while the FC demonstrates a slight decrease in the magnetization. The drop in the ZFC measurement is clear evidence for a strong shielding effect that originates from the superconducting surface currents. The huge difference in the ZFC and FC measurements at low temperatures indicates strong flux pinning, and the presence of pinning centers (defects), in the present sample. The defect size for flux pinning must be in the order of several nano meter (e.g. grain boundaries or impurities). Such defects are unfavorable in applications. However, flux pinning can also occur at surface imperfections. Hence, it cannot be concluded from this measurement which kind of imperfections act as pinning centers. Flux pinning plays no role in SRF cavities, since the critical field is chosen below H_{c1}. For SRF applications above H_{c1}, the depinning frequency should be taken in account [104, 105]. The onset temperature for the diamagnetic shielding is about $15.5\,\mathrm{K}$. This value must be compared to the point in the $R-T$ measurement in Fig. 5.7, where the curve reaches zero resistance and the shielding currents flow. The comparison shows that the points are identical in this case which gives the information that the critical temperature is perfectly homogeneous all over the sample. This can be stated from the fact that the $R-T$ measurement determines the critical temperature of the best superconducting path through the sample while the $M-T$ measurement determines the critical temperature of the weakest point (shielding currents flow through the whole sample).

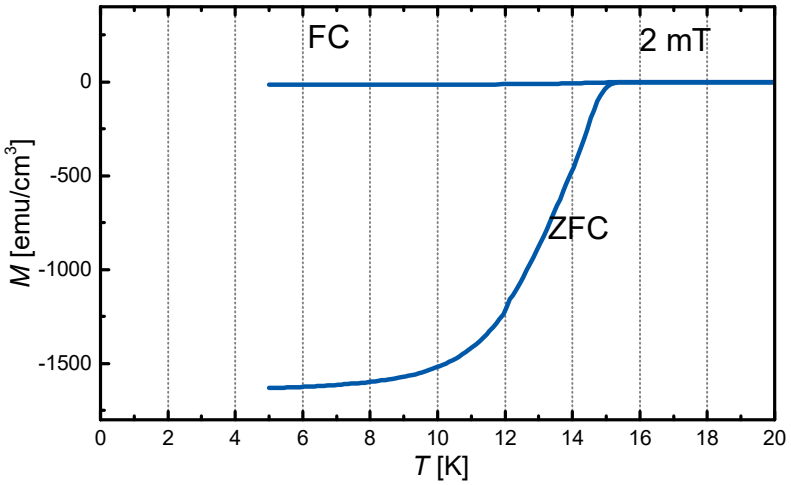

Figure 5.8.: Magnetization versus temperature measured in a field of $2\,\mathrm{mT}$ after zero field (ZFC) and field cooling (FC). Sample was Nb_3Sn sputtered at $435\,^{\circ}\mathrm{C}$ and 30 W Sn/158 W Nb. ZFC curves show strong shielding with a $T_{\mathrm{c},0}$ of $15.5\,\mathrm{K}$.

For further characterization, the hysteresis ($M-H$ measurement) is recorded as depicted in Fig. 5.9 in the range from $-6\,\mathrm{T}$ to $6\,\mathrm{T}$. For higher fields, the typical hysteresis of a hard superconductor is observed (see Fig. 2.16). At low fields however, flux jumps are observed that result in the shown fluctuation of magnetization [106, 107]. The onset field where the flux jumps start to occur, depends on the exerting force onto the flux lines in the pinning centers. This force is proportional to the superconducting current density that is temperature dependent (see Fig. 5.9). For this reason, the observed flux jumps are less pronounced for the hysteresis recorded at $10\,\mathrm{K}$. Such flux jumps create electrical resistivity which is the reason why they should be suppressed (see section 2.1.12) for stability criteria. Flux jumps in SRF cavities

can be suppressed by shunting via the cavity material that is demonstrated in section 5.5. The hysteresis curves can be used to determine the superconducting current density using relation 2.33, that is determined to be $1.6 \times 10^5\,\mathrm{A/cm^2}$.

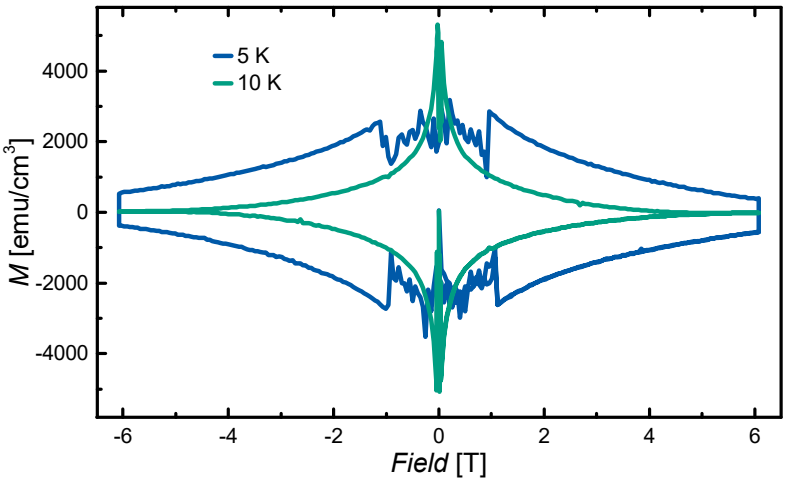

Figure 5.9.: Magnetization of sputtered Nb_3Sn thin films versus external magnetic field measured at $5\,\mathrm{K}$ and $10\,\mathrm{K}$. Flux jumps demonstrate temporary breakdown of the critical current.

5.1.5. Kinetic energy of out-sputtered niobium and tin

The impact of the kinetic energy (by adjustment of the sputtering power) on the superconducting properties is shown in the previous section. SIMTRA [108] is used to simulate the kinetic energy distribution of the out-sputtered niobium an tin atoms on the sample surface. The result is shown in Fig. 5.10 as a function of the sputtering power utilized in this work to synthesize Nb_3Sn. While the energy distribution of the niobium atoms do not change for the applied sputtering powers, the distribution of the tin atoms changes. For tin, not only higher energetic atoms are added to the distribution, but also the fraction of the high energetic atoms is increased by using higher sputtering powers. It must be concluded that the promoted phase formation of Nb_3Sn originates from the high energy tin atoms that are more likely to find desired locations by surface diffusion.

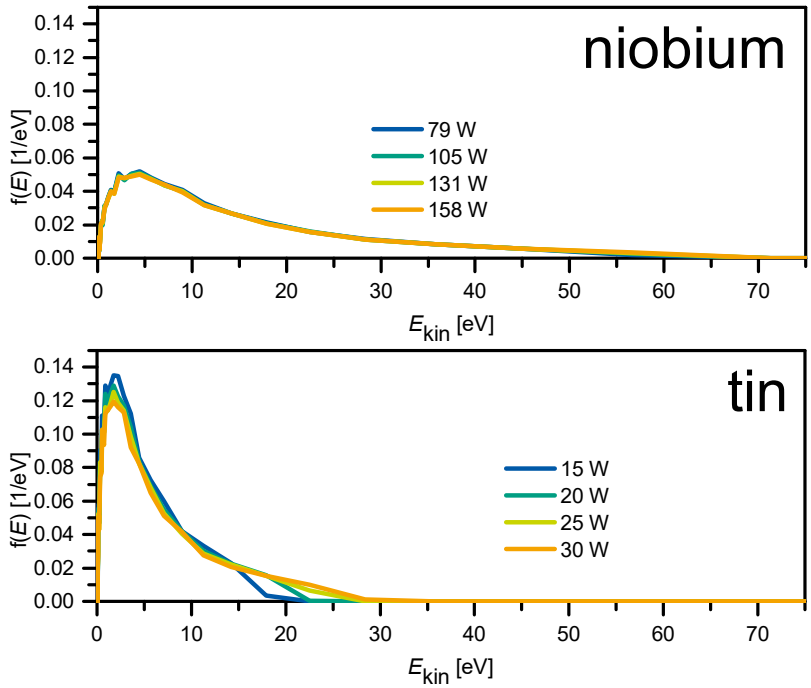

Figure 5.10.: Simulated kinetic energy distribution of sputtered species is plotted as a function of kinetic energy. Sputtering power ranges from $79\,\mathrm{W}$ to $158\,\mathrm{W}$ for niobium (top) and $15\,\mathrm{W}$ to $30\,\mathrm{W}$ for tin (bottom). While the kinetic energy distribution for niobium is weakly affected by the sputtering power in the given range, the amount of high energy tin atoms is increased.

5.2. Low temperature synthesis of Nb_3Sn

In Section 5.1, it is shown that Nb_3Sn was synthesized at $435\,^{\circ}\mathrm{C}$ with peak position matching the bulk values in XRD. Additionally, it was demonstrated that the overall sputtering power is beneficial for the sputtering properties. As it was discussed before, the deposition temperature should be as low as possible. For this reason, another series of samples was deposited at $320\,^{\circ}\mathrm{C}$ to investigate the role of kinetic energy at low thermal energy on the superconducting properties. $320\,^{\circ}\mathrm{C}$ was chosen for this series, since it was the lowest temperature with superconducting properties above the critical temperature of metallic niobium. Fig. 5.11 shows the XRD patterns of this series. It can be extracted that all samples are phase pure Nb_3Sn (space group $Pm\bar{3}n$). As it was observed for the series sputtered at $435\,^{\circ}\mathrm{C}$, the intensity ratio of 200, 210 and 211 reflections have no clear dependency from the sputtering power. The FWHM are significantly lower than the FWHM of the samples sputtered at $435\,^{\circ}\mathrm{C}$. However, the FWHM of reflection 210 is increasing with increasing sputtering power which is a contradiction to the series deposited at $435\,^{\circ}\mathrm{C}$. A second contradiction is given by the peak position of the 210 reflection that shifts relatively to the bulk positions from -0.1° to -0.3° for the sample sputtered at $15\,\mathrm{W}$ Sn/$79\,\mathrm{W}$ Nb and $30\,\mathrm{W}$ Sn/$158\,\mathrm{W}$ Nb, respectively. This indicates an increasing size of the unit cell with increasing sputtering power. A possible explanation can be given by the increasing sputtering rate due to the increased sputtering power. In this case, the crystal grows faster which can result in a higher dislocation density. This in return increases the size of the unit cell.

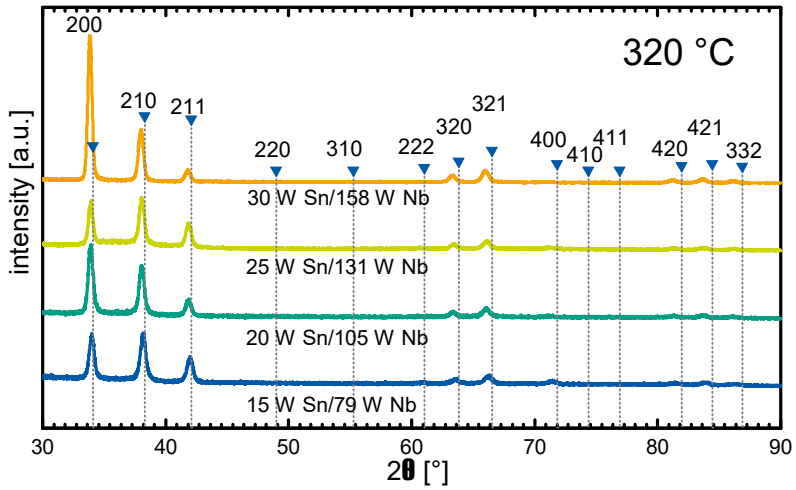

Figure 5.11.: XRD patterns of Nb_3Sn thin films grown on fused silica substrates. The sputtering power was increased from $15\,$W Sn/$79\,$W Nb to $30\,$W Sn/$158\,$W Nb while the substrate temperature was fixed to $320\,°$C at a power ratio of 5.25. All detected reflections are correlated to the Nb_3Sn ($Pm\bar{3}n$) indicating a high phase purity.

The $R-T$ measurements of this series is shown in Fig. 5.12. It can be clearly seen that there is a beneficial impact of the sputtering power on the critical temperature as well as the transition width ΔT from the normal conducting state into the superconducting state. As it was expected from the series sputtered at $435\,°$C, several discrete steps of the resistivity can be observed. The potential origin was discussed in Section 5.1. The values of the critical temperature of this series is listed in Tab. 5.3. The sputtering power has no clear impact on the critical temperature, since the lowest value of $9.43\,$K was measured for the sample sputtered at $25\,$W Sn/$131\,$W Nb and the highest for the sample sputtered at $30\,$W Sn/$158\,$W Nb. The highest value is achieved, as expected, for the highest sputtering power. However, it was not possible to reach values as high as in section 5.1 (samples grown at $435\,°$C).

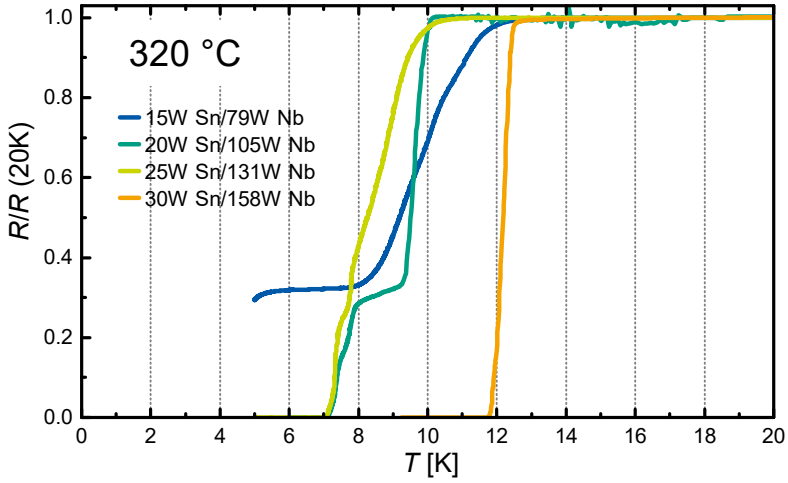

Figure 5.12.: Resistivity normalized to the resistivity at $20\,\mathrm{K}$ of Nb_3Sn thin films sputtered at $320\,^{\circ}\mathrm{C}$ versus temperature. The power input is increased from $15\,\mathrm{W}$ Sn/$79\,\mathrm{W}$ Nb to $30\,\mathrm{W}$ Sn/$158\,\mathrm{W}$ Nb while the substrate temperature is fixed to $435\,^{\circ}\mathrm{C}$. T_c is determined at $90\,\%$ of the resistivity at $20\,\mathrm{K}$. Increasing overall sputtering power increased the primary transition temperature and hindered multi-step transitions.

Table 5.3.: Properties of Nb_3Sn grown on fused silica by co-sputtering. The sputtering power was increased from $15\,\mathrm{W}$ Sn/$79\,\mathrm{W}$ Nb to $30\,\mathrm{W}$ Sn/$158\,\mathrm{W}$ Nb at constant power ratio of 5.25 and $435\,^{\circ}\mathrm{C}$ substrate temperature. Tin content and FWHM of 210 Bragg peak are listed.

P_{Sn}/P_{Nb} [W/W]	Sn [At-%]	FWHM 210 [°]	crystallite size [nm]	strain [%]	$T_{c,90}$ [K]
15/79	21.5±3.4	0.457	15.5	0.11	11.1
20/105	23.9±2.1	0.467	18.3	0.26	9.9
25/131	26.9±4.6	0.458	27.6	0.00	9.4
30/158	27.0±4.4	0.511	17.6	0.24	12.4

A conclusion from this series is that the kinetic energy of the sputtering process is beneficial for the superconducting phase formation. A drawback is that the increased kinetic energy comes with a higher growth rate (higher sputtering rate) that promotes high dislocations densities at the given substrate temperature of $320\,^{\circ}\mathrm{C}$. It can be stated that the lower synthesis temperature (and by that lower thermal energy) hinders optimal phase growth. In sum, the kinetic energy can replace thermal energy by some extent. Synthesis of well performing samples at lower temperatures than $435\,^{\circ}\mathrm{C}$ is not possible.

5.3. After-deposition annealing on sapphire

The presented process optimization could demonstrate pure phase formation with a $T_{c,90}$ of $16.31\,\mathrm{K}$ without consecutive annealing (see 5.1). This is outstanding 'as-deposited' thin film performance. However, the maximum achieved bulk value is about $18.3\,\mathrm{K}$. Trenikhina *et al.* could show that after-deposition annealing improves performance of thin films Nb_3Sn coated by single target sputtering on a heated substrate [109].

In this section, thin film Nb_3Sn is coated on Al_2O_3 substrate. Al_2O_3 is used in this section with after-deposition treatment, since it is chemically inert and with $14\,W\,m^{-1}\,K^{-1}$ to $30\,W\,m^{-1}\,K^{-1}$ an excellent thermal conductor in the class of oxides [110]. As the sample is heated from the backside, Al_2O_3 can increase the maximal annealing temperature. A set of samples was deposited at $320\,°C$ and $435\,°C$ each with annealing at $300\,°C$, $500\,°C$ and $730\,°C$ to investigate the optimal deposition temperature in combination with optimal annealing temperature. The tin content of the sample set sputtered at $320\,°C$ as a function of annealing time is show in Fig. 5.13 (left) and the sample set sputtered at $435\,°C$ in Fig. 5.13 (right). It can be seen that the tin content is not strongly affected by the annealing at $300\,°C$, $500\,°C$ and $730\,°C$ for the samples sputtered at $320\,°C$. The samples sputtered at $435\,°C$ show an unsteady trend of tin content. Considering the tin content increase after decrease, there is only one possible explanation indicating an inhomogeneous tin content all over the sample after annealing. Since the measured area in EDX is only a few micro meter square, inhomogeneous tin content can affect the result of the measurement.

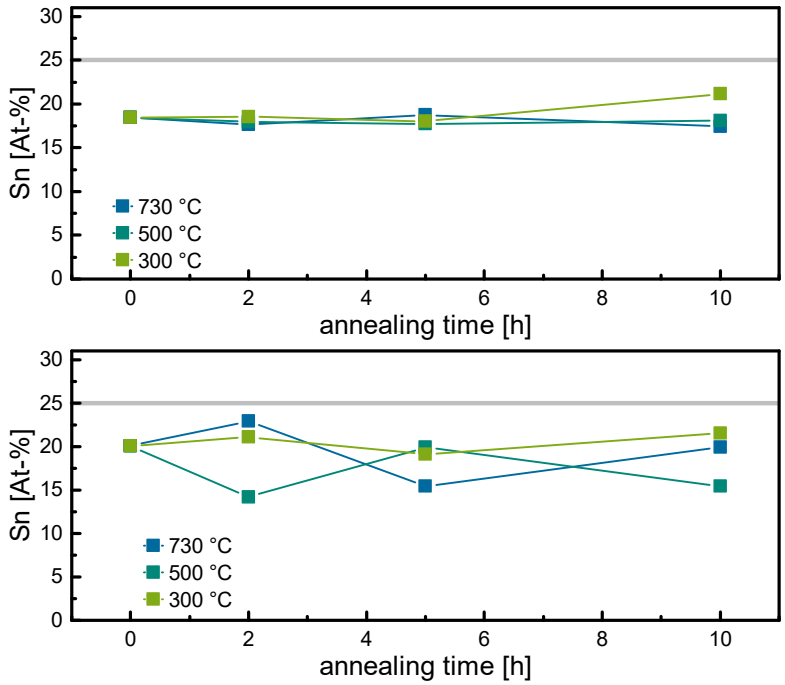

Figure 5.13.: Tin content measured by EDX is plotted as function of after-deposition annealing time in high-vacuum (10×10^{-6} mbar). Deposition conducted at $30\,W$ Sn/$158\,W$ Nb while the substrate temperature is fixed to $320\,°C$ (top) and $435\,°C$ (bottom). The utilized annealing temperatures range from $300\,°C$ to $730\,°C$. The stoichiometric tin content in Nb_3Sn of $25\,\%$ is marked by the gray line.

XRD patterns of the sample set sputtered at $435\,°C$ are depicted in Fig. 5.14. It can be clearly seen that the samples sputtered on Al_2O_3 could be coated with phase pure Nb_3Sn as it was demonstrated for thin films coated on fused silica. All samples annealed at $300\,°C$, $500\,°C$ and $730\,°C$ show only Nb_3Sn reflections demonstrating that the previously grown phase did not decompose. The FWHM of the Nb_3Sn reflections provide information about the Nb_3Sn phase and the impact of the annealing on the crystal. Peak broadening of the XRD reflections is a measure of crystal quality and can have two crystal related origins, strain and crystallite size. Strain and crystallite size can be investigated separately by Williamson-Hall plots based on the Scherrer equation [111]. The method was applied for TiO_2 by Kibasomba *et al.* [112] for that it was found to underestimate the crystallite size by $14\,\%$. For this reason, the Williamson-Hall plot

was used for a relative comparison of the crystallite size as a development over annealing time.

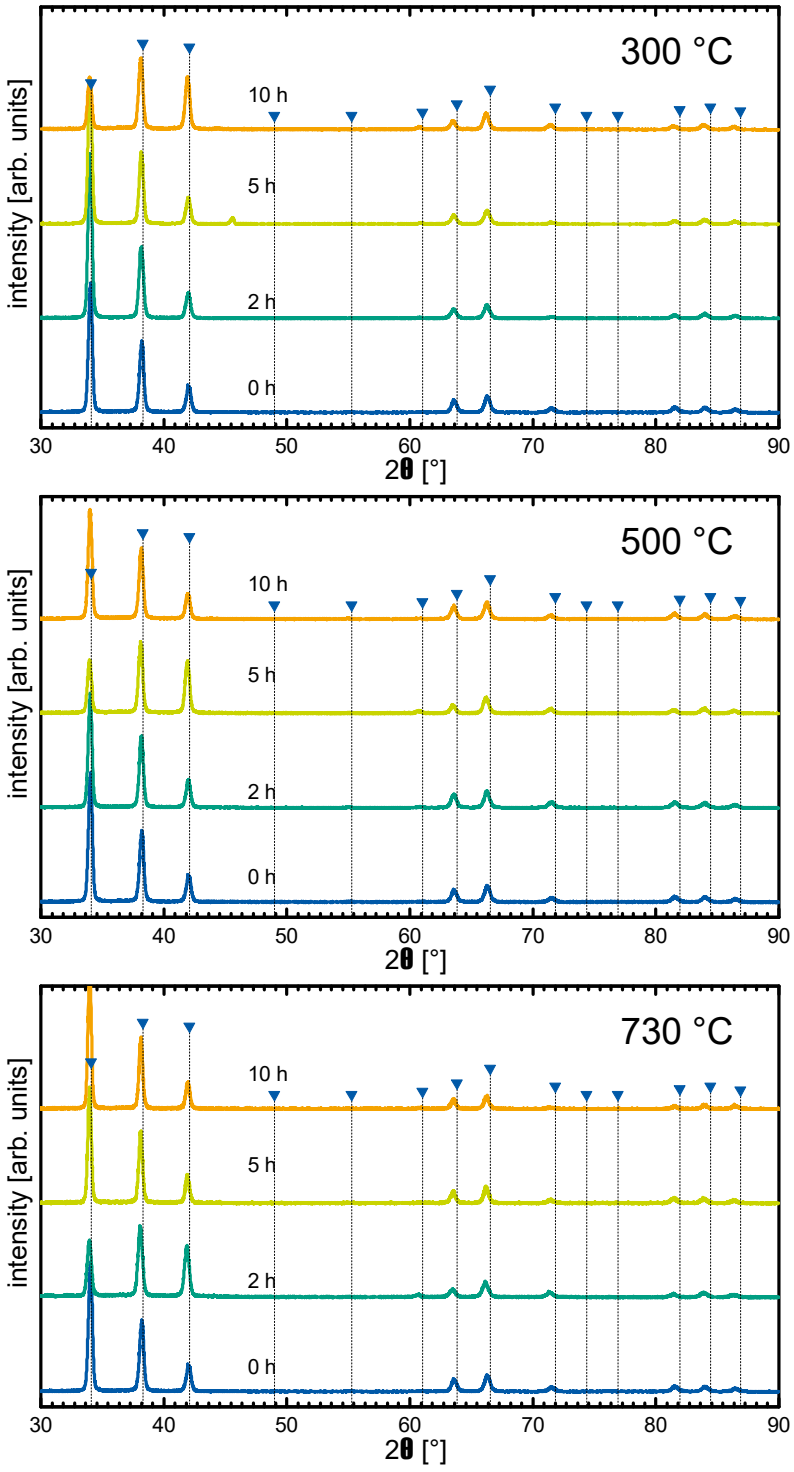

Figure 5.14.: Grazing incidence XRD (GXRD) patterns of samples sputtered at $435\,^{\circ}\mathrm{C}$ as function of after-deposition annealing time in high-vacuum. Deposition conducted at $30\,\mathrm{W}$ Sn/$158\,\mathrm{W}$ Nb while the substrate temperature is fixed to $435\,^{\circ}\mathrm{C}$. The utilized annealing temperatures range from $300\,^{\circ}\mathrm{C}$ to $730\,^{\circ}\mathrm{C}$. Nb_3Sn reflections are marked with tip down triangles.

The crystallite size determined by the Williamson-Hall plot of the sample sets is shown in Fig. 5.15.

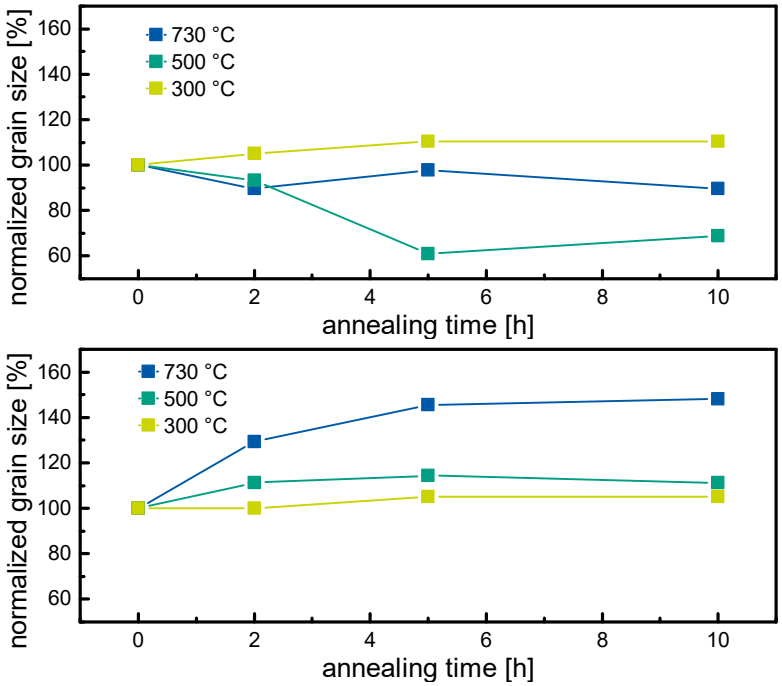

Figure 5.15.: Crystallite size determined by the Williamson-Hall plot is plotted as function of after-deposition annealing time in high-vacuum and normalized to the as-deposited crystallite size. Deposition conducted at 30 W Sn/158 W Nb while the substrate temperature is fixed to 320 °C (top) and 435 °C (bottom). The utilized annealing temperatures range from 300 °C to 730 °C.

It is to be noted that this method provides a well averaged crystallite size of the whole sample. Fig. 5.15 (left) shows the crystallite sizes of the samples sputtered at 320 °C while Fig. 5.15 shows the crystallite sizes of the samples sputtered at 435 °C. It can be extracted that annealing at 300 °C is beneficial for grain growth for both sputtering temperatures. It can be further seen that the annealing temperatures 500 °C and 700 °C are decreasing the average crystallite size for the samples sputtered at 320 °C. The same annealing temperatures could, however, increase the average crystallite sizes of the samples sputtered at 435 °C. Howard *et al.* stated that recrystallization requires annealing at 800 °C or above [113]. Kolosov and Shevyrev report that the recrystallization of Nb_3Sn take about 15 h at 900 °C to 1000 °C and 1 h at 1200 °C [114]. Recrystallization can be explained by the mobility of dislocations at elevated temperatures forming small angle grain boundaries and by that, a temporary decrease of crystallite size. These small angle grain boundaries then form large angle grain boundaries. In the last step of recrystallization, large grains grow in favor of small grains increasing the average crystallite size. Transferring the model of recrystallization to the obtained crystallite sizes of this work, two possible conclusions can be drawn. One is that the samples sputtered at 320 °C have more dislocations in comparison to the samples sputtered at 435 °C. The other is that the grain boundary formation of the sample set sputtered at 435 °C was finished during deposition while the grain boundary formation of the sample set sputtered at 320 °C started in the annealing step. The unfinished recrystallization is however, the less likely explanation. An unfinished recrystallization would show an increase in crystallite size after a short drop. It must be noted that the crystallite size measurements of a curve cannot be performed on a single sample, since the crystallite size measurements are not carried out in-situ and interruptions of the annealing can have unexpected influences. For this reason, it must be considered that the samples of one curve could have different 'as-deposited'

crystallite size distributions affecting the crystallite sizes after annealing. However, it is likely that the samples sputtered at $435\,^{\circ}$C and annealed at $\geq 500\,^{\circ}$C exhibit larger crystallite sizes due to annealing.

The resistivity versus temperature curves of the sample set sputtered at $435\,^{\circ}$C is shown in Fig. 5.16. The plotted measurements all show a multi-step transition behavior as it was observed in the previous sections where it could be solved by increasing the sputtering power during deposition. Unfortunately, it is neither possible to improve the onset of T_c by annealing nor is it possible to get rid of the multi-step transition behavior. Although there is not a clear trend of transition widths as a function of annealing time, it can be seen that the transition width increases for all annealed samples in relation to the not annealed sample. The origin of the multi-step is discussed in the previous section. Annealing could potentially worsen both, tin distribution and weak links.

It must be concluded from the annealing experiments that annealing at $730\,^{\circ}$C was observed to increase the average crystallite size of the thin films sputtered at $435\,^{\circ}$C. Additionally, it was not harmful for the Nb_3Sn phase as it was seen from XRD patterns. However, the performance in terms of T_c could not be improved by annealing after the deposition. Unfortunately, the onset temperature of the transition decreased while the transition width increased due to annealing.

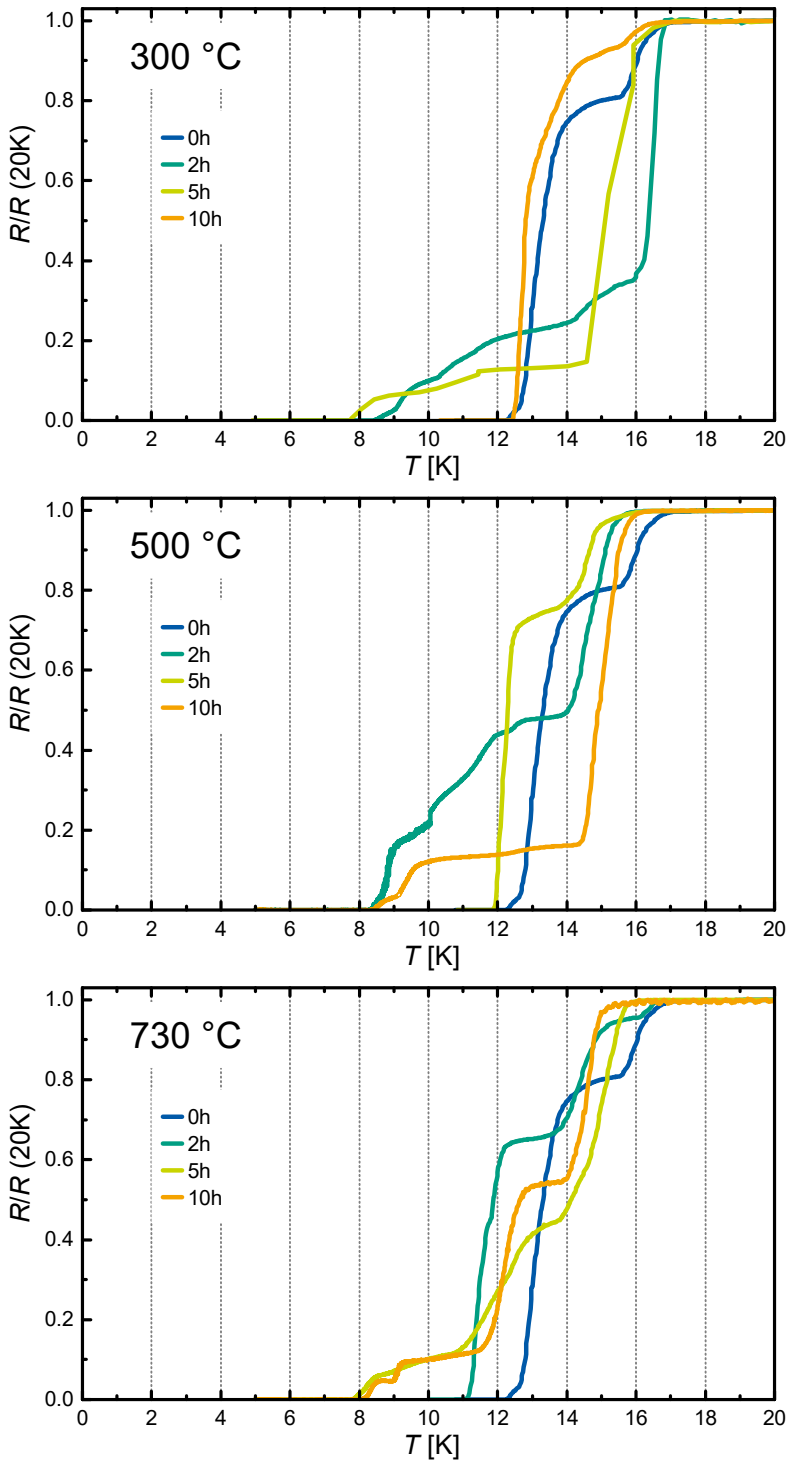

Figure 5.16.: Resistivity normalized to the resistivity at $20\,\mathrm{K}$ as function of temperature for samples annealed after deposition in high-vacuum. Deposition conducted at $30\,\mathrm{W}$ Sn/$158\,\mathrm{W}$ Nb while the substrate temperature is fixed to $435\,^{\circ}\mathrm{C}$. The utilized annealing temperatures range from $300\,^{\circ}\mathrm{C}$ to $730\,^{\circ}\mathrm{C}$.

The plotted measurements all show a multi-step transition behavior as it was observed in the previous sections where it could be solved by increasing the sputtering power during deposition. Unfortunately, it is neither possible to improve the onset of T_c by annealing nor is it possible to get rid of the multi-step transition behavior. Although there is not a clear trend of transition widths as a function of annealing time, it can be seen that the transition width increases for all annealed samples in relation to the not annealed sample. The origin of the multi-step is discussed in the previous section that remains unclear. Annealing could potentially worsen both, tin distribution and weak links.

5.4. Influence of the (local) structure and grain boundary condition on the performance

The origin of the footprint structure in the resistivity versus temperature measurements (see Fig. 5.7 and 5.17) could not be identified yet. So far, this phenomenon has been discussed for Nb_3Sn by Posen *et al.* [28] and Perpeet *et al.* [30]. For high-temperature superconductors (HTS) it is discussed by Alff *et al.* [102] and Wang *et al.* [115]. It is reported that in HTS grain boundaries have a strong impact on the superconducting performance [116]. Although Nb_3Sn is not a HTS, it has a comparable short coherence length of only $3\,$nm to $4\,$nm [21, 61]. As a consequence, the grain boundaries have the same high impact on the superconducting properties as in HTS. Grain boundaries can limit the critical current [115] that also limits the shielding behavior in SRF applications. Grain boundary segregations in the range of $3\,$nm are reported in Nb_3Sn coatings [116]. It was previously shown in this work how the foot print structure was suppressed by high sputtering powers. In spite of that, annealing after deposition could not suppress the issue.

5.4.1. Grain boundary critical current

Field dependent current-voltage characteristics are measured on samples sputtered at $320\,^{\circ}$C to investigate the grain boundary impact on the physical properties at $4\,$K (target operation temperature). At first, the resistivity versus temperature measurements of the samples were measured to find a suitable temperature for the measurement and find two different samples with and without footprint structure. The measurements are shown in Fig. 5.17 and the extracted information is summed up in Tab. 5.4. From these measurements, it can be seen that the sample sputtered at $30\,$W Sn/$158\,$W Nb has a sharp transition with a low transition width while the sample sputtered at $15\,$W Sn/$79\,$W Nb has a broad transition width with a plateau in the range of $8\,$K to $5\,$K. Although the samples did not perform well in terms of critical temperature, the different slope in the resistivity versus temperature measurement is suitable to find the origin of the multi-step transition.

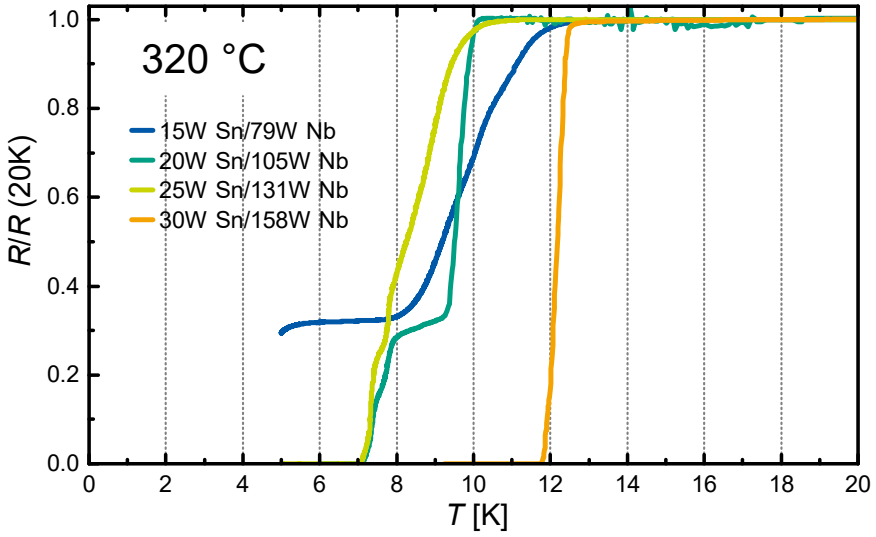

Figure 5.17.: Resistivity normalized to the resistivity at $20\,\mathrm{K}$ of sputtered Nb_3Sn thin films as a function of temperature. T_c is determined at $90\,\%$ of the resistance at $20\,\mathrm{K}$. During the growth of the different samples, the power input was increased from $15\,\mathrm{W}$ Sn/$79\,\mathrm{W}$ Nb to $30\,\mathrm{W}$ Sn/$158\,\mathrm{W}$ Nb while the substrate temperature was set to $320\,^{\circ}\mathrm{C}$.

Table 5.4.: Properties of Nb_3Sn grown on fused silica by co-sputtering. The sputtering power was increased from $15\,\mathrm{W}$ Sn/$79\,\mathrm{W}$ Nb to $30\,\mathrm{W}$ Sn/$158\,\mathrm{W}$ Nb at constant power ratio of 5.25 and $435\,^{\circ}\mathrm{C}$ substrate temperature. Tin content and FWHM of 210 Bragg peak are listed.

P_{Sn}/P_{Nb} [W/W]	Sn [At-%]	FWHM 210 [°]	crystallite size [nm]	strain [%]	$T_{c,90}$ [K]
15/79	21.5±3.4	0.457	15.5	0.11	11.1
20/105	23.9±2.1	0.467	18.3	0.26	9.9
25/131	26.9±4.6	0.458	27.6	0.00	9.4
30/158	27.0±4.4	0.511	17.6	0.24	12.4

Figure 5.18 shows the field dependent current-voltage characteristics of samples sputtered at $15\,\mathrm{W}$ Sn/$79\,\mathrm{W}$ Nb and $30\,\mathrm{W}$ Sn/$158\,\mathrm{W}$ Nb. The external field was ranged from $0\,\mathrm{mT}$ to $200\,\mathrm{mT}$. It can be seen that the voltage increases for both samples at a certain current. Below this current value, no voltage is measured. In case of the sample sputtered at $15\,\mathrm{W}$ Sn/$79\,\mathrm{W}$ this value changes from $22\,\mathrm{mA}$ to $15\,\mathrm{mA}$ with increasing external magnetic field. For the sample sputtered at $30\,\mathrm{W}$ Sn/$158\,\mathrm{W}$ Nb the voltage increases at around $38\,\mathrm{mA}$. This value does not change with the increasing external magnetic field. The behavior of both samples can be explained by a weak link grain boundary. This means that the grain boundary limits the critical current J_{GB} flowing trough the grain boundary. J_{GB} can be calculated dividing the critical current value by the cross section of the sample and is determined to be around $2.44 \times 10^3\,\mathrm{A\,cm^{-1}}$ and $2.50 \times 10^3\,\mathrm{A\,cm^{-1}}$ for the samples sputtered at $15\,\mathrm{W}$ Sn/$79\,\mathrm{W}$ Nb and $30\,\mathrm{W}$ Sn/$158\,\mathrm{W}$ Nb, respectively. The shown current-voltage characteristics and its field dependence is clear evidence that the grain boundaries are Josephson-type junctions [117, 118]. However, the superconducting properties are not affected below the critical current. It remains unclear by which extent the vortex penetration would increase the surface

resistivity and at which acceleration gradients the vortex penetration starts. The different response of the two samples can be explained by different grain boundary states. The critical current of the sample sputtered at 15 W Sn/79 W Nb was shown to have a strong dependence from the external magnetic field. The reason is found in a high grain boundary thickness distribution over the cross-section of the sample. In contrast to that, the sample sputtered at 30 W Sn/158 W Nb demonstrated a weak dependence from the external magnetic field. This means that the grain boundary network of this sample would not be detrimental for the application below the critical current. Since grain boundaries are effective pinning centers in Nb_3Sn [119, 120], unfavorable grain boundary network conditions generally result in additional RF power loss.

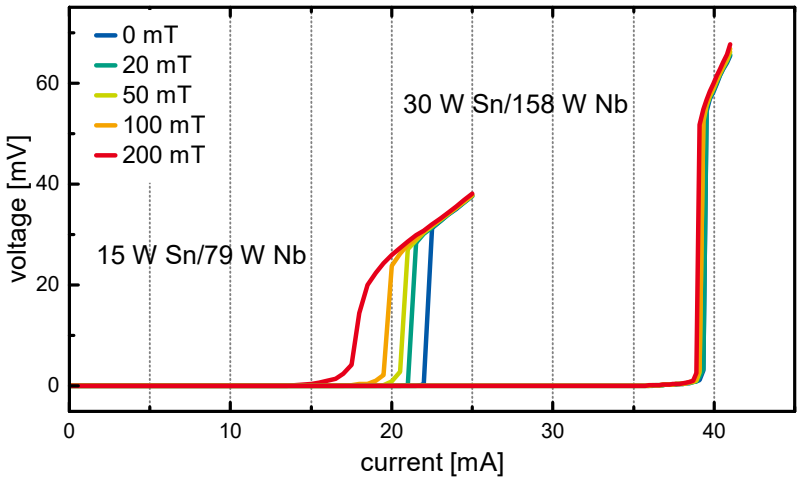

Figure 5.18.: Voltage of samples sputtered at 320 °C as a function of current at 4 K. The power input is increased from 15 W Sn/79 W Nb to 30 W Sn/158 W Nb while the substrate temperature is fixed to 320 °C. The external field applied was increased from 0 mT to 200 mT.

The field dependence as measured for the sample sputtered at 15 W Sn/79 W Nb is a necessary condition for a weak link Josephson-junction. However, only the Fraunhofer-pattern is a proof for a Josephson-junction. Such a pattern could not be measured for both samples. There are two possible reasons, a low resolution of the magnetic field applied or a network of several weak links manipulating the current randomly. The main conclusion is that even the sample with the sharp transition (weak impact of external field) shows grain boundaries acting as weak links are found. In this sample however, the grain boundary condition is homogeneous. This does not affect the operation of an SRF cavity below the critical current. Single grain boundaries in bad condition can limit the critical current density [115] and indirectly lower the shielding capability in the Meissner state (important aspect for SRF cavities). Therefore, it is favorable to have a high critical current density with homogeneous grain boundary condition. Such favorable homogeneities can be addressed by high sputtering powers. Another severe performance limitation is off-stoichiometry that can be the result of grain boundary segregation. As previously discussed, the demonstrated grain boundary segregation can lead to off-stoichiometry within the grains which can decrease the superconducting properties.

5.4.2. Effect of local structure

Extended x-ray absorption fine structure (EXAFS) combined with x-ray absorption (XA) mapping was used to examine the local and micro environment (e.g. off-stoichiometry) of the previous samples sputtered

at 15 W Sn/79 W Nb and 30 W Sn/158 W Nb in the two dimensions. The XA mappings can be seen in Fig. 5.19a) for the sample sputtered 30 W Sn/158 W Nb and 5.19b) for the sample sputtered at 15 W Sn/79 W Nb.

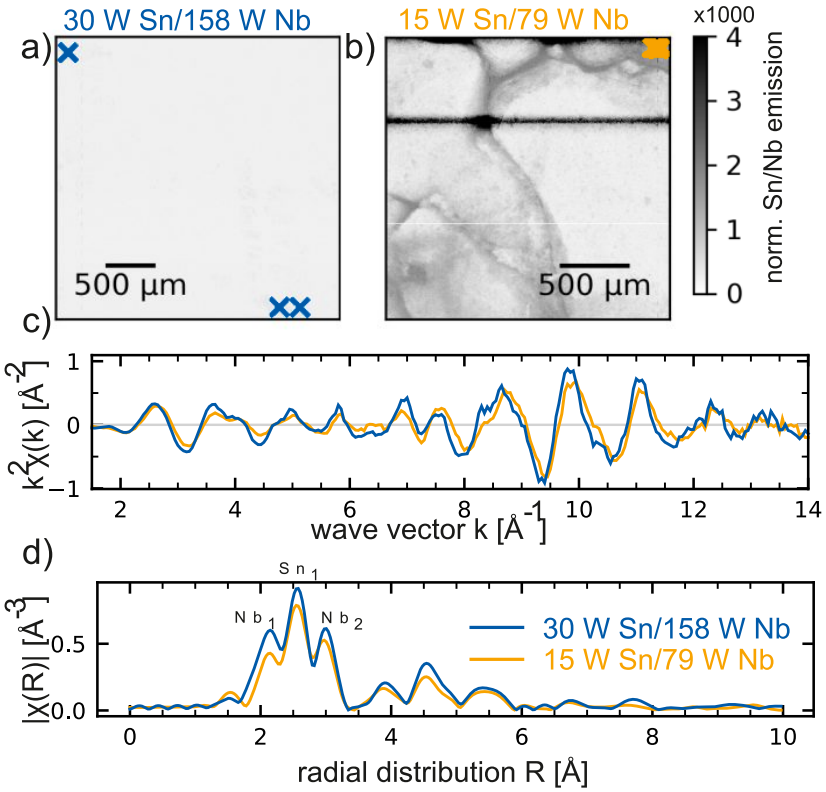

Figure 5.19.: XAS mapping patterns of Nb_3Sn thin films grown on fused silica substrates. Emission line ratio mapping of the sample a) 30 W Sn/158 W Nb and b) 15 W Sn/79 W Nb. c) k^2-weighted measured EXAFS $\chi(k)$ at the Nb K-edges. d) FFT of spectra. The first three maxima correspond to signals coming from the next neighbors Nb_1, Sn_1 and Nb_2.

The sample sputtered at 15 W Sn/79 W Nb shows a high gradient in the ratio between the Nb to Sn emission lines. From this difference, it can be assumed that the sample has a large difference in the local chemical composition. In contrast to that, the sample sputtered at 30 W Sn/158 W Nb shows a highly homogeneous ratio of the Nb and Sn emission lines of about 0.3. From this comparison, deviations in tin concentration can be concluded on micro-scale for the sample sputtered at 15 W Sn/79 W Nb. The colored markings of the present figures shows the spots of the samples where the EXAFS spectra were recorded and the local surrounding was investigated. All measured spectra were merged, since no deviation of the background noise was observed. The absorption edge of Nb was used to investigate the surrounding of the Nb atoms. In Fig. 5.19c), the spline and background corrected k^2-weighted EXAFS oscillations $\chi(k)$ is plotted for both measured samples at ambient temperature. The fast Fourier transform (FFT) of $\chi(k)$ is shown in Fig. 5.19d) providing information about the bond length between the absorbing atom and the next atomic neighbor. The backscattering amplitudes of Nb_1, Sn_1 and Nb_2 can be seen in this figure where Nb_1 represents Nb in the first backscattering shell, Sn_1 Sn in the first backscattering shell and Nb_2 Nb in the second backscattering shell. The comparison of the spectra of the two samples shows an eminent difference in the amplitude. From this difference it can be concluded that there are differences in the local structure on atomic-scale besides the segregations on micro-scale (XA). This means that the sample sputtered at

15 W Sn/79 W Nb has a much stronger disorder in relation to the sample sputtered at 30 W Sn/158 W Nb. The lower amplitude can be explained as disturbances in the individual paths or additional disturbing phase. The measured frequencies and the fit indicate a similar radial distribution of both samples. The real distances within the first atomic shell were determined utilizing FEFF9 [121] and the software package larch [122] using the pristine Nb_3Sn structure. The range set for FFT is 2.3 Å^{-1} to 14 Å^{-1} and the fitting windows was set to 1.8 Å to 3.2 Å for both spectra. The fitting results are summed up in Tab. 5.5. It can be extracted that the atomic distances Nb-Nb and Nb-Sn are smaller in the sample sputtered at 15 W Sn/79 W Nb and the static disorder σ_i^2 is significantly larger than for the sample sputtered at 30 W Sn/158 W Nb within this model. The calculated lattice constant from XRD measurements is 5.279 61(6) Å and 5.2987(3) Å for the samples sputtered at 15 W Sn/79 W Nb and 30 W Sn/158 W Nb, respectively.

Table 5.5.: Fit parameters for the first 3 paths. Here, S_0^2 is the amplitude reduction factor, ΔE_0 is the difference between experiment and theory in eV and σ_i^2 is the mean square deviation in path length. Fixed parameters in the fit are marked with an asterisk.

paths	N*	R_{fit} [Å]	σ^2 [Å^2]	S_0^2*
30 W Sn/158 W Nb				
Nb_0 - Nb_1	2	2.656(8)	0.0043(6)	0.7
Nb_0 - Sn_1	4	2.965(12)	0.0063(7)	0.7
Nb_0 - Nb_2	8	3.261(10)	0.0093(7)	0.7
15 W Sn/79 W Nb				
Nb_0 - Nb_1	2	2.643(17)	0.0062(16)	0.7
Nb_0 - Sn_1	4	2.930(29)	0.0082(20)	0.7
Nb_0 - Nb_2	8	3.255(22)	0.0108(16)	0.7

The XA mappings allow to state that Nb_3Sn is more likely to form a multi-step transition from normal to superconducting state when tin segregation occurs. Segregation can be the consequence from a lack of energy during phase formation. This can be solved, as preciously discussed, by an increase of sputtering power during film growth. EXAFS measurements could confirm disorders in the lattice on an atomic-scale. However, it is not possible to state which kind of atomic defects are formed in the crystal structure. For this reason, a tunneling electron microscope (TEM) is used to take images of the local crystal structure. These images are shown in Fig. 5.20 for the samples sputtered at 15 W Sn/79 W Nb and 30 W Sn/158 W Nb.

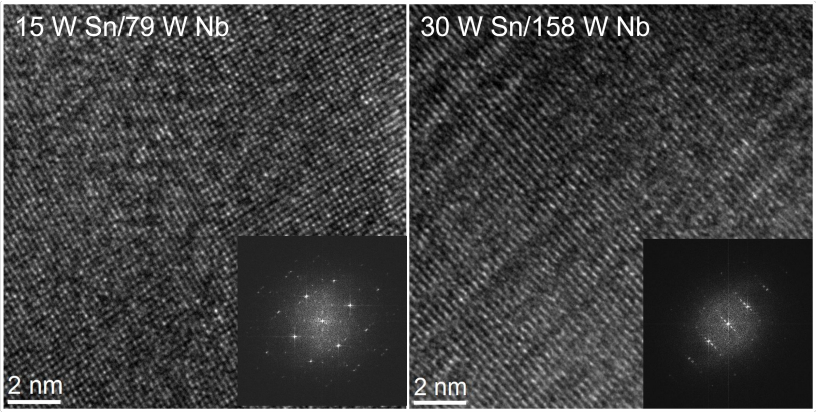

Figure 5.20.: HR-TEM images of Nb_3Sn thin films grown on fused silica substrates. The sample (left image) was sputtered at $15\,\mathrm{W}$ Sn/$79\,\mathrm{W}$ Nb and (right image) $30\,\mathrm{W}$ Sn/$158\,\mathrm{W}$ Nb. Bottom right corner shows the fast Fourier transformation (FFT) of the respective HR-TEM images.

The images show the lattice of single Nb_3Sn grains. It is clear from the the images that there are no significant differences of the lattice visible as it was extracted from the EXAFS measurements. The change in brightness of the atoms can be explained as measurement related artefacts. In sum, it can not be solved exactly which kind of defects are the origin of the multi-step transition. It can be stated that the origin is found in the grain boundaries. Differences on atomic-scale of the grains could be found, but cannot explain the discrete levels of the multi-step transition.

5.5. Performance on copper substrate

Copper is the candidate-of-choice as carrier material for thin film coated SRF cavities, since it has optimal heat conducting properties among all metals and allows easy manufacturing as well as a low price in relation to bulk niobium cavities. So far it has been demonstrated that the co-sputtering process used in this work could synthesize Nb_3Sn in a phase pure state at temperatures below $500\,^\circ\mathrm{C}$ that is a requirement for the coating of copper cavities. The reason is the copper melting point T_m of $1085\,^\circ\mathrm{C}$. Following a simple approximation [123], copper diffusion starts at about $400\,^\circ\mathrm{C}$. To minimize copper diffusion into the superconducting film, it is necessary to keep the synthesis temperature as low as possible and the synthesis duration as short as possible. In this section, the process parameters for copper substrate is investigated as well as the feasibility of the coating on copper for high-performance copper based SRF cavities. At first, the copper diffusion into the Nb_3Sn thin film at $520\,^\circ\mathrm{C}$ is investigated. Second, adhesion tests in two different conditions as-deposited and aged (temperature decreased from $300\,\mathrm{K}$ to $5\,\mathrm{K}$ and vice versa) are performed to demonstrate the adhesion of the film on the substrate as well as the durability of the coating. Third, the superconducting properties are investigated as a function of the thin film thickness. At last, the as-deposited surface roughness of the thin film is discussed as a function of the film thickness.

5.5.1. Elemental depth profile of Nb_3Sn on copper substrate

To investigate the copper diffusion into the superconducting film, a stoichiometric Nb_3Sn thin film was grown on copper substrate at a substrate temperature of $520\,^\circ\mathrm{C}$. Fig. 5.21 (top) shows the depth profile recorded with x-ray photoelectron spectroscopy (XPS) inclusively ion beam etching between the measurements.

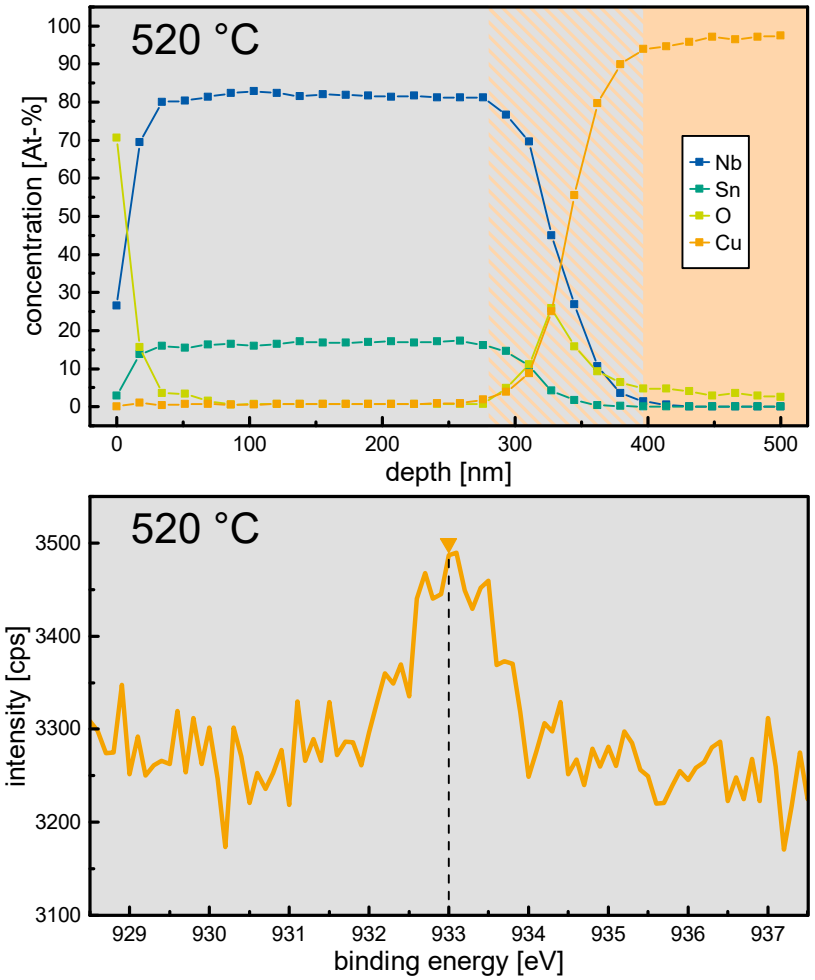

Figure 5.21.: XPS depth profile (top) of Nb_3Sn thin film grown on copper substrate sputtered at $520\,°C$ for $30\,min$ utilizing $158\,W$ Nb / $30\,W$ Sn. The average film thickness of area $2\,mm$ x $2\,mm$ is determined to be $350\,nm$. Gray background marks Nb_3Sn thin film coating. Orange background marks copper substrate. Interface region of $120\,nm$ is marked by dashed area. Cu2$p_{3/2}$ emission within the coating is plotted as a function of binding energy (bottom). Binding energy of Cu metal is marked with tip down triangle.

The surface region, as expected, consists of several oxides. After etching about $50\,nm$ the oxygen signal drops to $0\,At-\%$. From this point on, the atomic percentages of Nb and Sn are about $80\,At-\%$ and $20\,At-\%$, respectively. The atomic ratio stays almost constant all-over the film. After etching of about $275\,nm$, the copper and oxygen signal start to increase while the Nb and Sn signal decreases. This indicates that the etching has reached the copper substrate. The oxygen signal can be explained as copper oxides at the surface of the substrate before the thin film coating. The copperoxide film thickness is estimated to be about $125\,nm$. After about $400\,nm$, the Nb and Sn signals simultaneously reach $0\,At-\%$. Using maxima and minima of the Nb, Sn and Cu signal, the over $2\,\mu m$ x $2\,\mu m$ (beam size) averaged thickness of the interface region is estimated to be $120\,nm$. Fig. 5.21 (bottom) shows the Cu2$p_{3/2}$ signal at a position between the surface and interface region. The measurement shows only a weak signal of Cu. Such intensities do not allow a quantification, since a proper peak area fitting is not possible. However, a content of much less than $1\,At-\%$ can be assumed. It must be noted that the copper oxide inter-layer can reduce the heat conductivity

and must be removed in order to optimize the SRF performance. The stoichiometry determined by XPS of the sample differs from the desired ratio of $75{:}25\,\mathrm{At}-\%$ in favor of Nb with $80{:}20\,\mathrm{At}-\%$. This can be explained by preferential sputtering of Sn out of the Nb_3Sn film by the ion beam. The constant signals demonstrate an excellent depth homogeneity. The obtained inter-layer width is in the range of the surface roughness of the substrate. It is further shown that the substrate surface was oxidized due to contact with air before the coating process. These oxides must be removed to improve cryogenic efficiency. From this experiment it is clear that the film contains a small amount of copper. A few percent of copper can already lower the performance of Nb_3Sn [21]. It remains unclear, if concentrations less than $1\,\mathrm{At}-\%$ already lower the performance. In conclusion, it could be shown that the process is able to coat Nb_3Sn on copper with light diffusion of copper into the film. There is no evidence found of tin diffusion into the substrate or a tin-rich surface layer as found by Hillenbrand *et al.* [19].

5.5.2. Film thickness influence on phase growth

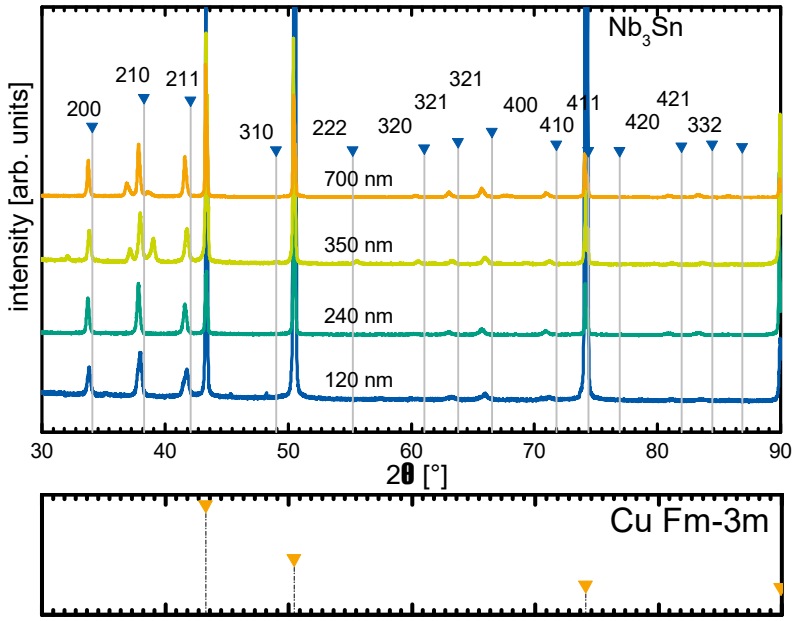

Figure 5.22.: XRD patterns of Nb_3Sn thin films grown on copper substrates. The film thickness was increased from $120\,\mathrm{nm}$ to $700\,\mathrm{nm}$ while the substrate temperature was fixed to $480\,^{\circ}\mathrm{C}$ at a power ratio of 5.25 (Nb:Sn). Reflections of Nb_3Sn ($Pm\bar{3}n$) are marked with tip down triangles. Reflections of Cu ($Fm\bar{3}n$) are provided for comparison.

A series of samples with gradually increasing Nb_3Sn thin film thickness was grown on copper substrates to investigate the influence of the process duration (taking place at elevated temperature) on the phase growth and morphology. The film thickness was adjusted via coating duration that was set to $10\,\mathrm{min}$, $20\,\mathrm{min}$, $30\,\mathrm{min}$ and $60\,\mathrm{min}$. The results was a film thickness of about $120\,\mathrm{nm}$, $240\,\mathrm{nm}$, $350\,\mathrm{nm}$ and $700\,\mathrm{nm}$, respectively. To measure the film thickness, ion beam etching (IBE) was used to etch off the film. A profilometer was then used to measure the height of the etched area in respect to the original film height. The etching duration together with the etching depth was used to estimate an etching rate per minute. The rate was used to determine the film thickness of this series. The XRD patterns of this series are shown in Fig. 5.22. The reflections of the measurements match all reflections of the desired Nb_3Sn phase of space group $Pm\bar{3}n$. Additional reflections can be associated with the copper phase of space group $Fm\bar{3}m$. The samples

of thickness 350 nm and 700 nm show reflections that could potentially match Nb-Sn intermetallics with higher Sn content (e.g. $NbSn_2$ and Nb_6Sn_5) than Nb_3Sn. Since these phases are energetically favorable [76, 124, 125, 126, 81], a longer coating duration could lead to a decomposition of Nb_3Sn. A clear identification is not possible due to low peak areas and different peak area ratios of the two samples. It must be concluded that there are at least two different unidentified phases. This means that there are two counteracting processes, the promotion of the thermodynamic unfavorable Nb_3Sn and its decomposition at moderate temperatures for long coating duration. The decomposition could not be observed for films on sapphire substrate for long annealing times (see Section 5.3). In sum, the kinetically induced phase formation of Nb_3Sn is outstanding and allows coating of copper. Long synthesis duration however, may promote a decomposition of the phase in the given temperature regime.

5.5.3. Surface roughness

Since the surface roughness influences the superheating field H_{SH},[127, 128] the quality of the surface must be examined. The as-deposited surface of a series of increasing thickness is investigated using an atomic force microscope (AFM) and scanning electron microscope (SEM). Fig. 5.23 shows the SEM images of the series.

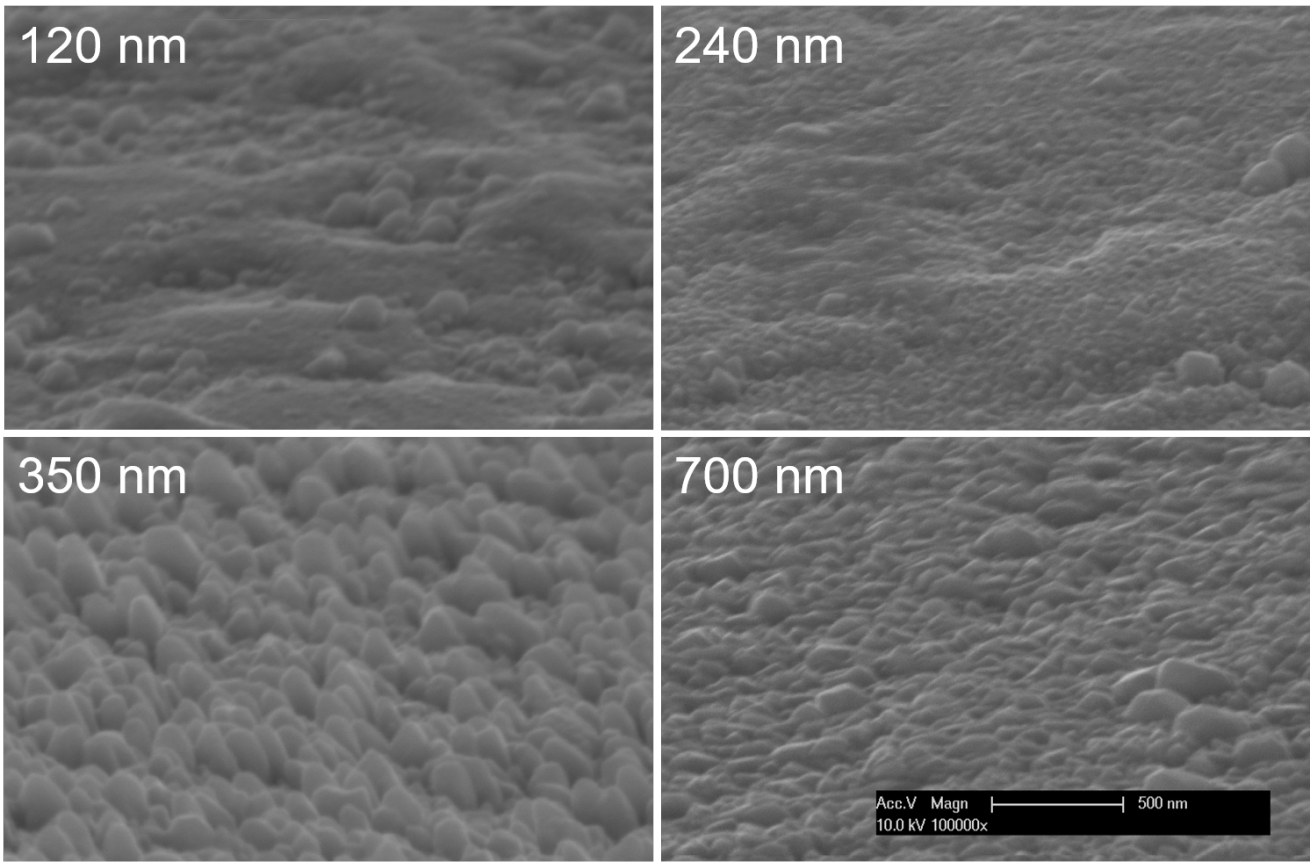

Figure 5.23.: SEM images of Nb_3Sn thin films synthesized by co-sputtering on copper substrates. The coating duration was increased from 10 min to 60 min resulting in 120 mm to 700 mm film thickness.

These images show that all samples, independent from the film thickness, were coated with an excellent

surface coverage. In addition, there are no macroscopic defects like cracks or voids visible. The average crystallite size (determined by the Williamson-Hall method) is about $39(12)$ nm for the sample of 120 nm. The sample of thickness 240 nm has an averaged grain size of $60(16)$ nm. Both samples have inter-granular areas that can be differentiated by the height. The thicker samples (350 nm and 700 nm) do not have such height differences. Therefore, it is a possible influence from the substrate. In both thicker samples, the height difference is dominated by large grains. The sample of 325 nm has a significantly higher grain size of $75(29)$ nm. The 700 nm sample has the overall smoothest surface and a grains size of $68(6)$ nm.

AFM is used to record a topographical image of the surface. These images are shown in Fig. 5.24 for the samples of thickness 120 nm and 700 nm.

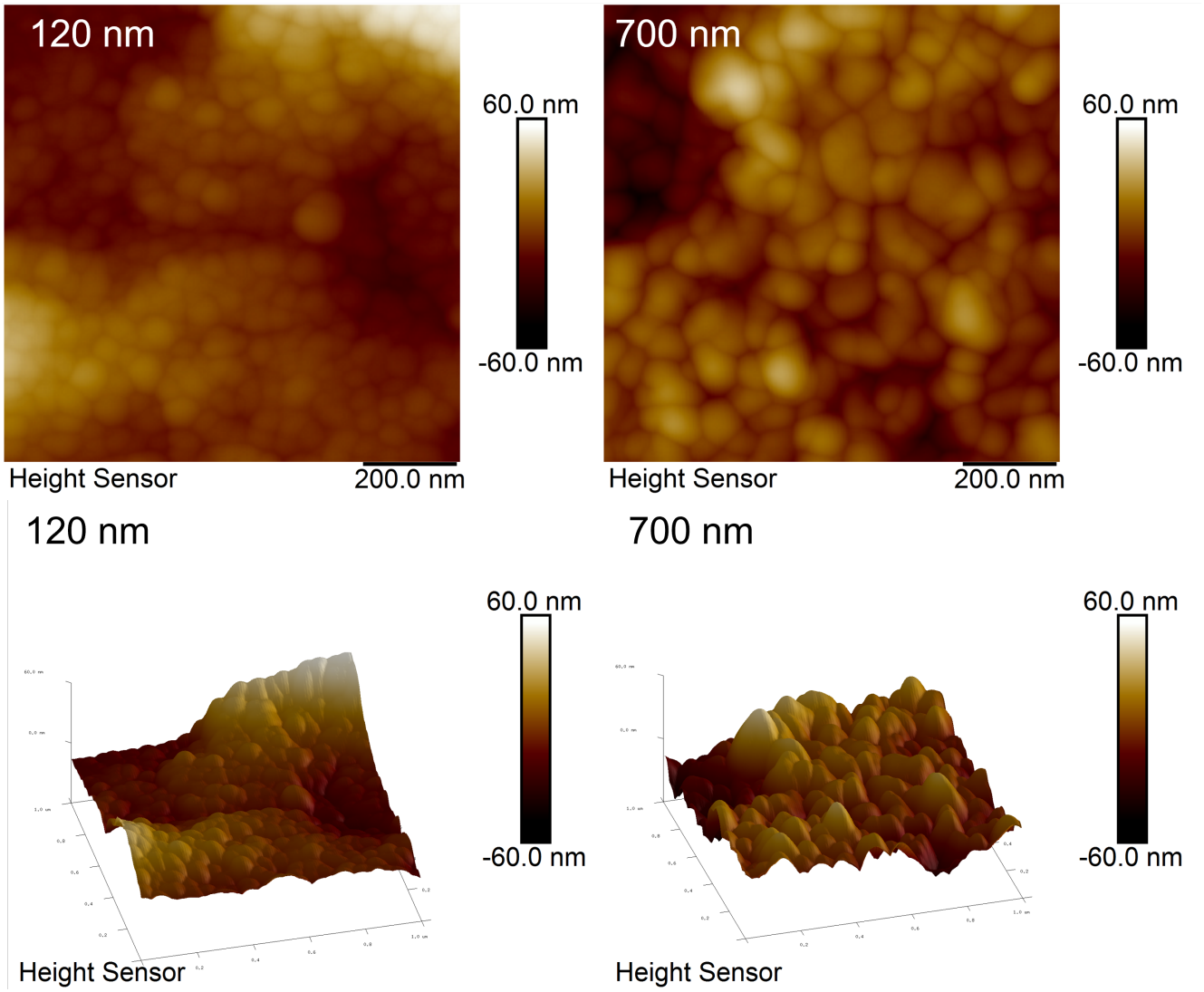

Figure 5.24.: AFM topography images of Nb_3Sn thin films synthesized by co-sputtering on copper substrates. The coating duration was 10 min and 60 min resulting in 120 nm and 700 nm film thickness, respectively.

The AFM topography images confirm the observation that the surface has inter-granular areas of high difference in height in case of the 120 nm sample and larger grains that define the surface roughness of the 700 nm sample. The absolute difference is determined to be 120 nm and the R_q (root mean square)

is 12.6 nm for the sample of thickness 120 nm while the sample of thickness 700 nm has a lower absolute height difference in the examined region and an R_q of 12.3 nm.

In thin film growth dynamics, there are usually some grains of preferential orientation that grow faster than the average. Unfavorable grain orientations grow slower and disappear in favor of other orientations. Such an effect can be observed from the SEM and AFM images of this series. The fact that the copper substrate has a high surface roughness can explain the roughness of the thinner films as an impact from the copper substrate. It can be clearly seen that the film growth comes with a surface smoothening effect. In comparison to other processes [31, 22, 20], co-sputtering produces much smaller grains. However, the obtained surface roughness is significantly lower [20, 129]. Pudasaini *et al.* [31] have shown that grains sizes can reach values of 7 µm after 100 h of heat treatment. Large grain sizes are believed to promote good SRF performance, though long heat treatments at high temperatures can also lead to segregation at the grain boundary [116]. However, the grain boundaries have only impact on the SRF performance when the grain boundary width is above the coherence length of 3 nm to 4 nm. This means that a small grain size is not harmful in the case of excellent grain boundary condition.

5.5.4. Adhesion of Nb_3Sn on copper substrate

The fact that the Nb_3Sn phase is brittle is the reason why the winding process of superconducting Nb_3Sn magnets is usually done before the heat treatment. Only after winding, the heat treatment forms the brittle Nb_3Sn phase [130]. Taking this as an example, the copper cavity is formed by mechanical processes and the coating takes place after the forming into the complex geometry of the cavity. The huge temperature difference between formation and operation however, induces stress in the thin film coating and can result in cracks and delamination. Stress is induced by the difference in thermal expansion coefficient between Nb_3Sn and copper. This stress can be reduced by a lower synthesis temperature to maintain long-term performance of the thin film coated cavity. Such cracks or delamination could not be observed (see Fig. 5.23). To get clear evidence for good thin film adhesion, spherical nanointendation is used. It is done by recording the load of the indenter as a function of the displacement into the material providing a load-displacement curve. A failure of the brittle Nb_3Sn film would be indicated as a pop-in (displacement step). The pop-in load for a sample of thickness 1000 nm in 'as-deposited' and after 15 cycles from 5 K to 300 K is shown in Fig. 5.25.

Figure 5.25.: Pop-in load measured by a nanoindentation testing of Nb_3Sn thin film with 1000 nm film thickness on copper substrate as-deposited and after 15 temperature cycles between 300 K and 5 K.

The sample demonstrated a pop-in load of 3.5 mN as-deposited. After 15 cycles the pop-in load remains unchanged at a value of 3.5 mN. A high degree of scatter is observed for this study. A high difference of the film thickness can be an explanation for this behavior. The failure of the thin film induced by nanoindentation testing is a crack perpendicular to the film surface. Another mechanical testing mode is a scratch test (spherical nanoindenter) that introduces shear forces in the thin film.

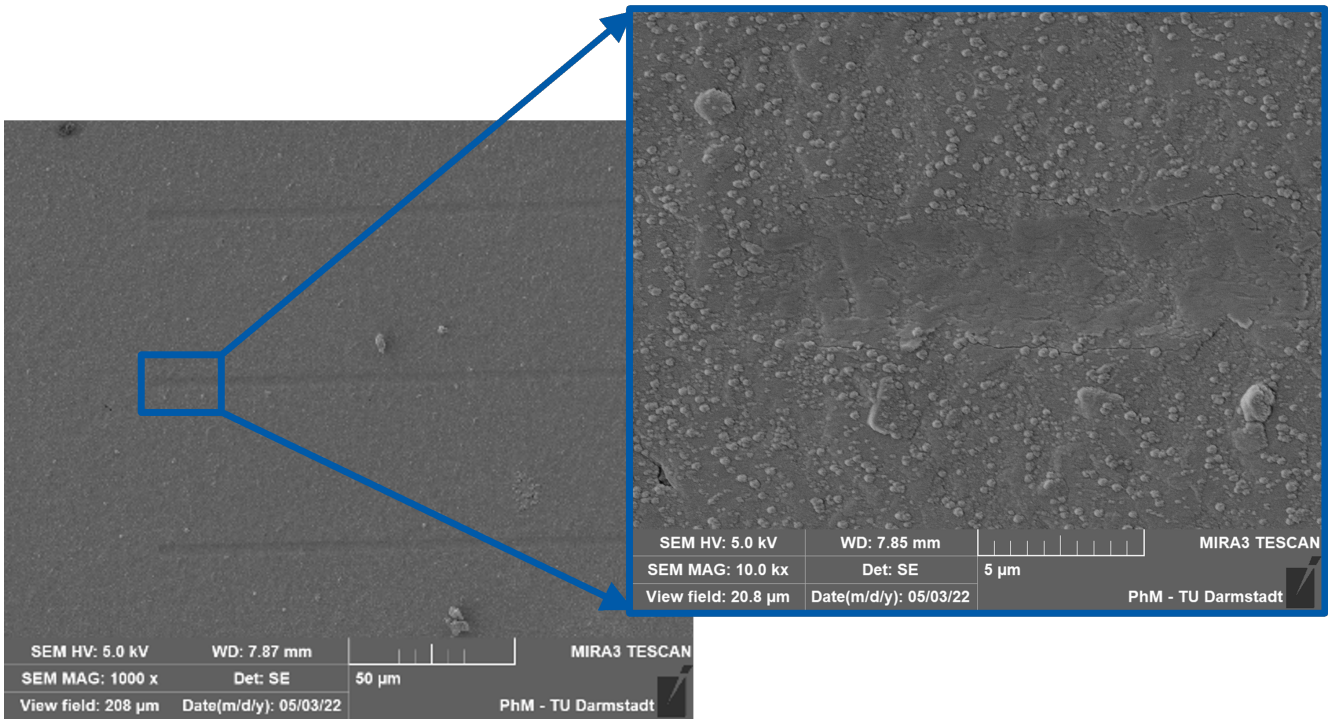

Figure 5.26.: SEM investigation of nanoindentation scratch tests on Nb_3Sn thin films synthesized by co-sputtering on copper substrates. The force is ramped to $10\,\mathrm{mN}$ (higher force on left side). In the enlarged blue box fracture is observed at the edges of the scratch path.

Fig. 5.26 shows the scratch test for a sample of thickness $1000\,\mathrm{nm}$ after 15 cycles from $5\,\mathrm{K}$ to $300\,\mathrm{K}$. The load is ramped up to $10\,\mathrm{mN}$ exceeding the previously determined pop-in load. It is clear from the images that the thin film cracked at the edges of the indenter track. Although the mechanical limit of the thin film was exceeded, the film was not delaminated from the substrate. In conclusion, these experiments are clear evidence that the Nb_3Sn exhibits good adhesion on copper. Even the temperature difference of almost $800\,\mathrm{K}$ between the coating and potential operation temperature together with the 15 temperature cycles of about $300\,\mathrm{K}$ difference did not result in delamination.

5.5.5. T_c and H_{c1} as a function of film thickness

It has been demonstrated that Nb_3Sn coatings on copper cavities can be realized in terms of non detrimental inter-diffusion, phase growth, as-deposited surface roughness and adhesion. There is no doubt that the most important criteria is the superconducting performance of the grown Nb_3Sn thin film on copper. For this reason, magnetization versus temperature and magnetization versus field measurements were conducted to investigate how the film thickness and the surface/interface roughness play a role in the performance. The slight presence of copper in the film deposited at $520\,^\circ\mathrm{C}$ is the reason why the temperature of the series in this section was lowered to $480\,^\circ\mathrm{C}$ to further decrease copper inter-diffusion. T_c is defined as the point where the $M-T$ curve starts to bend that corresponds to the value where the resistivity reaches zero. H_{c1} is determined as the point of lowest magnetization in the field free recorded $M-H$ curve (zero field cooled). Fig. 5.27 (top) shows the curves of both, zero field cooled (ZFC) and field cooled (FC) $M-T$ measurements in parallel orientation while Fig. 5.27 (bottom) shows the perpendicular orientation. ZFC measurements are plotted as solid lines while FC measurements are plotted as dashed lines.

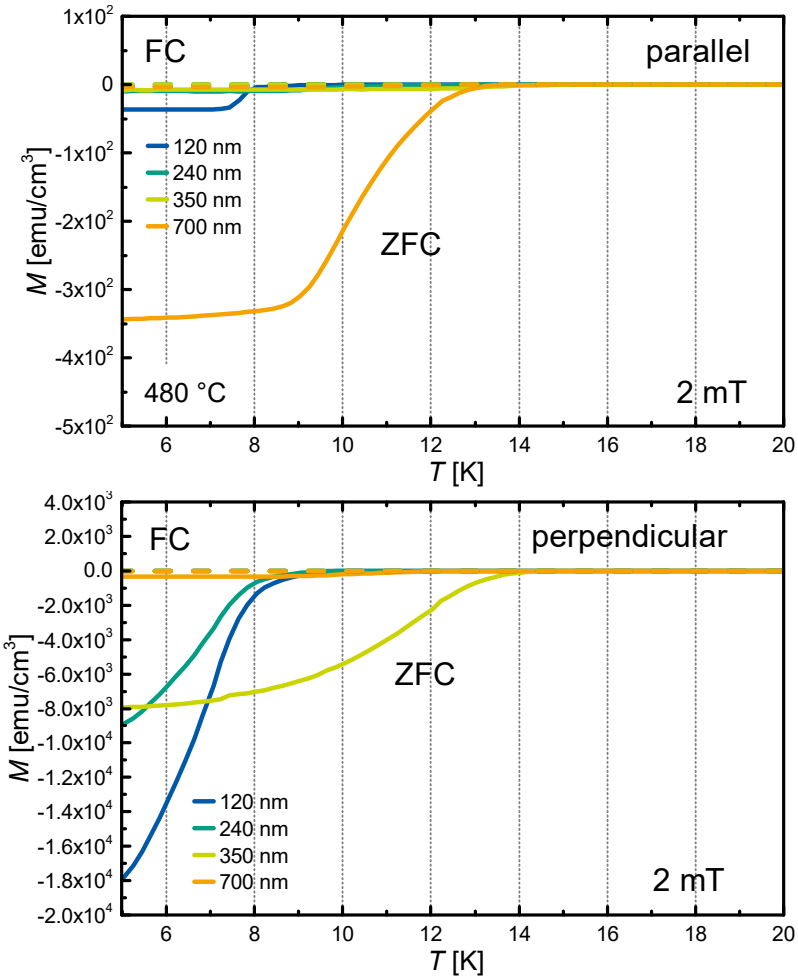

Figure 5.27.: Magnetization versus temperature measured by a MPMS as a function of the temperature in parallel orientation (top) and perpendicular orientation (bottom) of the magnetic field to the thin film surface for zero field cooled samples. Field cooled measurements are plotted for comparison by dashed lines. The film thickness was increased from $120\,\mathrm{nm}$ to $700\,\mathrm{nm}$. The critical temperature was defined as the temperature where the magnetization deviates from the linear fit of the paramagnetic magnetization in the normal conducting state. Magnetization at $20\,\mathrm{K}$ was subtracted from the measurement points.

The drop in magnetization demonstrates shielding of the external field by all samples in parallel and perpendicular orientation to the external field. This means that the whole sample is superconducting at the point where the magnetization becomes negative and shielding currents can flow in two dimensions, in-plane and out-of-plane. It can be seen that the magnetization is much stronger in the perpendicular orientation in comparison with the parallel orientation. The ZFC magnetization at $5\,\mathrm{K}$ of the perpendicular orientation shows increasing values for decreasing film thickness. The reason is that the magnetic moment is divided by the films volume to calculate the magnetization. The relatively low magnetization of the $700\,\mathrm{nm}$ film gives two indications. First, the shielding is not yet saturated for this film thicknesses. Otherwise, the magnetization would be weaker for the thicker films. Second, the decrease in magnetization is not proportional to the film thickness that means that a comparable volume of the films did not take part in the shielding response. The passive volume can be a surface oxide layer of constant thickness. This in

turn can mean that determined film thickness must be subtracted due to surface/interface roughness to an effective film thickness. In contrast to that, the 700 nm sample has the lowest magnetization followed by the sample of thickness 120 nm. The magnetization of the sample thicknesses 240 nm and 350 nm are even some orders of magnitudes lower. This order can only be explained by tilt and position of the samples within the SQUID in the MPMS. A slight relative rotation in parallel orientation has already a strong effect on the magnetization.

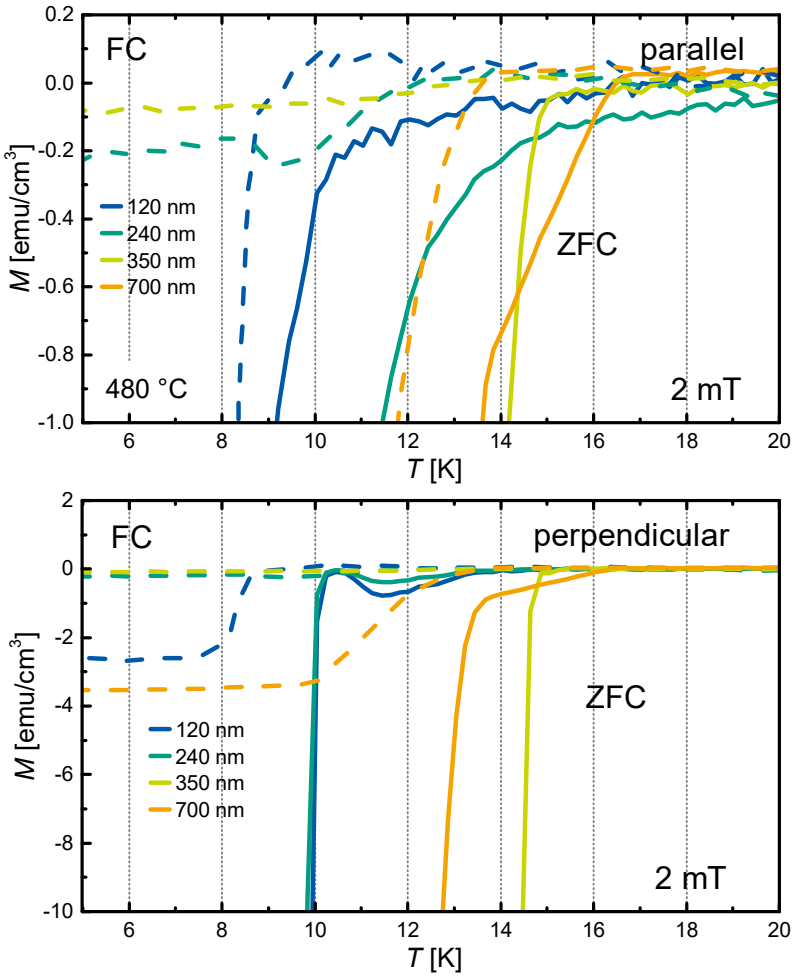

Figure 5.28.: Enlarged magnetization versus temperature measured by a MPMS as a function of the temperature in parallel orientation of the magnetic field to the thin film surface for zero field cooled samples. The film thickness was increased from 120 nm to 700 nm. The critical temperature was defined as the temperature where the magnetization deviates from the linear fit of the paramagnetic magnetization in the normal conducting state. Magnetization at 20 K was subtracted from the measurement points.

Fig. 5.28 shows a detailed view of the magnetization versus temperature measurements, in order to have a closer look at the magnetization at the phase transition. In both orientations, the critical temperature of the ZFC measurements ranges from 13.0 K to 16.8 K for the samples thicknesses 120 nm and 700 nm, respectively. In perpendicular orientation, the samples of thickness 120 nm and 240 nm show a small bump after the critical temperature. The bump can be explained by the paramagnetic Meissner effect (PME). The PME was described in FC measurements by Li [131], that is not in agreement with the observation made

for this series. Another explanation is given by Geim *et al.* [132] and Engelmann [133]. They propose a compression of frozen fluxes in a 'superconducting sheath' into a smaller volume that allows more flux to penetrate the sample. Since it occurs for the ZFC measurements, the origin of the 'frozen flux' is not clear. Possible origins are fluxes that penetrate the material over the edges of the sample or due to surface imperfections. The critical temperature for the FC measurements deviates from the critical temperatures in the ZFC measurements. Due to the (possible) different influence from flux pinning on the determined T_c from FC measurements, the values are not further discussed. The maximal critical temperature of $16.8\,\mathrm{K}$ on copper is higher than that of other work [109, 134].

It was proposed in section 5.1 that the flux jumps of the magnetization versus field measurements of Nb_3Sn on the fused silica substrate could be solved by shunting (via well heat conducting substrate). To confirm the proposed solution, $M - H$ measurements were carried out for the previous sample series. Fig. 5.29 shows the $M - H$ in the range $-3\,\mathrm{T}$ to $3\,\mathrm{T}$ for parallel (left) and perpendicular (right) orientation. It can be seen that the samples coated on copper substrate do no exhibit flux jumps. However, it can be seen for both orientations that the peak magnetization in the hysteresis is not a function of the film thickness. Crystals in two conditions can lead to comparable critical current densities and by that to comparable magnetization. One condition is a high quality crystal, the other is a relatively poor crystal quality together with pinning sites. Söll has shown how irradiation of Nb_3Sn can introduce defects acting as pinning sites and increase the critical current density [135]. For this series, it can be clearly seen that the samples order by magnetization in $M - H$ measurements is the same as in ZFC $M - T$ measurements. For this reason, it can be stated that the crystal quality dominates the magnetization, since pinning sites do not play a role in ZFC $M - T$ measurements.

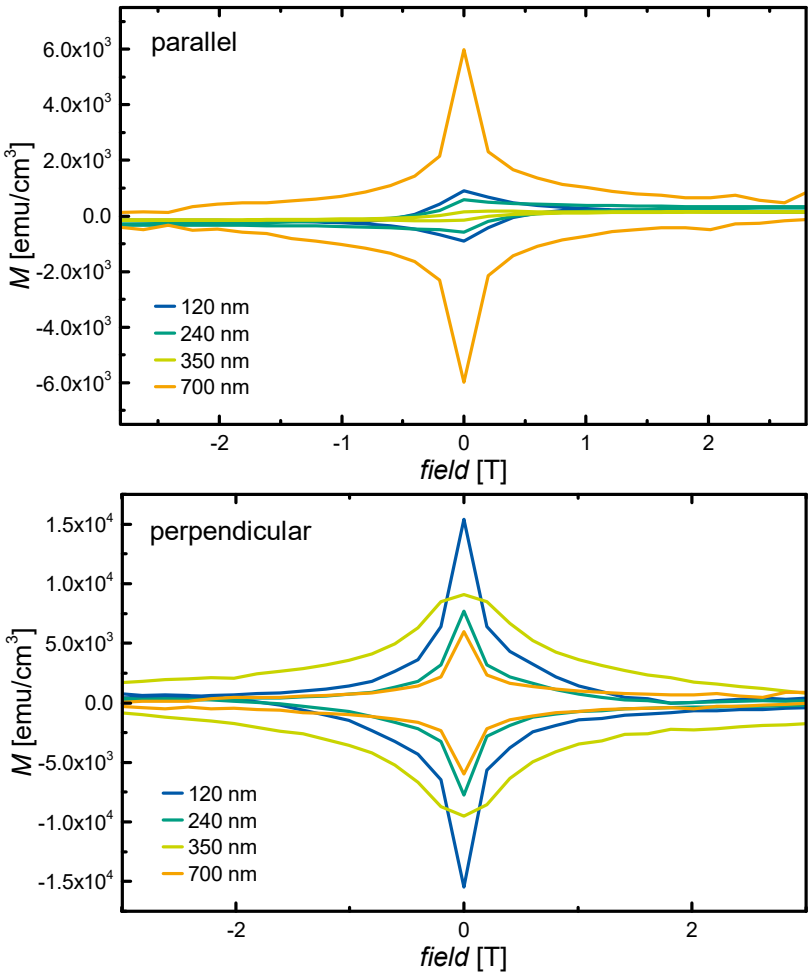

Figure 5.29.: Magnetization versus external field measured by a MPMS as a function of the temperature in parallel orientation (top) and perpendicular orientation (bottom) of the magnetic field to the thin film surface for zero field cooled samples. Field cooled measurements are plotted for comparison by dashed lines. The film thickness was increased from $120\,\mathrm{nm}$ to $700\,\mathrm{nm}$. The critical temperature was defined as the temperature where the magnetization deviates from the linear fit of the paramagnetic magnetization in the normal conducting state. Magnetization at $20\,\mathrm{K}$ was subtracted from the measurement points.

H_{c1} is another important factor for SRF applications, since it is influencing H_{SH}. It does not affect the surface resistivity, defines however the maximal acceleration gradient of the cavity. Equation 5.1 shows the temperature dependence of H_{c1} given with

$$H_{c1} = H_{c1}(0)[1 - (T/T_c^2)]. \tag{5.1}$$

From this relation, it is clear that the critical temperature influences the decrease of H_{c1} with increasing operation temperature. The reported literature values of bulk Nb_3Sn (T_{c}=18.3 K, H_{c1}=50 mT) have been set in Eq. 5.1 and the area below the plot is marked red in Fig. 5.30. The critical field H_{c1} was determined for a series of gradually increasing thickness by the lowest point of the virgin curve at a given temperature

and set in Eq. 5.1 to get the respective values for $H_{c1}(0)$ and T_c.

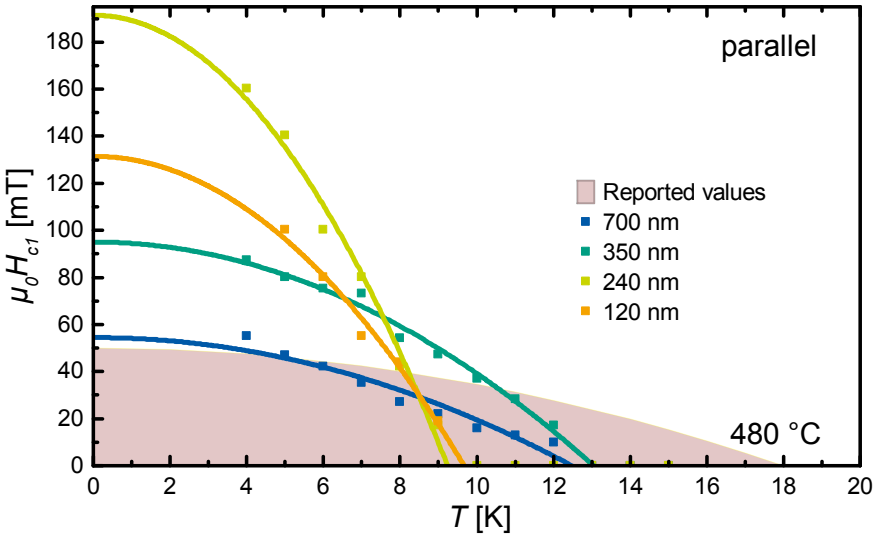

Figure 5.30.: Critical field H_{c1} determined from the lowest magnetization in magnetization versus external field measurements (virgin curves). H_{c1} was plotted as a function of the temperature. The coating duration was increased from $10\,\text{min}$ to $60\,\text{min}$ resulting in $120\,\text{nm}$ to $700\,\text{nm}$ film thickness. Curves were fitted to Equation 5.1. The reported bulk values of $50\,\text{mT}$ and $18.3\,\text{K}$ were used for comparison (red area).

It can be seen from Fig. 5.30 that the samples exhibit a T_c in the range of $9\,\text{K}$ to $13\,\text{K}$ that is much lower than the determined values from $M-T$ measurements. The explanation might be that the thin films do not have enough diamagnetic energy to fully shield the external field in the vicinity of the critical temperature. This behavior is also observed in $M-T$ measurements where the slope of magnetization is low. All determined $H_{c1}(0)$ are clearly higher than the bulk value. This was already described by Gurevich [56].

The critical temperature determined from ZFC $M-T$ measurements (for better comparability with literature) and the H_{c1} at $4\,\text{K}$ is plotted in Fig. 5.31 as function of the film thickness. The film thickness shows a clear impact on $H_{c1}(0)$. The film of thickness $700\,\text{nm}$ is found to have 'bulk-like' behavior. The values for H_{c1} range from $55\,\text{mT}$ to $190\,\text{mT}$. It can be seen that H_{c1} benefits from thinner film thicknesses, finding the optimum for a thickness of $240\,\text{nm}$.

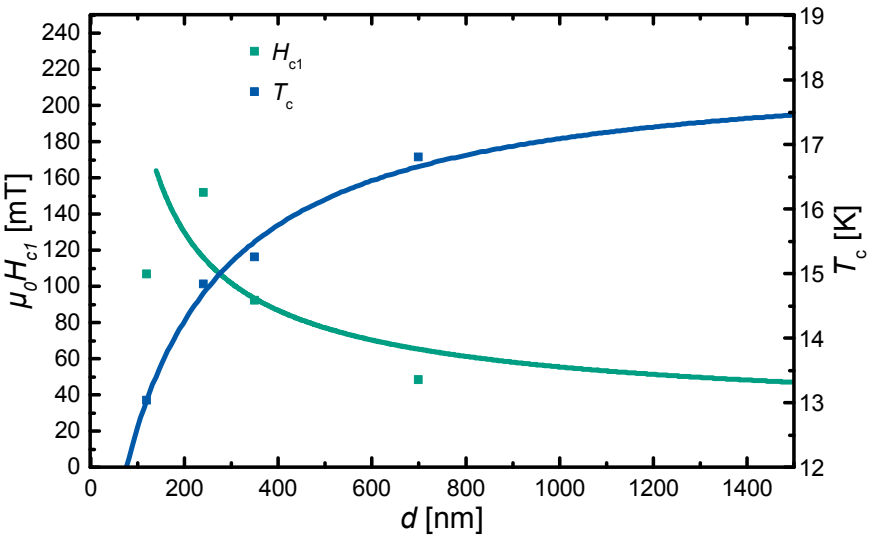

Figure 5.31.: Critical temperature T_c determined from $M-T$ measurements and critical field H_{c1} from $M-H$ measurements at $4\,\mathrm{K}$ of thin film Nb_3Sn on copper substrate as a function of thin film thickness. Solid lines provide a guide to the eye.

Since the enhancement of H_{c1} could be observed for thickness higher than the penetration depth of about $140\,\mathrm{nm}$, it must be noted that the determined film thickness must be corrected due to surface and interface roughness to an effective film thickness d_{eff}. From this relation it follows that the critical field enhancement occurs for films thinner than $310\,\mathrm{nm}$ (with a penetration depth of $140\,\mathrm{nm}$). In general, the thickness dependence of H_{c1} can be explained by a phase transition of second order at the transition from normal to superconducting state of thin films [136, 137]. Kubo *et al.* give counterflow currents at the interface as the reason for the field enhancement when $d \approx \lambda$ [138]. Two requirements must be fulfilled for a phase transition of second order that is an external magnetic field in parallel orientation to the film surface and a film thickness $d_{max} = \sqrt{5}\lambda$. A reduction of T_c for thin film thicknesses was experimentally shown for Nb thin films in contact to normal conducting metals by Il'in [139]. Cooper *et al.* found an explanation for the effect with a phonon exchange between the normal conducting metal and the superconducting metal [140]. As a consequence, the normal metal becomes superconducting and the superconductor becomes a normal conductor. Fominov *et al.* stated that the proximity effect depends on the interface resistance [141]. According to this work, the suppression of T_c is a consequence of a low interface resistance. The proximity effect, however, cannot be considered as an explanation in the present case. The samples presented in this section have thicknesses that are higher than the influence range of the interface. It is rather likely that the thin film growth needs several hundreds of nanometer for an optimal crystal growth.

6. Conclusion

6.1. Summary

The process optimization in the beginning of this work has demonstrated that high quality Nb_3Sn thin films can be synthesized by magnetron co-sputtering. Optimizing the deposition parameters can reproducibly create thin films with superconducting properties close to the bulk values. The temperature needed to create films with good performance is only $435\,°C$. This is possible due to relatively high kinetic energies in the range of several tens eV (in comparison to several hundreds of meV thermal energy) of the out-sputtered atoms at the sample surface. Another sample series with increasing sputtering power, and by that higher kinetic energy, was carried out at $320\,°C$, demonstrating that kinetic energy can only promote the phase growth by some extent and not fully replace the thermal energy. Using high kinetic energies at substrate temperatures below $435\,°C$ leads to drastically decreasing critical temperatures. The relatively low synthesis temperature and short synthesis duration together with excellent superconducting performance is of great technological importance, since it allows the coating of cavity with materials with a lower melting point than niobium. Nb_3Sn coated copper cavities can be a great step towards highly energy efficient SRF cavities. The reason is the high heat conductivity of copper, which can further improve the cryogenic efficiency in comparison to the Nb_3Sn coated niobium cavity.

Multi-step transitions from normal to superconducting state are observed. One solution to this behavior is found by providing more (kinetic) energy to the system. The capability of heat treatments after depositions is investigated in order to solve the origin of the multi-step transition and eventually improve the superconducting properties any further. The conducted experiments have shown that annealing above $500\,°C$ promotes grain growth. At the same time however, it has a negative impact on the transition width ΔT from normal conducting state to superconducting state.

In order to find the origin of the multi-step behavior, two different samples, with a sharp and broad transition each, have been investigated. The sample with the broad transition was found to be much worse in terms of homogeneity on micro and atomic scale, but also demonstrated a strong impact of the external field on the critical current through the grain boundaries. It is believed that severe elemental inhomogeneity on micro-scale creates some grain boundaries in unfavorable condition. This in turn is a possible origin for the multi-step transition. The sample with the sharp transition has demonstrated homogeneous grain boundary conditions, an excellent tin distribution, as well as a low atomic disorder. It could be demonstrated that external fields have a low impact on the superconducting properties in the examined magnetic field range which is a fundamental requirement for the RF application.

The established co-sputtering process was utilized to coat copper substrates with which it could prove its versatility to any substrate material with a low melting point. A qualitative proof of a low copper inter-diffusion at about $500\,°C$ is given, which is however, not detrimental for the superconducting properties. Nb_3Sn is likely to decompose into other Nb-Sn intermetallics at the applied synthesis temperatures in case of long deposition duration. For this reason, high sputtering rates together with short deposition duration need to be chosen to avoid a decomposition of the pristine Nb_3Sn phase. The perfectly low surface roughness as well as the good substrate coverage achieved on copper substrates are promising for high acceleration gradients. The adhesion of the Nb_3Sn thin film on copper substrate even after several

temperature cycles is an evidence for an excellent long-term stability of the next generation Nb_3Sn thin film coated copper cavity. It could be shown that the performance of Nb_3Sn co-sputtered films on copper have bulk-like performance. The film thickness has a strong impact on the critical temperature and critical field which even exhibits a strong critical field enhancement for thicknesses below a certain threshold. This means that operators of particle accelerators can choose between high acceleration fields or high cryogenic efficiency for their particle accelerator.

6.2. Outlook

The critical temperature of a superconductor is only a benchmark for crystal quality, not a benchmark for SRF performance. In this work, the highest reported critical temperature of bulk could not be achieved. It has to be investigated, if it can be further improved by an increase of the process temperature, sputtering power or higher film thickness. To evaluate the copper diffusion quantitatively and figure out the definite limit of process temperature, another characterisation method (e.g. secondary ion mass specroscopy) with higher sensitivity has to be applied. With this method copper diffusion can be quantified with a better sensitivity than XPS (with ion beam etching). Another method is EXAFS, where measurements at the copper absorption edge could show the next neighbors of the copper atoms in the substrate. Angle resolved EXAFS measurements could give two answers. The first is the amount of copper atoms diffusing in the superconducting film. The other is the tin diffusion into the substrate. Tin in the substrate is, per se, not harmful. It can however, cause tin-poor atomic layers at the interface. These could hinder counterflow-currents at the interface and decrease SRF performance.

Nb_3Sn has a great potential to save enormous amounts of energy in comparison to bulk Nb. In times of climate change and particularly in times of exorbitant energy prices due to uncertain supply chains (e.g. helium), it becomes more important to exploit this potential to maintain the operation of huge facilities at optimal efficiency. After this work, it remains unclear how good the SRF performance of the present Nb_3Sn thin films is. The experiments done in this work show a promising performance in direct current superconductivity. The performance can only indicate a good SRF performance, which must however, be measured directly to show the potential of Nb_3Sn in future work. SRF performance of cavity is quantified in terms of the Q-factor which can be expressed as function of acceleration gradient or operation temperature. The Q-factor is related to the geometry of a cavity and its resonant frequency. To compare different materials and different cavity geometries the surface resistivity must be measured. There are two options to determine the surface resistivity. One is the Q-slope of a cavity, the other measurement set-ups which can measure the surface resistivity. The quadrupole resonator (QPR) at HZB is one of these measurement set-ups [142]. It is a versatile method to determine the superconductors SRF performance of samples with $75\,\mathrm{mm}$ diameter. Subsequently to this thesis, samples for the QPR should be prepared and measured to investigate the influence of weak links and flux pinning on the surface resistivity of Nb_3Sn. The influence of the film thickness is another parameter which must be investigated. Following Gurevich's description, the critical field enhancements by film thicknesses below the penetration depth could tremendously increase the acceleration gradients. It is however, not clear if this is also valid for SRF applications, why different film thicknesses should be tested in the QPR. The film thickness was discussed as a trade-off between critical temperature and critical field. In case that RF measurements show no critical field enhancement beyond the bulk value, it is a clear indication to use thick Nb_3Sn films which have higher critical temperatures.

The coated QPR samples are only a way to measure field dependent and temperature dependent surface resistivity as a measure of SRF performance and are no replacement for the cavity. For this reason, the challenging transformation of the co-sputtering process to coat cavities is inevitable. In order to realize this, many approaches are under current development [16, 143, 144]. These approaches clearly rely on only one target at a time. The co-sputtering process relies on two targets which make the coating of a

cavity even more challenging. The achieved performance in this work is only useful, if the co-sputtering can be used to coat a cavity.

A. appendix

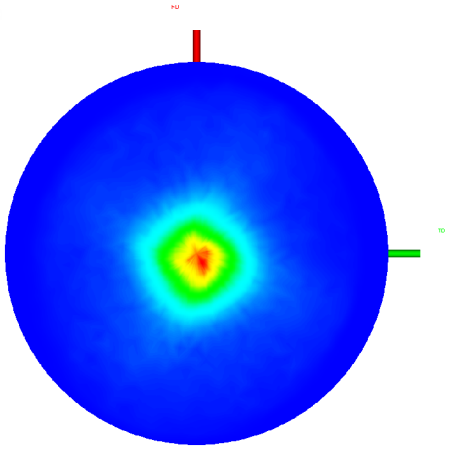

Figure A.1.: Pole figure of 200 diffraction peak of Nb_3Sn sputtered on fused silica at $435\,°C$ utilizing $30\,W$ Sn/$158\,W$ Nb.

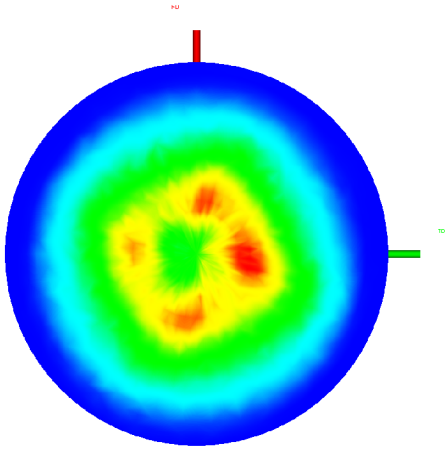

Figure A.2.: Pole figure of 210 diffraction peak of Nb_3Sn sputtered on fused silica at $435\,°C$ utilizing $30\,W$ Sn/$158\,W$ Nb.

Fig. A.1 and A.2 display pole figures measured by XRD to investigate the texture of Nb_3Sn sputtered on fused silica at $435\,°C$ utilizing $30\,W$ Sn/$158\,W$ Nb. The pole figure of the 200 diffraction peak shows highest intensities for smallest out-of-plane angles. The pole figure (Fig. A.2) of the 210 diffraction peak has high intensity in a circular shape around the center. This demonstrates a strong texture in the (100) orientation (perpendicular to surface plane).

In table A.1 tin content, FHWM of the 210 diffraction peak, critical temperature and RRR values are listed for Nb_3Sn sputtered at different temperatures. Tin concentration is close to the desired value of $25\,\%$. FHWM of the 210 diffraction peak increases for decreasing temperatures demonstrating smaller crystallites at lower substrate temperatures. Critical temperature decreases for decreasing substrate temperatures during deposition. RRR values are in the range of 1 to 1.5.

Table A.1.: Sample overview of Nb_3Sn grown on fused silica by co-sputtering. The substrate temperature was decreased from $435\,°C$ to $260\,°C$ at a constant power ratio of 5.25 and $20\,W$ Sn/$105\,W$ Nb. The tin content, $FWHM$ of the 210 bragg peaks, critical temperature and RRR values are listed.

T_{sub} [°C]	Sn [At-%]	$FWHM$ [°]	$T_{c,90}$ [K]	RRR
435	25.3±0.3	0.367	13.9	1.02
410	25.3±0.3	0.387	15.1	1.22
360	24.1±1.2	0.381	14.7	1.41
320	23.0±0.7	0.414	11.5	1.04
280	24.5±0.8	0.493	7.3	1.49
260	22.8±0.8	0.497	/	/

Table A.2 shows properties for Nb_3Sn sputtered at $435\,°C$ on fused silica utilizing increasing total sputtering power of $15\,W$ Sn/$79\,W$ Nb to $30\,W$ Sn/$158\,W$ Nb at a constant power ratio of 5.25. Tin concentration, $FWHM$ of the 210 diffraction peak, critical temperature, RRR value and total film thickness d is listed.

Table A.2.: Sample overview of Nb_3Sn grown on fused silica by co-sputtering. The sputtering power was increased from $15\,W$ Sn/$79\,W$ Nb to $30\,W$ Sn/$158\,W$ Nb at a constant power ratio of 5.25 and $435\,°C$ substrate temperature. Tin content, $FWHM$ of the 210 Bragg peak, critical temperature, RRR values and film thickness d are listed.

P_{Sn}/P_{Nb} [W/W]	Sn [At-%]	$FWHM$ [°]	$T_{c,90}$ [K]	RRR	d [nm]
15/79	17.7±0.7	0.367	13.8	1.14	1127±188
20/105	25.3±0.3	0.387	15.1	1.83	884±79
25/131	24.1±0.3	0.368	14.8	1.14	909±230
30/158	25.7±0.2	0.337	16.3	1.49	1637±199

The used $I(V)$ characteristics of the sputtering process are listed in table A.3 in dependence of the utilized total sputtering powers of $15\,W$ Sn/$79\,W$ Nb to $30\,W$ Sn/$158\,W$ Nb at a constant power ratio of 5.25. Sputtering is performed using a RF power source for Sn and a DC power source for Nb.

Table A.3.: Sample overview of Nb_3Sn grown on fused silica by co-sputtering. The sputtering power was increased from $15\,$W Sn/$79\,$W Nb to $30\,$W Sn/$158\,$W Nb at a constant power ratio of 5.25 and $435\,°$C substrate temperature. $I(V)$ characteristics are listed.

P_{Sn}/P_{Nb} [W/W]	I_{Nb} [A]	V_{Nb} [V]	I_{Sn} [A]	V_{Sn} [V]
15/79	0.305	257	0.169	89
20/105	0.393	267	0.190	105
25/131	0.489	275	0.212	118
30/158	0.562	281	0.227	132

The average and median of the kinetic energy distribution during the sputtering process for the utilized sputtering powers of of $15\,$W Sn/$79\,$W Nb to $30\,$W Sn/$158\,$W Nb are listed in table A.4.

Table A.4.: Sample overview of Nb_3Sn grown on fused silica by co-sputtering. The sputtering power was increased from $15\,$W Sn/$79\,$W Nb to $30\,$W Sn/$158\,$W Nb at a constant power ratio of 5.25 and $435\,°$C substrate temperature. Average and median of kinetic energy distributions are listed.

P_{Sn}/P_{Nb} [W/W]	$\overline{E}_{kin,Sn}$ [eV]	$\overline{E}_{kin,Nb}$ [eV]	$\tilde{E}_{kin,Sn}$ [eV]	$\tilde{E}_{kin,Nb}$ [eV]
15/79	2.21	5.77	0.63	2.02
20/105	2.32	5.82	0.71	2.02
25/131	2.43	5.87	0.80	2.02
30/158	2.49	5.90	0.89	2.02

List of Figures

List of Tables

Bibliography

[1] *New element named after its German birthplace*. URL: https://cordis.europa.eu/article/id/20730-new-element-named-after-its-german-birthplace (visited on 04/11/2022).

[2] *Heike Kamerlingh Onnes: Facts*. URL: https://www.nobelprize.org/prizes/physics/1913/onnes/biographical/ (visited on 02/01/2021).

[3] W. Meissner and R. Ochsenfeld. "Ein neuer Effekt bei eintritt der Supraleitfähigkeit". In: *Naturwissenschaften* 21 (1933), pp. 787–788.

[4] J. Bardeen, L. N. Cooper, and J. R. Schrieffer. "Theory of Superconductivity". In: *Phys. Rev.* 108 (5 Dec. 1957), pp. 1175–1204.

[5] J. G. Bednorz and K. A. Müller. "Possible high Tc superconductivity in the Ba-La-Cu-O system". In: *Zeitschrift für Physik B Condensed Matter* 64.2 (1986), pp. 189–193.

[6] *Superconductivity*. URL: https://en.wikipedia.org/wiki/Superconductivity (visited on 02/01/2021).

[7] R. G. Sharma. *Superconductivity : basics and applications to magnets*. Springer Cham, 2015.

[8] *Meet the 32 Tesla Superconducting Magnet*. URL: https://nationalmaglab.org/about-the-maglab/around-the-lab/meet-the-magnets/meet-the-32-tesla-superconducting-magnet/ (visited on 09/20/2023).

[9] P. Schmüser. "Superconductivity in high energy particle accelerators". In: *Progress in Particle and Nuclear Physics* 49.1 (2002), pp. 155–244.

[10] F. Hinterberger. *Physik der Teilchenbeschleuniger und Ionenoptik*. Springer-Verlag, 2013.

[11] B. W. Smith and K. Suzuki. *Microlithography: science and technology*. CRC press, 2018.

[12] C. Pagani et al. "LASA Superconducting RF Cavities for Particle Accelerators". In: *Toward a Science Campus in Milan*. Ed. by Pier Francesco Bortignon et al. Springer International Publishing, 2018, pp. 293–305.

[13] B. Aune et al. "Superconducting TESLA cavities". In: *Physical Review Special Topics - Accelerators and Beams* 3.9 (Sept. 2000). DOI: 10.1103/physrevstab.3.092001. URL: https://doi.org/10.1103%2Fphysrevstab.3.092001.

[14] *Weltmaschine: Teilcheinbeschleuniger*. URL: https://www.weltmaschine.de/cern_und_lhc/technologietransfer/teilchenbeschleuniger/ (visited on 03/18/2022).

[15] *Welt der Physik: Häufige Fragen zum LHC*. URL: https://www.weltderphysik.de/gebiet/teilchen/experimente/teilchenbeschleuniger/lhc/lhc-faq/ (visited on 03/18/2022).

[16] M. N. Sayeed et al. "Microstructural and Superconducting Radiofrequency Properties of Multilayer Sequentially Sputtered Nb3Sn films". In: *IEEE Transactions on Applied Superconductivity* 31.5 (2021), pp. 1–4.

[17] S. Foner and E. J. McNiff. “Upper critical fields of cubic and tetragonal single crystal and polycrystalline Nb3Sn in DC fields to 30 tesla”. In: *Solid State Communications* 39.9 (1981), pp. 959–964.

[18] M. K. Transtrum, G. Catelani, and J. P. Sethna. “Superheating field of superconductors within Ginzburg-Landau theory”. In: *Phys. Rev. B* 83 (9 Mar. 2011), p. 094505.

[19] B. Hillenbrand et al. “Superconducting Nb3Sn cavities with high microwave qualities”. In: *IEEE Transactions on Magnetics* 13.1 (1977), pp. 491–495.

[20] S. Posen et al. “Advances in Nb3Sn superconducting radiofrequency cavities towards first practical accelerator applications”. In: *Superconductor Science and Technology* 34.2 (Jan. 2021), p. 025007.

[21] A. Godeke. “Nb3Sn for Radio Frequency Cavities”. In: *The International Workshop on: Thin Films and new ideas for pushing the limits of RF superconductivity*. Legnaro National Labs. 2006.

[22] J. Lee et al. “Atomic-scale analyses of Nb3Sn on Nb prepared by vapor diffusion for superconducting radiofrequency cavity applications: a correlative study”. In: *Superconductor Science and Technology* 32.2 (2018), p. 024001.

[23] D. L. Hall et al. “High Quality Factor Studies in SRF Nb3Sn Cavities”. In: *SRF2015*. TRIUMF. 2015, TUPB044.

[24] A. Godeke. “A review of the properties of Nb3Sn and their variation with A15 composition, morphology and strain state”. In: *Superconductor Science and Technology* 19.8 (2006), R68–R80.

[25] E. A. Ilyina et al. “Development of sputtered Nb3Sn films on copper substrates for superconducting radiofrequency applications”. In: *Superconductor Science and Technology* 32.3 (2019), p. 035002.

[26] B. Hillenbrand and H. Martens. “Superconducting Nb3Sn cavities with high quality factors and high critical flux densities”. In: *Journal of Applied Physics* 47.9 (1976), pp. 4151–4155.

[27] B. Hillenbrand et al. “Superconducting Nb3Sn-cavities”. In: *IEEE Transactions on Magnetics* 11.2 (1975), pp. 420–422.

[28] S. Posen and M. Liepe. “Advances in development of Nb 3 Sn superconducting radio-frequency cavities”. In: *Physical Review Special Topics-Accelerators and Beams* 17.11 (2014), p. 112001.

[29] M. Peiniger and H. Piel. “A Superconducting Nb3Sn Coated Multicell Accelerating Cavity”. In: *IEEE Transactions on Nuclear Science* 32.5 (1985), pp. 3610–3612.

[30] M. Perpeet et al. “High-quality Nb3Sn thin films on sapphire prepared by tin vapor diffusion”. In: *Journal of applied physics* 82.10 (1997), pp. 5021–5023.

[31] U. Pudasaini et al. “Insights into formation of Nb3Sn film during the vapor diffusion process”. In: *SRF2017*. IMP and IHEP, pp. 539–542.

[32] A. A. Rossi et al. “Nb3Sn films by multilayer sputtering”. In: *SRF2009*. Helmholtz-Zentrum Berlin. 2009, TUOBAU06.

[33] M. N. Sayeed et al. “Magnetron sputtering of Nb3Sn for SRF cavities”. In: *IPAC2018*. TRIUMF. 2018, THPAL129.

[34] W. Tan et al. “Nb3Sn thin film deposition on copper by DC magnetron sputtering”. In: *SRF2017*. IMP and IHEP. 2017, TUPB055.

[35] G. Rosaz et al. “Development of Nb3Sn coatings by magnetron sputtering for SRF cavities”. In: *SRF2015*. TRIUMPF. 2015, TUPB051.

[36] S. Sosa-Guitron, A. Gurevich, and J. Delayen. “Measurements of RF properties of thin film Nb3Sn superconducting multilayers using a calorimetric technique”. In: *SRF2015*. TRIUMF. 2015, TUPB060.

[37] C. T. Wu, R. T. Kampwirth, and J. W. Hafstrom. “High-rate magnetron sputtering of high Tc Nb3Sn films”. In: 14.1 (1977), pp. 134–137.

[38] G. Carta et al. “Attempts to deposit Nb3Sn by MO-CVD”. In: *Proc. Int. Workshop on Thin Films and New Ideas for Pushing the Limits of RF Superconductivity (Padua)* (2006).

[39] E. Barzi et al. “Synthesis of superconducting Nb3Sn coatings on Nb substrates”. In: *Superconductor Science and Technology* 29.1 (2015), p. 015009.

[40] S. Franz et al. “Electrochemical synthesis of Nb3Sn coatings on Cu substrates”. In: *Materials Letters* 161 (2015), pp. 613–615.

[41] S. Posen and D. L. Hall. “Nb3Sn superconducting radiofrequency cavities: fabrication, results, properties, and prospects”. In: *Superconductor Science and Technology* 30.3 (2017).

[42] C.J. Gorter and H.G.B. Casimir. In: *Phys. Z.* 35 (1934), p. 963.

[43] B. D. Josephson. “Possible new effects in superconductive tunnelling”. In: *Physics letters* 1.7 (1962), pp. 251–253.

[44] P. W. Anderson and J. M. Rowell. “Probable observation of the Josephson superconducting tunneling effect”. In: *Physical Review Letters* 10.6 (1963), p. 230.

[45] A. B. Pippard. “The coherence concept in superconductivity”. In: *Physica* 19.1-12 (1953), pp. 765–774.

[46] A. A. Abrikosov. “On the magnetic properties of superconductors of the second group”. In: *Sov. Phys. JETP* 5 (1957), pp. 1174–1182.

[47] C. P. Bean. “Magnetization of Hard Superconductors”. In: *Phys. Rev. Lett.* 8 (6 Mar. 1962), pp. 250–253.

[48] C. P. Bean. “Magnetization of High-Field Superconductors”. In: *Rev. Mod. Phys.* 36 (1 Jan. 1964), pp. 31–39.

[49] V. L. Ginzburg and L. D. Landau. “K teorii sverkhrovodimosti”. In: *Zhurnal Eksperimentalnoi i Teoreticheskoi Fiziki* 20 (1950), pp. 1064–1082.

[50] H. Fröhlich. “Theory of the Superconducting State. I. The Ground State at the Absolute Zero of Temperature”. In: *Phys. Rev.* 79 (5 Sept. 1950), pp. 845–856.

[51] E. Maxwell. “Isotope Effect in the Superconductivity of Mercury”. In: *Phys. Rev.* 78 (4 May 1950), pp. 477–477.

[52] C. A. Reynolds et al. “Superconductivity of Isotopes of Mercury”. In: *Phys. Rev.* 78 (4 May 1950), pp. 487–487.

[53] J. Bardeen. “Wave Functions for Superconducting Electrons”. In: *Phys. Rev.* 80 (4 Nov. 1950), pp. 567–574.

[54] L. N. Cooper. “Bound Electron Pairs in a Degenerate Fermi Gas”. In: *Phys. Rev.* 104 (4 Nov. 1956), pp. 1189–1190.

[55] R. Meservey and D. H. Douglass. “Energy Gap Measurements by Tunneling between Superconducting Films. II. Magnetic Field Dependence”. In: *Phys. Rev.* 135 (1A July 1964), A24–A33.

[56] A. Gurevich. “Enhancement of rf breakdown field of superconductors by multilayer coating”. In: *Applied Physics Letters* 88.1 (2006), p. 012511.

[57] C. P. Bean and J. D. Livingston. “Surface Barrier in Type-II Superconductors”. In: *Phys. Rev. Lett.* 12 (1 Jan. 1964), pp. 14–16.

[58] P. V. Christiansen. “Magnetic superheating of high-κ superconductors”. In: *Solid State Communications* 7.10 (1969), pp. 727–729.

[59] H. Padamsee, J. Knobloch, and T. Hays. “RF Superconductivity for Accelerators John Wiley & Sons”. In: *Inc., New York* (1998), p. 199.

[60] J. Knobloch. “The “Q disease” in superconducting niobium RF cavities”. In: *AIP Conference Proceedings*. Vol. 671. 1. American Institute of Physics. 2003, pp. 133–150.

[61] A.-M. Valente-Feliciano. “Superconducting RF materials other than bulk niobium: a review”. In: *Superconductor Science and Technology* 29.11 (Sept. 2016), p. 113002.

[62] A. Gurevich. “Theory of RF superconductivity for resonant cavities”. In: *Superconductor Science and Technology* 30.3 (2017), p. 034004.

[63] W. Singer. “SRF cavity fabrication and materials”. In: *arXiv preprint arXiv:1501.07142* (2015).

[64] A. Grassellino et al. “Unprecedented quality factors at accelerating gradients up to 45 MVm-1 in niobium superconducting resonators via low temperature nitrogen infusion”. In: *Superconductor Science and Technology* 30.9 (2017), p. 094004.

[65] P. Dhakal et al. “Effect of low temperature baking in nitrogen on the performance of a niobium superconducting radio frequency cavity”. In: *Physical Review Accelerators and Beams* 21.3 (2018), p. 032001.

[66] R. D. Veit et al. “Suppression of nano-hydride growth on Nb (100) due to nitrogen doping”. In: *The Journal of Chemical Physics* 152.21 (2020), p. 214703.

[67] W. J. Schneider, P. Kneisel, and C. H. Rode. “Gradient optimization for SC CW accelerators”. In: *Proceedings of the 2003 Particle Accelerator Conference*. Vol. 5. IEEE. 2003, pp. 2863–2868.

[68] D. B. Liarte et al. “Theoretical estimates of maximum fields in superconducting resonant radio frequency cavities: stability theory, disorder, and laminates”. In: *Superconductor Science and Technology* 30.3 (2017), p. 033002.

[69] S. Keckert et al. “Critical fields of Nb3Sn prepared for superconducting cavities”. In: *Superconductor Science and Technology* 32.7 (2019), p. 075004.

[70] G. F. Hardy and J. K. Hulm. “Superconducting Silicides and Germanides”. In: *Phys. Rev.* 89 (4 Feb. 1953), pp. 884–884.

[71] B. T. Matthias et al. “Superconductivity of Nb_3Sn”. In: *Phys. Rev.* 95 (6 Sept. 1954), pp. 1435–1435.

[72] J. J. Hanak, K. Strater, and G. W. Cullen. “Preparation and properties of vapor-deposited niobium stannide”. In: *RCA (Radio Corporation of America) Review (U.S.)* 25 (Sept. 1964).

[73] R. E. Enstrom. “Superconducting Properties of Nb6Sn5 and of Multiphase Nb–Sn Alloys”. In: *Journal of Applied Physics* 37.13 (1966), pp. 4880–4882.

[74] J. P. Charlesworth. “The superconducting transition temperatures of Nb6Sn5 and NbSn2”. In: *Physics Letters* 21.5 (1966), pp. 501–502.

[75] D. J. Van Ooijen, J. H. N. Van Vucht, and W. F. Druyvesteyn. “Superconductivity of NbSn2”. In: *Phys. Letters* 3 (1962), pp. 128–129.

[76] H. Devantay et al. “The physical and structural properties of superconducting A15-type Nb-Sn alloys”. In: *Journal of Materials Science* 16.8 (1981), pp. 2145–2153.

[77] R. Flükiger. “Atomic Ordering, Phase Stability and Superconductivity in Bulk and Filamentary A15 Type compounds”. In: *IV. conference*. Kernforschungszentrum Karlsruhe. 1987.

[78] D. Dew-Hughes. “Superconducting A-15 compounds: A review”. In: *Cryogenics* 15.8 (1975), pp. 435–454.

[79] D. O. Welch et al. “Defects and diffusion mechanisms in Nb3Sn”. In: *Journal of Physics and Chemistry of Solids* 45.11 (1984), pp. 1225–1242.

[80] G. R. Stewart, L. R. Newkirk, and F. A. Valencia. “Impurity stabilized A15 Nb3Nb - a new superconductor”. In: *Physical Review B* 21.11 (1980), p. 5055.

[81] L. J. Vieland. “High-temperature phase equilibrium and superconductivity in the system niobiumtin”. In: *RCA (Radio Corporation of America) Review (US)* 25 (1964).

[82] W. Buckel and W. Weber. “Superconductivity in d-and f-Band Metals”. In: *IV. conference*. Kernforschungszentrum Karlsruhe. 1982.

[83] M. C. Jewell et al. “The Upper Critical Field of Stoichiometric and Off-Stoichiometric Bulk, Binary Nb3Sn”. In: *AIP Conference Proceedings* 711.1 (2004), pp. 474–484.

[84] Angus Rockett. “Thin film growth processes”. In: *The Materials Science of Semiconductors* (2008), pp. 455–503.

[85] S. Swann. “Magnetron sputtering”. In: *Physics in Technology* 19 (1988), p. 67.

[86] J. R McNeil, J. J. McNally, and P. D. Reader. “11 - Ion Beam Deposition”. In: *Handbook of Thin Film Deposition Processes and Techniques (Second Edition)*. Ed. by K. Seshan. Second Edition. Norwich, NY: William Andrew Publishing, 2001, pp. 463–499.

[87] W. H. Bragg and W. L. Bragg. “The reflection of X-rays by crystals”. In: *Proceedings of the Royal Society of London. Series A, Containing Papers of a Mathematical and Physical Character* 88.605 (1913), pp. 428–438.

[88] W. L. Bragg. “The structure of some crystals as indicated by their diffraction of X-rays”. In: *Proceedings of the Royal Society of London. Series A, Containing papers of a mathematical and physical character* 89.610 (1913), pp. 248–277.

[89] B. D. Cullity. *Elements of X-ray Diffraction*. Addison-Wesley Publishing, 1956.

[90] A. Snigirev et al. “On the possibilities of x-ray phase contrast microimaging by coherent high-energy synchrotron radiation”. In: *Review of Scientific Instruments* 66.12 (1995), pp. 5486–5492.

[91] *Materials Science: SEM Resolution*. URL: https://www.thermofisher.com/de/de/home/materials-science/learning-center/applications/sem-resolution.html (visited on 08/11/2022).

[92] B. J. Inkson. “2 - Scanning electron microscopy (SEM) and transmission electron microscopy (TEM) for materials characterization”. In: *Materials Characterization Using Nondestructive Evaluation (NDE) Methods*. Ed. by Gerhard Hübschen et al. Woodhead Publishing, 2016, pp. 17–43.

[93] T. R. Shojaei, S. Soltani, and M. Derakhshani. “Chapter 6 - Synthesis, properties, and biomedical applications of inorganic bionanomaterials”. In: *Fundamentals of Bionanomaterials*. Ed. by A. Barhoum, J. Jeevanandam, and M. K. Danquah. Micro and Nano Technologies. Elsevier, 2022, pp. 139–174.

[94] *Scanning electron microscope*. URL: https://www.nanoscience.com/techniques/scanning-electron-microscopy/ (visited on 08/11/2022).

[95] T. Bayer. “Einfluss injizierter Ladungen auf Ba0, 6Sr0, 4TiO3-Dünnschichten: Elektrische und dielektrische Charakterisierung und Simulation des Ladungstransport”. PhD thesis. Technische Universität, 2014.

[96] S. Tougaard. “Practical algorithm for background subtraction”. In: *Surface Science* 216.3 (1989), pp. 343–360.

[97] A. R. Nyaiesh and L. Holland. “The dependence of deposition rate on power input for dc and rf magnetron sputtering”. In: *Vacuum* 31.7 (1981), pp. 315–317.

[98] M. N. Sayeed et al. “Structural and superconducting properties of Nb3Sn films grown by multilayer sequential magnetron sputtering”. In: *Journal of Alloys and Compounds* 800 (2019), pp. 272–278.

[99] M. N. Sayeed et al. “Properties of Nb3Sn films fabricated by magnetron sputtering from a single target”. In: *Applied Surface Science* 541 (2021), p. 148528.

[100] R. Ghosh, D. Basak, and S. Fujihara. “Effect of substrate-induced strain on the structural, electrical, and optical properties of polycrystalline ZnO thin films”. In: *Journal of Applied Physics* 96.5 (2004), pp. 2689–2692.

[101] R. Grewe et al. “Superconducting RF cavity materials research at the S-DALINAC”. In: *SRF2019*. Helmholtz Zentrum Dresden. 2019, MOP022.

[102] L. Alff et al. “Ramp-edge Josephson junctions with Nd1.85Ce0.15CuO4-y barriers.” In: *Physica C* (271 1996), pp. 339–348.

[103] B. Mayer et al. “Superconducting transport properties of Bi2Sr2CaCu2O8+x bicrystal grain boundary junctions”. In: *Applied Physics Letters* 63.7 (1993), pp. 996–998.

[104] C. Z. Antoine. “Influence of crystalline structure on RF dissipation in Niobium: flux trapping, hydride precipitate, doping behavior...” In: *arXiv preprint arXiv:1802.07241* (2018).

[105] P. Cuadra-Solís. “Vortex Dynamics in Superconducting Thin Films under Microwave Fields”. PhD thesis. Universitat de Barcelona, 2015.

[106] J.-Y. Lee et al. “Saw-tooth pattern from flux jumps observed by high resolution M-H curves in MgB2 thin films”. In: *Journal of Applied Physics* 108.3 (2010), p. 033909.

[107] V. Kashikhin. “Flux jumps on Nb3Sn magnets”. In: *Technical Division Notes Library*. Fermi National Accelerator Laboratory. 2003.

[108] *SiMTra - Simulation of the Metal Transport*. URL: `http://draftugentbe.webhosting.be/index.php?p=137` (visited on 07/30/2020).

[109] Y. Trenikhina et al. “Performance-defining properties of Nb3Sn coating in SRF cavities”. In: *Superconductor Science and Technology* 31.1 (2017), p. 015004.

[110] *Thermal Conductivity: Al2O3*. URL: `https://www.makeitfrom.com/material-properties/Alumina-Aluminum-Oxide-Al2O3` (visited on 11/14/2022).

[111] G. K. Williamson and W. H. Hall. “X-ray line broadening from filed aluminium and wolfram”. In: *Acta Metallurgica* 1.1 (1953), pp. 22–31.

[112] P. M. Kibasomba et al. “Strain and grain size of TiO2 nanoparticles from TEM, Raman spectroscopy and XRD: The revisiting of the Williamson-Hall plot method”. In: *Results in Physics* 9 (2018), pp. 628–635.

[113] K. Howard, Z. Sun, and M. U. Liepe. “Thermal annealing of sputtered Nb3Sn and V3Si thin films for superconducting RF cavities”. In: *SRF2021*. FRIB. 2021, TUPB051.

[114] V. N. Kolosov and A. A. Shevyrev. “Effect of Heat Treatment on the Structure and Properties of Superconducting Nb and Nb3Sn Electrodeposits”. In: *Inorganic Materials* 40 (2004), pp. 235–240.

[115] G. Wang, M. J. Raine, and D. P. Hampshire. “The cause of ‘weak-link’ grain boundary behaviour in polycrystalline Bi2Sr2CaCu2O8 and Bi2Sr2Ca2Cu3O10 superconductors”. In: *Superconductor Science and Technology* 31.2 (2018), p. 024001.

[116] J. Lee et al. “Grain-boundary structure and segregation in Nb3Sn coatings on Nb for high-performance superconducting radiofrequency cavity applications”. In: *Acta Materialia* 188 (2020), pp. 155–165.

[117] W. C. Stewart. “Current-voltage characteristics of josephson junctions”. In: *Applied Physics Letters* 12.8 (1968), pp. 277–280.

[118] R. Gross et al. “Thermally activated phase slippage in high-T_c grain-boundary Josephson junctions”. In: *Phys. Rev. Lett.* 64 (2 1990), pp. 228–231.

[119] J. H. Durrell et al. “The behavior of grain boundaries in the Fe-based superconductors”. In: *Reports on Progress in Physics* 74.12 (2011), p. 124511.

[120] A. M. Campbell and J. E. Evetts. “Flux vortices and transport currents in type II superconductors”. In: *Advances in Physics* 21.90 (1972), pp. 199–428.

[121] J. J. Rehr et al. “Parameter-free calculations of X-ray spectra with FEFF9”. In: *Physical Chemistry Chemical Physics* 12.21 (2010), pp. 5503–5513.

[122] Mm Newville. “Larch: an analysis package for XAFS and related spectroscopies”. In: *Journal of Physics: Conference Series*. Vol. 430. 1. IOP Publishing. 2013, p. 012007.

[123] Z. Balogh and G. Schmitz. “5 - Diffusion in Metals and Alloys”. In: *Physical Metallurgy (Fifth Edition)*. Ed. by D. E. Laughlin and K. Hono. Fifth Edition. Oxford: Elsevier, 2014, pp. 387–559.

[124] C. Toffolon, C. Servant, and B. Sundman. “Thermodynamic assessment of the Nb-Sn system”. In: *Journal of phase equilibria* 19.5 (1998), pp. 479–485.

[125] C. Toffolon et al. “Reassessment of the Nb-Sn system”. In: *Journal of phase equilibria* 23.2 (2002), pp. 134–139.

[126] R. A. Schiffman and D. M. Bailey. “Thermodynamics of the incongruently subliming niobium-tin system”. In: *High Temp. Sci.;(United States)* 15.2/3 (1982).

[127] H. S. Padamsee. “Superconductivity in high energy particle accelerators”. In: *Annu. Rev. Nucl. Part. Sci* 64.1 (2014), pp. 175–196.

[128] M. K. Transtrum, G. Catelani, and J. P. Sethna. “Superheating field of superconductors within Ginzburg-Landau theory”. In: *Physical Review B* 83.9 (2011), p. 094505.

[129] Z. Sun et al. “Surface roughness reduction of Nb3Sn thin films via laser annealing for superconducting radio-frequency cavities”. In: *IPAC2021*. LNLS/CNPEM. 2021.

[130] H. Müller and T. Schneider. “Heat treatment of Nb3Sn conductors”. In: *Cryogenics* 48.7-8 (2008), pp. 323–330.

[131] M. S. Li. “Paramagnetic Meissner effect and related dynamical phenomena”. In: *Physics reports* 376.3 (2003), pp. 133–223.

[132] A. K. Geim et al. “Paramagnetic Meissner effect in small superconductors”. In: *Nature* 396.6707 (1998), pp. 144–146.

[133] J. Engelmann. “Spannungsinduzierte Supraleitung in undotierten BaFe2As2-Dünnschichten”. PhD thesis. Technische Universität Dresden, 2014.

[134] L. Xiao et al. “The technical study of Nb 3 Sn film deposition on copper by HiPIMS”. In: *SRF2019*. HZDR. 2019, pp. 846–847.

[135] M. Söll. “Changing of the critical current density of Nb3Sn”. In: *Journal of Nuclear Materials* 72.1-2 (1978), pp. 122–128.

[136] H.J. Fink, D.S. McLachlan, and B. Rothberg-Bibby. “Chapter 6 First and Second Order Phase Transitions of Moderately Small Superconductors in a Magnetic Field”. In: ed. by D. F. Brewer. Vol. 7. Progress in Low Temperature Physics. Elsevier, 1978, pp. 435–516.

[137] M. Tinkham. *Introduction to superconductivity*. Courier Corporation, 2004.

[138] T. Kubo, Y. Iwashita, and T. Saeki. “Radio-frequency electromagnetic field and vortex penetration in multilayered superconductors”. In: *Applied Physics Letters* 104.3 (2014), p. 032603.

[139] K. S. Il’in et al. “Technology and Performance of THz Hot-Electron Bolometer Mixers”. In: *IEEE Transactions on Applied Superconductivity* 19.3 (2009), pp. 269–273.

[140] L. N. Cooper. “Superconductivity in the neighborhood of metallic contacts”. In: *Physical Review Letters* 6.12 (1961), p. 689.

[141] Ya. V. Fominov and M. V. Feigel’man. “Superconductive properties of thin dirty superconductor–normal-metal bilayers”. In: *Phys. Rev. B* 63 (9 Feb. 2001), p. 094518.

[142] S. Keckert et al. “Characterizing materials for superconducting radiofrequency applications—A comprehensive overview of the quadrupole resonator design and measurement capabilities”. In: *Review of Scientific Instruments* 92.6 (2021), p. 064710.

[143] A. Sublet et al. “Thin Film Coating Optimization For HIE-ISOLDE SRF Cavities: Coating Parameters Study and Film Characterization”. In: *SRF2013*. CERN. 2013.

[144] J. Dai et al. “The development of niobium sputtering on copper cavities at IHEP”. In: *SRF2019*. HZDR. 2019, pp. 613–615.

[145] N. Schäfer et al. “Kinetically induced low-temperature synthesis of Nb3Sn thin films”. In: *Journal of Applied Physics* 128.13 (2020), p. 133902.

[146] N. Schäfer et al. “Role of kinetic energy on Nb_3Sn thin films by low-temperature co-sputtering”. In: *Journal of Applied Physics* 134.4 (July 2023), p. 043903.

[147] N. Schäfer et al. “Physical Properties of Nb_3Sn Layers on Cu by Buffer-free Co-Sputtering for Sustainable High-Performance SRF Cavities”.

[148] N. Schäfer, M. Major, and L. Alff. “A review of Nb_3Sn thin film processing for Nb SRF cavities”. In: *Verhandlungen der Deutschen Physikalischen Gesellschaft*. Deutsche Physikalische Gesellschaft. 2019.

[149] N. Schäfer, M. Major, and L. Alff. “Nb_3Sn multitarget sputtering for Nb SRF cavities”. In: *SRF2019*. Helmholtz Zentrum Dresden. 2019.

[150] N. Schäfer et al. “Nb_3Sn thin film synthesis for SRF application by co-sputtering”. In: *Verhandlungen der Deutschen Physikalischen Gesellschaft*. Deutsche Physikalische Gesellschaft. 2021.

[151] N. Schäfer et al. “Nb_3Sn thin film synthesis for SRF application by co-sputtering”. In: *IPAC2021*. LNLS/CNPEM. 2021.

[152] N. Schäfer et al. “Nb_3Sn thin film synthesis for SRF application by co-sputtering”. In: *Verhandlungen der Deutschen Physikalischen Gesellschaft*. Deutsche Physikalische Gesellschaft. 2022.

[153] N. Schäfer et al. “Nb_3Sn Co-Sputtering for Interlayer-Free High Performance Copper Based SRF Cavities”. In: *IPAC2022*. Thai Synchrotron National Lab. 2022.

[154] N. Schäfer et al. "Nb_3Sn Co-Sputtering for Interlayer-Free High Performance Copper SRF Cavities". In: *Verhandlungen der Deutschen Physikalischen Gesellschaft*. Deutsche Physikalische Gesellschaft. 2023.

[155] N. Schäfer et al. "Nb_3Sn Co-Sputtering for Interlayer-Free High Performance Copper Based SRF Cavity". In: *SRF2023*. Facility for Rare Isotope Beams at Michigan State University. 2019.

Danksagung

Vielen dank an...

Herrn **Prof. Dr. Lambert Alff** und Herrn **Dr. Márton Major** für die Möglichkeit der Promotion an diesem tollen Thema und all die Freiheiten und Möglichkeiten für meine persönliche Entwicklung.

Herrn **Prof. Dr. Dirk Lützenkirchen-Hecht** für das Angebot des Zweitgutachtens und die interessanten Kooperationen.

Herrn **Prof. Dr. Leopoldo Molina-Luna** und **Prof. Dr. Herbert De Gersem** für die Übernahme der Prüfungsverantwortung.

Herrn **Prof. Dr. Heiko Wende**, Frau **Dr. Katharina Ollefs** und Herrn **Damian Günzing** für EXAFS Messungen und insbesondere die umfangreichen Auswertung.

Herrn **Dr. Christian Dietz** für AFM Aufnahmen.

Herrn **Dr. Sebastian Bruns** für Schichthaftungstests.

Herrn **Prof. Dr. Leopoldo Molina-Luna** und Herrn **Tianshu Jiang** für TEM Aufnahmen.

Herrn **Dr. Alexey Arzumanov** und **Dr. Philipp Komissinskiy** für die gemeinsame Projektarbeit, die erstaunliche Ergebnisse vorweisen kann.

Herrn **Dr. Stefan Petzold** für die sprachliche Patenschaft zweier Publikationen.

die anderen **ATFT Doktoranden** für unterhaltsame Gründe die Arbeit gelegentlich etwas liegen zu lassen.

Herrn **Jürgen Schreeck** und Herrn **Michael Weber**, sowie **die gesamte Mechanikwerkstatt** für die technische Anleitung, Reparaturen und großartigen ”Basteleien”.

meinen Vater für die finanzielle Untersützung während des Studiums und bin glücklich, dass er jetzt nicht mehr warten muss bis ich endlich ”richtig” Geld verdiene.

B. List of publications

N. Schäfer et al. “Kinetically induced low-temperature synthesis of Nb3Sn thin films”. In: *Journal of Applied Physics* 128.13 (2020), p. 133902

N. Schäfer et al. “Role of kinetic energy on Nb_3Sn thin films by low-temperature co-sputtering”. In: *Journal of Applied Physics* 134.4 (July 2023), p. 043903

N. Schäfer et al. “Physical Properties of Nb_3Sn Layers on Cu by Buffer-free Co-Sputtering for Sustainable High-Performance SRF Cavities”

C. List of conference contributions

N. Schäfer, M. Major, and L. Alff. "A review of Nb_3Sn thin film processing for Nb SRF cavities". In: *Verhandlungen der Deutschen Physikalischen Gesellschaft*. Deutsche Physikalische Gesellschaft. 2019

N. Schäfer, M. Major, and L. Alff. "Nb_3Sn multitarget sputtering for Nb SRF cavities". In: *SRF2019*. Helmholtz Zentrum Dresden. 2019

N. Schäfer et al. "Nb_3Sn thin film synthesis for SRF application by co-sputtering". In: *Verhandlungen der Deutschen Physikalischen Gesellschaft*. Deutsche Physikalische Gesellschaft. 2021

N. Schäfer et al. "Nb_3Sn thin film synthesis for SRF application by co-sputtering". In: *IPAC2021*. LNLS/CNPEM. 2021

N. Schäfer et al. "Nb_3Sn thin film synthesis for SRF application by co-sputtering". In: *Verhandlungen der Deutschen Physikalischen Gesellschaft*. Deutsche Physikalische Gesellschaft. 2022

N. Schäfer et al. "Nb_3Sn Co-Sputtering for Interlayer-Free High Performance Copper Based SRF Cavities". In: *IPAC2022*. Thai Synchrotron National Lab. 2022

N. Schäfer et al. "Nb_3Sn Co-Sputtering for Interlayer-Free High Performance Copper SRF Cavities". In: *Verhandlungen der Deutschen Physikalischen Gesellschaft*. Deutsche Physikalische Gesellschaft. 2023

N. Schäfer et al. "Nb_3Sn Co-Sputtering for Interlayer-Free High Performance Copper Based SRF Cavity". In: *SRF2023*. Facility for Rare Isotope Beams at Michigan State University. 2019